UNIVERSITY OF OKLAHOMA

GRADUATE COLLEGE

Evolution of the Structure and Dynamics of the Nocturnal Low-Level Jet after the Passage of a Cold Front and Insights into the Initiation and Maintenance of Nocturnal Convection

A THESIS

SUBMITTED TO THE GRADUATE FACULTY

in partial fulfillment of the requirements for the

Degree of

MASTER OF SCIENCE IN METEOROLOGY

By

Christopher Rattray
Norman, Oklahoma
2021

Evolution of the Structure and Dynamics of the Nocturnal Low-Level Jet after the Passage of a Cold Front and Insights into the Initiation and Maintenance of Nocturnal Convection

A THESIS APPROVED FOR THE
SCHOOL OF METEOROLOGY

BY THE COMMITTEE CONSISTING OF

Dr. David B. Parsons, Chair

Dr. Alan Shapiro, Co-Chair

Dr. Elinor Martin

Acknowledgments

This work would not be possible without everyone who has supported me over the years working on this project. I would first like to thank my committee members: Drs. Parsons, Shapiro and Martin. It has been a privilege working with them, and this work is a direct result of their guidance and patience. I would also like to thank my family for their support. This work would have been much more difficult without moral support from my father, mother, brother and late dog Coco.

Table of Contents

List of Figures

Abstract

Nocturnal low-level jets (NLLJs) are commonly observed over the Southern Great Plains (SGP) and have been linked to occurrence of the nocturnal maximum in mesoscale convective systems over this region during the late spring and summer. Researchers have long proposed that the Blackadar mechanism of an inertial ageostrophic oscillation superimposed on a southerly geostrophic flow is a likely cause of the southerly NLLJ. The NLLJ has also been the subject of recent research, in part driven by the community focus on Plains Elevated Convection at Night (PECAN) field campaign. Findings from this recent research include that the NLLJ is not just composed of a southerly jet, but also includes a maximum in the westerly winds above the southerly jet. The potential importance of baroclinicity on the sloping terrain in contributing to the NLLJ structure has also been a recent focus with a contribution to the NLLJ structure likely to be as or even more important than the Holton mechanism which assumes constant buoyancy along the slope. While temperature and moisture advection associated with the NLLJ has been shown known to create favorable conditions for deep convection, recent investigations have proposed a variety of other mechanisms. These mechanisms include persistent ascent driven by an inertial-gravity associated with a local maximum in the lateral variations in buoyancy, quasi-geostrophic ascent associated with warm advection, and the destabilization and maintenance of deep convection by bores and long-period gravity waves.

This thesis investigates the evolution of the structure of the NLLJ following two cold frontal passages over the SGP region during the International H2O Project field campaign (IHOP_2002). The NLLJs where examined in subsequent days after cold frontal passages on 25 May and 5 June 2002. The data set utilized includes radiosonde observations made at 3-h intervals from five sites maintained by the ARM (Atmospheric Radiation Measurement). These data sets provided insight into processes contributing to the NLLJ structure and to the return of the favorable conditions over the SGP for deep convection including the spatial and temporal variations in Convective Available Potential Energy. The

analysis of data from IHOP_2002 was supplemented with the fields from the ERA-5 Reanalysis. The 30-km horizontal grid and 1-h temporal resolution of this data set allowed deeper insight into the temporal and spatial variations of conditions over the sloping terrain.

The findings from this analysis include that the southerly and westerly component of the NLLJ strengthened in both intensity and height following the two cold frontal passages. The intensity of the southerly NLLJ was linked to the ageostrophic enhancement expected from Blackadar mechanism superimposed on a far larger general increase in the background southerly geostrophic wind. The increase in the southerly geostrophic flow extended over a depth of 3 to 4 km apparently in association with heating over the sloped terrain on synoptic time-scales. In order to better understand the evolution of NLLJ in these post-frontal periods, the evolution of conditions following the frontal passage on 5 June was investigated in detail. Specifically, the period was divided into a pre-moistening, moistening and post-moistening phases. A key finding was that the buoyancy gradient on and over the slope became increasingly non-uniform during this recovery period. During the post-moistening period, the buoyancy gradient at the surface became clearly non-linear with an increased gradient evident over a distance of $\sim 2^{\circ}$ of longitude in response to diurnal heating. Calculations showed that the enhancement to the pressure gradient force that occurred after peak heating exhibited spatial variability on scales of < 150 km, but was smoothed out at scales of > 300 km. The leading edge of this enhanced gradient was associated with a transition in the day-time boundary layer depth changing from ~ 4 km (above ground level) to the west compared to only ~ 1 km over the moist air mass. The circulations at this transition in boundary layer height had the characteristics of a dryline, which formed in the late afternoon and moved up the slope after sunset. Thus, during this post-moistening phase the recently proposed concept of a uniformly linear buoyancy gradient on the slope is no longer valid in the vicinity of this enhanced and moving gradient in buoyancy associated with the dryline. In this region, the vertical profile in the southerly geostrophic wind also does not remain constant with height during the night.

Our results suggest that over the western slopes, the NLLJ can be inherently heterogeneous due to the non-uniform and evolving gradients in buoyancy over the slope and that advection by the southerly winds above the NLLJ also impact the variations in NLLJ structure. These results stand in contrast to recent studies that have shown that the NLLJ becomes heterogeneous primarily due to advection by the westerly component of the NLLJ over the sloping terrain in the presence of a linear variation in buoyancy on the slope. Our finding of an inherently non-linear structure during the post-moistening phase also made it difficult to determine the extent to an inertial oscillation was contributing to NLLJs during this period. The impacts of this changing buoyancy gradient was associated with the NLLJs strengthening with intensification of a baroclinic zone as the height of the southerly v_{max} was consistent with being produced from a thermal wind reversal along sloped terrain. Other key findings from our analysis are that the long wave radiative impacts likely impact the thermal gradients and that the diurnal reversals in the buoyancy gradient on the slope varied in magnitude, timing and height. For example, early in the post-frontal period the buoyancy reversal took place near the surface in association with the nocturnal stable layer, while the late in the period, the reversal took place aloft in associated with the growth of the morning boundary layer.

Our analysis also has implications for understanding the mechanisms for the initiation and maintenance of deep convection in the NLLJ environment. Specifically, NLLJs were critical in returning conditions favorable for convection, with moisture transport playing a greater role on earlier after the frontal passage and ascent later in the recovery process after the frontal passage. The nature of the nocturnal boundary layer also varied significantly during the recovery period following the frontal passage changing initially from shallow ($<$ 100 m) and strong inversions initially to deeper ($\sim$500 to 800 m) and less stable inversions capped by an inversion. Another relevant finding is that late in the recovery period, the conditions on the higher slopes to the west become less favorable for deep convection during the night as the layer of high CAPE becomes more shallow. This finding that

convection will become less likely to occur over higher terrain later in the night is consistent with the concept of a west-to-east progression of nocturnal convection over the Great Plains. Our analysis also provided insight into the vertical motions in the NLLJ environment that could influence the initiation and maintenance of deep convection. Specifically, the analysis appeared consistent with the presence of inertial-gravity wave generated in the deep, warm residual layers to the west. Ascent was also associated with warm advection as has been argued to occur from quasi-geostrophic forcing. Our analysis shows, however, that the warm advection by the ageostrophic motions is similar in magnitude to the geostrophic forcing and occurs over a deeper depth. Thus, a semi-geostrophic framework is likely to be relevant than quasi-geostrophic theory. Other mechanisms for ascent are also discussed.

Chapter 1

Introduction

1.1 Motivation

This thesis seeks to advance our knowledge of the mechanisms that control the structure of the nocturnal low-level jet (NLLJ) and how the NLLJ structure contributes to the existence of a nocturnal maximum in deep convection over the United States Great Plains region (USGP). More than a century has passed since Kincer (1916) found precipitation to exhibit a nocturnal maximum over the USGP, yet there is still a lack of consensus on the primary mechanism(s) responsible for this peak (e.g., Geerts et al. 2017). This nocturnal maximum in precipitation appears to be linked to circulations impacted by the unique topography of the Southern Great Plains (SGP) and surrounding regions as the environment containing nocturnal convection often includes a NLLJ (e.g., Means 1952; Curtis and Panofsky 1958; Pitchford and London 1962; Maddox et al. 1979; Maddox 1983; Trier and Parsons 1993). Within the United States, this southerly wind maximum is known to occur most frequently over western Oklahoma and Kansas during the warm season (Bonner 1968; Mitchell et al. 1995; Whiteman et al. 1997; Arritt et al. 1997; Song et al. 2005; Walters et al. 2008).

The need to increase our knowledge of the understanding of nocturnal convection and CI events in the NLLJ environment, particularly those without surface boundaries is motivated in part by the finding that these CI events result in organized MCSs (e.g, Reif and Bluestein 2017). Such organized systems can have significant societal impacts that range from providing an important source of rainfall for agriculture (Fritsch et al. 1986), cause flooding (Doswell III et al. 1996) and are associated with severe weather (Gallus Jr et al. 2008). Unfortunately, numerical weather model prediction often shows a relative lack of skill in forecasting these events (Clark et al. 2007; Surcel et al. 2010; Kain et al. 2013; Bechtold et al. 2014; Pinto et al. 2015). Inaccuracies in forecasting the timing, structure,

location and evolution of MCSs over this region can sometimes result in a low-skill forecast days later over Europe, the North Atlantic, and even the Arctic through Rossby wave dynamics (Rodwell et al. 2013; Lillo and Parsons 2017; Rodwell et al. 2018; Parsons et al. 2019b).

Northward moisture flux by the NLLJ is responsible for transporting as much as one third of moisture into the continental United States (Helfand and Schubert 1995; Higgins et al. 1997). The advection of warm, moist air by the southerly NLLJ creates an elevated source for the Convective Available Potential Energy (CAPE) and the intensity of the NLLJ tends to be correlated with heavier rainfall (e.g, Arritt et al. 1997; Tuttle and Davis 2006). Weaker than normal NLLJs have been linked to droughts over the USGP (Hu et al. 2018). Recent modelling work by Hu et al. (2018) revealed anomalously weak NLLJs contributed to the "dust bowl" drought in the 1930s, as weaker NLLJs amplified drought conditions because of reduced moisture transport. It is suspected that changes in land-cover contributed to weaker NLLJs (Hu et al. 2018). In addition, Cook et al. (2009) found that land-cover changes during the 1930s were likely caused by agriculture. These findings suggest that processes associated with NLLJ formation are delicate enough to be disturbed by human activity, and variations of NLLJs associated with climate change may be detrimental for agriculture.

Studies have found that climate change may also alter moisture transport by the NLLJ, resulting in contrasting impacts depending on the region. These possible future impacts include a reduction of precipitation in the SGP and a greater risk of floods in the Mid-Western states (Cook et al. 2008; Barandiaran et al. 2013). Barandiaran et al. (2013) analyzed trends in the USGP low-level jet for the period 1979-2012 using North American Regional Reanalysis data and found trends in NLLJ intensity may explain precipitation trends suggesting decreased precipitation in the future. Precipitation trends analyzed by Barandiaran et al. (2013) were characterized by a 50% decline in precipitation in Oklahoma-Texas

during May which was associated with reduced NLLJ intensity. However there was an increase in precipitation in the Northern Great Plains (NGP) (north of 40°N). Extrapolation of observations by Barandiaran et al. (2013) are consistent with global climate simulations (GCMs) by Cook et al. (2008), which suggests a decreasing trend in precipitation over the SGP. Cook et al. (2008) found that these future climate conditions could also resemble the warm season of 1993 which was notable for its flooding in the Mid-Western United States. Future climate projections of less precipitation over the USGP demonstrate the need for accurately modelling NLLJs, as more accurate precipitation modelling may mitigate drought impacts to agriculture. However, more accurate modelling of NLLJs may be hindered by our uncompleted understanding of mechanisms driving NLLJs over the USGP.

One issue plaguing NLLJ research is the lack of consensus on the mechanism(s) responsible for explaining the geographical preference of NLLJs found by Bonner (1968). The sloping terrain of the SGP facilitates multiple mechanisms that explain NLLJ evolution (Holton 1967; Bonner and Paegle 1970; Paegle and Rasch 1973; Parish 2017). Having numerous mechanisms that may contribute to NLLJs pose a challenge for pinning down contributions by each of the mechanisms to NLLJ formation. Further complicating NLLJ research is that mechanisms proposed for explaining NLLJ climatology cover a range of scales, from planetary boundary layer (PBL) (Blackadar 1957) to mesoscale (Holton 1967; Bonner and Paegle 1970; Paegle and Rasch 1973) to synoptic scale (Uccellini and Johnson 1979). More detail on these mechanisms are provided in Section 1.3. Several studies have revealed that the synoptic flow pattern can have extensive impacts on NLLJ characteristics (e.g., Uccellini and Johnson 1979; Uccellini 1980; Igau and Nielsen-Gammon 1998; Walters and Winkler 2001; Walters 2001).

A source of difficulty in understanding why the NLLJ exhibits a geographical preference stems from contributions by both synoptic and sub-synoptic scale processes. In addition, these mechanisms may not be mutually exclusive, with multiple processes possibly contributing to these flow features. This study is motivated by the lack of understanding

on how mechanisms responsible for forming NLLJs vary with evolving synoptic conditions and what impacts such variations may have on facilitating convection.

1.2 Climatology of the Great Plains NLLJ

This study focuses on the NLLJ that occurs over the SGP region. One of the first climatological studies of the Great Plains NLLJ was conducted by Bonner (1968). His work examined rawinsonde data from two times: 1) 0000 2) 1200 UTC, for weak, moderate and strong NLLJs based the following criteria:

1. Wind at the level of wind maximum greater than 12 m s^{-1} and wind shear decreases by 6 m s^{-1} to the next wind maximum or to 3 km, whichever is lower.

2. Wind at the level of wind maximum greater than 16 m s^{-1} and wind shear decreases by 8 m s^{-1} to the next wind maximum or to 3 km, whichever is lower.

3. Wind at the level of wind maximum greater than 12 m s^{-1} and wind shear decreases by 10 to the next wind maximum or to 3 km, whichever is lower.

Using this criteria, the resulting climatology had a clear maximum of southerly NLLJs occurring in western Oklahoma, decreasing northward until South Dakota, eastward to Illonois, southward to the Gulf Coast in Texas and westward into the Texas Panhandle (Fig. 1.1). Subsequent climatological work has confirmed this geographical preference of the NLLJ found by Bonner (Helfand and Schubert 1995; Parish 2017).

One problem with Bonner's climatology is the two times used resulted in a lack of temporal resolution leaving aspects of NLLJ evolution occurring in-between these times not well understood. Wind profiler data utilized by Mitchell et al. (1995) allowed for the hourly examination of NLLJ intensity, which found a peak occurred between 0600-0900 UTC for Bonner category 3 low-level jets. A subsequent climatology by Whiteman et al. (1997) used rawinsonde data collected over a 2-year period at 8 times per day (0200, 0500, 0800, 1100, 1400, 1700, 2000 and 2300 UTC) from one site located in the SGP to gain

insight into NLLJ evolution, including timing of peak intensity and evolution of the height of the wind-maximum. Their study found a tendency for the wind maximum to occur at 355-553 m above ground level (AGL), they also found that the highest frequency of strong (Bonner category 3) low-level jets occurred with greatest frequency between 0500-1100 UTC. This timing of peak intensity for the strongest category of low-level jets over the SGP confirms the importance of nocturnal mechanisms in the forcing of NLLJs. Subsequent climatological work by Song et al. (2005) utilized wind-profiler data collected over a 6-year period and found that NLLJs occurred more frequently than that found in Whiteman et al. (1997)'s climatology and occurred at slightly lower heights (250-350 m). The additional number of years examined by Song et al. (2005) suggested that NLLJs were associated with larger scale patterns such as El-Nino Southern Oscillation (ENSO). However, one issue with these studies is the use of data from a single location, leaving questions on the spatio-temporal component of NLLJ evolution.

Later work by Berg et al. (2015) utilizing reanalysis products have confirmed findings of timing of the NLLJ from Whiteman et al. (1997) and (Song et al. 2005) that the NLLJ reached peak intensity between 0000-1200 UTC are not confined to a single site. The additional spatial resolution from reanalysis data also indicated that the location of the NLLJ shifted north overnight, going from Oklahoma at 0600 UTC to Kansas at 0900 UTC. Additional work by Danco and Martin (2018) utilizing simulation from phase 5 of the Coupled Model Intercomparison Project (CMIP5) and observational data confirmed findings by Whiteman et al. (1997) of the association between ENSO and low-level jets occurring over the USGP. Their study indicated a statistically significant correlation between the phase of ENSO was found in observations but was not well captured by models due to the associated affects on geopotential heights and atmospheric circulation.

The nocturnal timing of intensity found by climatological studies of low-level jets along with the association with larger scale patterns suggest mechanisms acting at a range of

scales are important for explaining the geographical preference of the NLLJ. The following section will examine several of these proposed mechanisms.

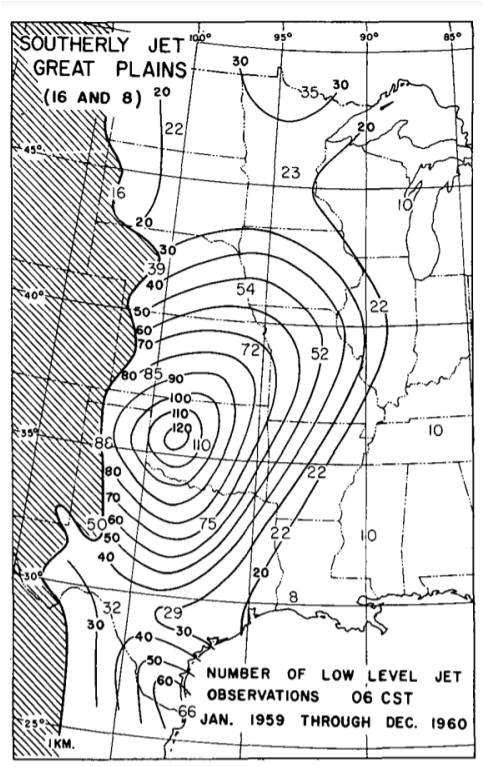

Figure 1.1: Climatology of Bonner (1968) criteria 2 southerly low-level jets over the central United States. Taken from Bonner (1968).

1.3 Mechanisms for the NLLJ

This section provides a brief overview of mechanisms proposed for explaining the climatological maximum of NLLJs over the SGP region.

1.3.1 The Inertial Oscillation

One of the earliest proposed mechanisms for explaining the climatological maximum of the NLLJ in the SGP was given by Blackadar (1957). Blackadar (1957) proposed that the occurrence of the NLLJ resulted from an inertial oscillation (IO) caused by the cessation of daytime turbulent mixing in the boundary layer near sunset, producing a wind-maximum

near the height of the boundary layer inversion. The IO proposed by Blackadar (1957) results in supergeostrophic winds as the Coriolis force acts on an acceleration in the direction of the pressure gradient force (PGF) that is produced when frictional forces in the daytime PBL are no longer acting on the wind. This IO is characterized by the ageostrophic wind vector rotating clockwise around the geostrophic wind vector with time, producing the largest supergeostrophic enhancement when the ageostrophic and geostrophic components of the horizontal wind are aligned. Several studies have found that NLLJs occurring over the USGP exhibit characteristics similar to those produced from an IO (Parish et al. 1988; Mitchell et al. 1995; Parish and Oolman 2010; Fedorovich et al. 2017). Potential issues with this mechanism explaining the Bonner climatology are: 1) Blackadar (1957) assumed constant geostrophic winds when formulating this mechanism, and 2) Since boundary layer decoupling is not localized to the SGP, this mechanism by itself cannot explain the geographic preference of the NLLJ.

1.3.2 Seasonal Heating

Later work has found that heating along the slope of the SGP during the summer months creates a favorable PGF for the development of southerly NLLJs from the Blackadar's IO mechanism (Parish et al. 1988; Parish and Oolman 2010; Parish 2016, 2017; Parish and Clark 2017; Parish et al. 2020). Parish (2016) constructed composites of isobaric temperatures over the SGP during low-level jet events that occurred during June and July of 2008 and 2009 using data from the North American Mesoscale Forecast System model (NAM). These composites suggested that the effects of daytime heating combined with an IO may explain NLLJ climatology. Later work by Parish (2017) used composites constructed from the NAM over a 5 year period during the months of June and July to examine forcing mechanisms of NLLJs by dividing NLLJ cases by strong and weak jets. Using this technique Parish (2017) found that strong low-level jets had a much greater isobaric temperature gradients at the level of the jet, consistent with the effects of a thermal low from daytime

heating. Parish proposed that these two effects, mean seasonal heating and the IO can explain the climatological maximum of the NLLJ. The combination of an IO with mean seasonal heating may be an oversimplification as it relies on the Blackadar's assumption of constant geostrophic winds, observations of NLLJs suggest this is not always the case. One example documented by Parish (2016) found a nocturnal intensification of the geostrophic winds that was a fundamental departure from their low-level jet composites.

1.3.3 Baroclinic Influence

In contrast to work by Parish, previous studies have found more substantial diurnal oscillations of low-level geostrophic winds associated with NLLJs (Bonner and Paegle 1970; Paegle and Rasch 1973). Bonner and Paegle (1970) inferred low-level geostrophic winds by using the surface buoyancy gradients over the sloping terrain of the SGP and found the along-slope PGF exhibited diurnal oscillations on the order of 5-9 m s^{-1} over western Oklahoma and Texas. These diurnal oscillations of the geostrophic winds have been explained through baroclinic effects that may take place over sloping terrain (Holton 1967; Bonner and Paegle 1970; Paegle and Rasch 1973).

Specifically, Holton (1967) proposed that a thermal wind reversal may take place with uniform heating along sloped terrain. This thermal wind reversal is said to occur when the surface cools more rapidly upslope than in the residual layer at the same heights to the east. This mechanism may act together with the IO mechanism to produce dramatic changes in NLLJ structure as found in analytical work by Shapiro et al. (2016) which unified the IO and thermal wind reversal mechanisms. Shapiro et al. (2016) found that NLLJs produced by their analytical model were more similar to those observed in the SGP than those produced by the two mechanisms on their own. In addition to the Shapiro et al. (2016) analytical model producing the well known southerly wind maximum (v_{max}), a westerly wind maximum (u_{max}) was found to occur just above the v_{max}.

It is well known that differential heating over the slope often results in buoyancy gradients (e.g, Sun and Ogura 1979; Anthes et al. 1982; Benjamin 1986; Kaplan et al. 1984; Parsons et al. 1991; Sun and Wu 1992; Gebauer and Shapiro 2019). This buoyancy gradient has been attributed to: differences in soil moisture, vegetation, and cloud cover air producing a pressure gradient with an upslope component to the surface winds (e.g, Sun and Ogura 1979; Anthes et al. 1982; Benjamin 1986; Kaplan et al. 1984; Parsons et al. 1991; Sun and Wu 1992). Bonner and Paegle (1970) found that the effects of non-uniform heating along sloped terrain can influence low-level jet structure. Gebauer and Shapiro (2019) used composites of Oklahoma Mesonet surface data to examine relative contributions from the effects of uniform heating and differential heating along the slope, their results suggested that both mechanisms produced thermal wind effects of 3-4 m s^{-1}. When trying to link surface thermal gradients to soil moisture, Gebauer and Shapiro (2019) found a surprising lack of correlation between months with the greatest soil moisture gradients and thermal gradients.

1.3.4 Other Contributing Factors

In addition to influencing low-level jet structure, along-slope non-linear thermal gradients occur and are known to favor the development of surface boundaries known as drylines (Carlson and Ludlam 1968; Schaefer 1974a; Sun and Ogura 1979; Sun and Wu 1992). Modelling work by Sun and Ogura (1979) found that the effects of differential surface heating observed with drylines produced a thermally driven circulation with ascending air on the warm side of the boundary and descending air on the cool side. Sun and Wu (1992) found drylines could develop under synoptically quiescent conditions over sloping terrain given favorable low-level wind shear and soil moisture gradients. In addition, Sun and Wu (1992) found that downward mixing of westerly momentum on the dry side promoted eastward movement during the day, as mixing ceased an IO acting on the easterly component of the wind on the moist side of the boundary caused a westward movement of the boundary

and resulted in the formation of a NLLJ on the moist side. Southerly NLLJs have often been observed on the moist side of a retrogressing dryline (e.g, Parsons et al. 1991; Ziegler and Hane 1993; Parsons et al. 2000), Parsons et al. (1991) observed an elevated low-pressure perturbation occurring on the moist side of a retrogressing dryline. Later work by Ziegler and Hane (1993) speculated that this pressure perturbation may be dynamically forced, resulting when the retrogressing dryline advances westward behaving like a density current and proposed that this may explain the formation of NLLJs associated with retrogressing drylines. Evidence for retrogressing drylines behaving as density currents was found by Geerts (2008) using 2-months of Texas Mesonet data, found that the $\Delta\theta_v$ and propagation speed of retrogressing drylines was consistent with density current characteristics. There is a lack of work considering the impacts of this diurnal evolution of non-linear thermal gradients on NLLJ evolution within the context of a retrogressing dryline.

The solenoid circulation associated with drylines have been associated with the westward propagation of convective precipitation that develops over the High Plains during the late afternoon and propagates east overnight (Carbone et al. 2002), suggesting that this circulation may continue to be important overnight. Using composites constructed from North American Regional Reanalysis (NARR) data, Pu and Dickinson (2014) found that regions of convergence associated with this solenoid circulation shifted east overnight, and proposed that this shift was the result of the reversal of the solenoid circulation. More specifically, Pu and Dickinson (2014) found that sinking motion developed to the west overnight along with downslope flow, and suggested that the NLLJ and convergence occurred as a mass response to balance the reversal of the circulation. Other authors have noted flaws with this argument, Shapiro et al. (2018) noted that such changes to vorticity could occur due to stretching of earth's relative vorticity for the scales of analysis used by Pu and Dickinson (2014), and Parish et al. (2020) argued that the PGF was not favorable for downslope drainage flow. Despite these criticisms, analysis by Pu and Dickinson (2014) does show an association between the vertical motion pattern and NLLJs.

Although sub-synoptic scale mechanisms are important for explaining NLLJ climatology over the SGP, Uccellini and Johnson (1979) proposed that low-level jets may develop when upper-level divergence associated with a jet streak induces a low-level mass response. Low-level jets occurring under such conditions are often referred to as coupled low-level jets (c-LLJs). Subsequent analysis of 15 NLLJ/c-LLJ events by Uccellini (1980) was consistent with low-level jets being influenced by such a synoptic flow regime. In these cases they found a trough or jet streak was located over or just to the west of the Rockies and surface pressure falls over the Texas Panhandle and western Oklahoma exhibited an eastward trend, coinciding with the eastward movement of the c-LLJ. Uccellini (1980) found c-LLJs still exhibit a nocturnal intensification, suggesting that sub-synoptic scale processes are still influencing low-level jet evolution under active synoptic conditions.

Along with upper-level divergence, synoptic scale fronts may be another potential mechanism contributing to to the formation of low-level jets (Browning and Pardoe 1973; Hsie et al. 1984; Lackmann 2002). Browning and Pardoe (1973) suggested that low-level jets formed within the warm conveyor belt as part of a corkscrew-like circulation associated with extra-tropical cyclones. Further work by Lackmann (2002) found that potential vorticity (PV) anomalies associated with cold fronts may contribute to intensity of low-level jets occurring within warm-conveyor belts.

Numerous studies examining how synoptic flow influences NLLJ development find that more intense NLLJs are associated with an active synoptic pattern, characterized by a jet-streak located west of the Rockies (Uccellini 1980; Igau and Nielsen-Gammon 1998; Walters 2001). The tendency for strong NLLJs to occur in active synoptic environments appears to support for the idea that synoptic flow influences NLLJ development over the SGP. However, some studies have found that the upper-level coupling mechanism proposed by Uccellini and Johnson (1979) has difficulty explaining some aspects of NLLJ development (Walters and Winkler 2001; Walters 2001). In a two part study, Walters and Winkler (2001)

and Walters (2001) used composites of NLLJs exhibiting similar flow characteristics (orientation, diffluence field and latitudinal extent) to try and link low-level jets exhibiting different configurations to specific synoptic flow regimes. They found that most low-level jets occurring in active environments took place when the upper-level flow was not favorable to induce a mass response proposed by Uccellini and Johnson (1979), with these low-level jets forming near the lower right quadrant of a jet streak. This result was an unexpected finding given that the flow field in the of the low-level jet was consistent with a transverse circulation. Walters and Winkler (2001) speculated that a transverse circulation associated with a dryline may offer an explanation based on the moisture field associated with this type of low-level jet. Interestingly, this low-level jet configuration was also found to exhibit a westerly maximum occurring below 700 hPa but above the southerly low-level jet, similar to that expected by the Shapiro et al. (2016) analytical model. As with NLLJs documented during PECAN (Gebauer et al. 2018; Smith et al. 2019), convergence was associated with heterogeneous characteristics of the westerly low-level in composites analyzed by Walters and Winkler (2001). The finding that westerly NLLJs are more common under active synoptic conditions further complicates pinning down mechanisms responsible for NLLJs in the SGP and suggests that a broad range of scales should be considered when investigating mechanisms driving their formation.

Understanding how NLLJs interact with synoptic scale flow may be important for understanding seasonal variations in the hydrological cycle over the USGP (Wang and Chen 2009). A well documented late-spring maximum (May-June) in precipitation occurs over the central USGP (e.g, Nigam and Ruiz-Barradas 2006). At this time the region is a net moisture sink, followed by becoming a net moisture source during the summer months (July-August) (Roads et al. 1994; Gutowski Jr et al. 1997; Ropelewski and Yarosh 1998). Wang and Chen (2009) examined the role of the NLLJ in this late spring hydrological shift using reanalysis data from 1979 to 2002 and categorizing low-level jet events by whether or not they were coupled with upper-level flow. Their results found that 70% of rainfall

over the central plains was linked to low-level jets, and 75% of precipitation associated with low-level jets was associated with upper-level coupled low-level jets.

1.4 The NLLJ as a Trigger for Deep Convection

Wilson and Roberts (2006) found convergence and conditional instability above the nocturnal boundary layer were critical factors in initiating nocturnal convection during the International H2O project (IHOP_2002) (Weckwerth et al. 2004). Subsequently, the Plains Elevated Convection At Night (PECAN) project (Geerts et al. 2017) that took place during June and July 2015 over the US Great Plains was designed to investigate nocturnal convection within the NLLJ environment including convective initiation (CI) events. Trier et al. (2017) investigated CI events during PECAN finding strong synoptic forcing (e.g., cold fronts, short waves), the NLLJ interacting with a quasi-stationary front as in (Trier and Parsons 1993), and events that took place without strong synoptic forcing, fronts or surface boundaries. Weckwerth et al. (2019) subsequently examined nocturnal CI events during PECAN and found that CI fell into several categories: 1) frontal overrunning, 2) the LLJ, 3) a preexisting mesoscale convective system (MCS), 4) a bore or density current, and 5) a nocturnal atmosphere lacking a clearly presence of the other forcing (i.e., termed pristine CI). While dynamic frameworks for CI due to lifting by density currents (e.g., (Rotunno et al. 1988; Liu and Moncrieff 2000), bores (Wilson and Roberts 2006; Parsons et al. 2019a; Loveless et al. 2019), and stationary fronts (Maddox et al. 1979; Trier and Parsons 1993) in this environment are relatively well understood, the reasons for CI driven by the NLLJ and pristine events is less clear. In addition to a lack of understanding of CI associated with NLLJs, accurate prediction of CI associated with bores may depend on the correct modelling of the NLLJ (Haghi and Durran 2021).

Several mechanisms have been proposed to explain CI in the vicinity of the NLLJ that occurs apart from density currents, bores and fronts. For example, Reif and Bluestein (2017) undertook a 20 year climatology in the vicinity of the NLLJ over this region and

found two main peaks in the timing of CI with the later peak taking place in the absence of a nearby surface boundary. Through examination of case studies of three nocturnal CI events that occurred during PECAN, Reif and Bluestein (2017) proposed that quasi-geostrophic ascent associated with warm air advection was a possible cause of the CI. However, the pronounced ageostrophic component of the NLLJ, which has been shown to extend well above the southerly wind maximum by Rattray et al. (2018) suggests the use of quasi-geostrophic theory alone to predict the magnitude of ascent for CI needs to be further examined as also noted by Gebauer et al. (2018).

Further linkage between the occurrence of warm advection and CI can be found in the Wilson et al. (2018) study that observed CI taking place in the presence of warm advection, but with gravity waves causing additional ascent associated with the CI event. Trier et al. (2017) also found that the advection of warm air with high water vapor content and persistent vertical motions contributed to the development of elevated, approximately saturated layers with lapse rates greater than moist adiabatic. These layers were favorable for CI. These results are consistent with earlier findings, such as the classical Maddox (1983) study that investigated the environment near large mesoscale convective complexes and found the presence of warm advection and ascent in association with the NLLJ.

Other mechanisms for ascent in association with the NLLJ include Pu and Dickinson (2014) that argued a decrease in the intensity of the NLLJ during the night would induce ascent to compensate for a local changes in the vertical voricity balance. Their study suggested this mechanism would result in ascent east of the NLLJ core late in the night as the intensity of the NLLJ decreased. Shapiro et al. (2018) argued flaws existed in that vorticity balance argument and instead proposed persistent, gentle mesoscale ascent in the lower troposphere would develop from an inertia–gravity wave response due to the sudden decrease of turbulent mixing in the convective boundary layer. In the Shapiro et al. (2018) mechanism, the ascent would be centered on lateral maximum in buoyancy field within the convective boundary layer. Gebauer et al. (2018), investigating one of the events studied

in Trier et al. (2017) found convergence and moisture advection was occurring at the top eastern edge of a veering NLLJ leading to moist saturated layers as noted by Trier et al. (2017). Gebauer et al. (2018) proposed that this favorable NLLJ structure with veering of the NLLJ was driven by non-uniform heating on the sloped terrain. The Gebauer et al. (2018) study shows the need to consider the full three-dimensional structure of the NLLJ for nocturnal CI including the maximum in the westerly winds noted earlier. Through utilizing high resolution observations taken during PECAN along with numerical simulations, Smith et al. (2019) found CI could be influenced by local events since the NLLJ structure significantly in time and space with the westerly maximum playing a significant role.

Squitieri and Gallus Jr (2016a) examined the correlation between southerly NLLJ and MCS error in environments with weak synoptic forcing (referred to as type A low level jet in their paper) and found simulations had difficulty with timing and location of CI. These errors could not be explained by errors in southerly NLLJ moisture, MUCAPE or MUCIN. In a follow up study Squitieri and Gallus Jr (2016b), and suggested mass convergence associated with the NLLJ may offer an explanation but could not find a clear signal to support this hypothesis. Given findings by Gebauer et al. (2018), perhaps the lack of signal was a result of their focus only on levels near the height of the southerly NLLJ. Parsons et al. (2019a) constructed composites of the vertical profiles of CAPE and CIN and found the most favorable conditions for deep convection were found in the day-time boundary layer. Thus, they suggested that nocturnal convection might arise from ascent that is intermittent in time and/or localized along the slope. The heterogeneous nature of the NLLJ may provide an explanation for the spatial-temporal variability of CAPE and CIN overnight. A better understanding on how the evolution of the two wind-maximum NLLJ influences the distribution of CAPE in time and space may help identify deficiencies in models and increase the ability to accurately forecast nocturnal convection.

1.5 Objectives

This study will address knowledge gaps in our current understanding of the NLLJ by using observational data to document the day-to-day evolution of the NLLJ after a cold-frontal passage and its role in returning convectively unstable conditions to the region. This will be addressed by answering the following two questions:

1. What is the day-to-day evolution of the NLLJ after a cold frontal passage has diminished the thermal gradients along the slope?

2. How does this evolution facilitate convection?

This approach will provide insight into how NLLJs evolve as boundary layer mixing and thermal gradients return to the region and also provide a synoptic framework for the NLLJ that considers how mechanisms driving NLLJs change with synoptic flow becoming more active with each subsequent day. This study will also document how evolution of the NLLJ coincides with the development of more convectively favorable conditions. This approach will provide a source of documentation for future investigations into precipitation extremes over the region.

Chapter 2

Methods

2.1 IHOP_2002 Observational Data

The research in this thesis makes use of observations taken during the International H_20 Project (IHOP_2002) that took place from 15 May 2002 to 25 June 2002 over the SGP. A summary of the experimental design and research goals for IHOP_2002 can be found in Weckwerth et al. (2004). Specifically, the IHOP_2002 goals were focused on obtaining an improved characterization of the time varying 3-D distribution of water vapor to advance our understanding and prediction of convective processes. The experimental domain for the IHOP_2002 field campaign is shown in Fig. 2.1 and included a wide variety of fixed and mobile ground-based instrumentation. In addition, six research aircraft were utilized in IHOP_2002.

This thesis makes use of rawinsonde measurements taken at five sites operated by the Department of Energy's Atmospheric Radiation Measurement Program (ARM) (Stokes and Schwartz 1994; Mather and Voyles 2013). The rawinsonde launches were made from these ARM sites at 3 h intervals from 25 May to 15 June 2002. Each rawinsonde measured temperature, relative humidity, wind speed, and pressure as a function of height at a frequency of 2-s. Measurements from the rawinsondes in this study were used to document the structure and evolution of the NLLJ and to evaluate the stability of the atmosphere for deep convection over the region. The spatial configuration of these ARM sites (Fig. 2.2) included a central facility at Lamont, Oklahoma (hereafter referred to as: central site) and four boundary facilities surrounding this central site with Vici, Oklahoma to the west (hereafter referred to as: western site), Hillsboro, Kansas to the north (hereafter referred to as: northern site), Morris, Oklahoma to the east (hereafter referred to as: eastern site), and Purcell, Oklahoma to the south (hereafter referred to as: southern site). This work focuses

on data collected during the hours: 0000-1200 UTC, since the cessation of mixing within the boundary layer occurs near 0000 UTC and 1200 UTC is the last sounding time before the boundary is impacted by the morning transition.

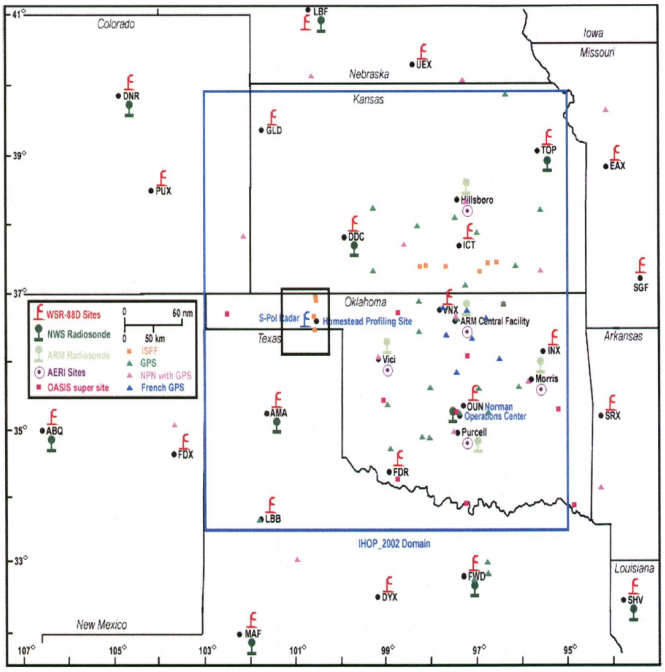

Figure 2.1: Locations of sites and instruments used during the IHOP_2002 field campaign. From Weckwerth et al. (2004).

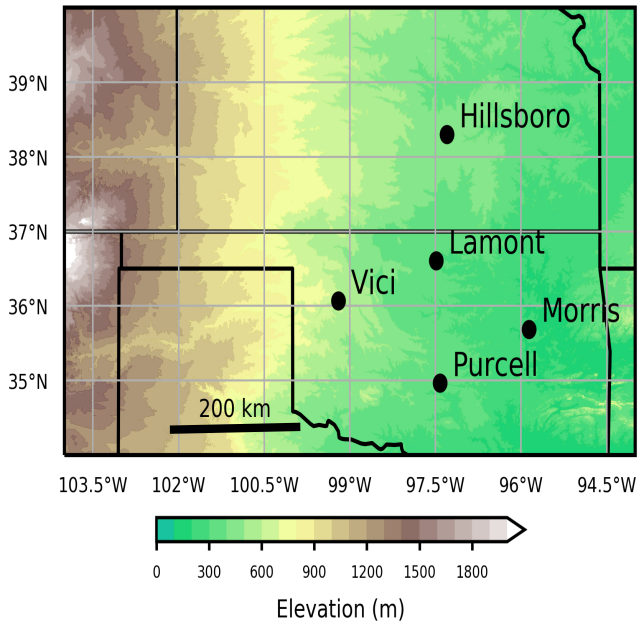

Figure 2.2: The five Department of Energy's ARM sites where 3 h rawindsondes were deployed during IHOP_2002.

2.1.1 Calculation of Spatial Gradients

Gradients at the central site were calculated for these radiosonde data using centered-differencing scheme with north-south gradients computed using the difference between the northern and southern sites, and the east-west gradients using the difference between the western and eastern sites. The horizontal distance between the western and eastern sites was $\sim$300 km, while the distance between the northern and southern sites was slightly farther at $\sim$330 km. Calculations requiring gradients between the ARM sites were performed on isobaric surfaces with the Sounding Hodograph Analysis and Research Program in Python (SHARPpy) toolkit (Blumberg et al. 2017) used to interpolate variables to constant height surfaces and pressure levels. Variables which required calculation of gradients at the ARM

sites were: vertical velocities (w), horizontal divergence (δ), temperature and moisture advection and the wind components (geostrophic components (u_g and v_g) and ageostrophic components (u_a and v_a)). The following is how these variables were calculated:

2.1.1.1 Vertical Velocities and Divergence

Vertical velocities were calculated using the kinematic method (Bluestein 1992):

$$\omega(P) = -\int_{p_0}^{P} \delta dP' + \omega_0 \tag{2.1}$$

where pressure p is the level where ω is calculated, p_0 is the pressure level nearest to the surface and pressure P' is a dummy variable over which the integrand is being integrated. The pressure level nearest to the surface common to all sites in this analysis was $\sim$940 hPa. The lower kinematic boundary condition was calculated from:

$$w_0 = (\frac{Dz}{Dt})_0 = (\frac{\partial z}{\partial x}\frac{Dx}{Dt} + \frac{\partial z}{\partial y}\frac{Dy}{Dt})_0 \tag{2.2}$$

w_0 was then converted to ω_0 with:

$$\omega = \frac{\partial P}{\partial t} + V \cdot \nabla p + w\frac{dP}{dz} \tag{2.3}$$

Using the hydrostatic equation:

$$\frac{dP}{dz} = -\rho g \tag{2.4}$$

and assuming the first and second term on the RHS are at least an order of magnitude less than the last term on the RHS (typically valid for synoptic scales (e.g, Holton 1973)) yields:

$$\omega_0 \approx -\rho g w_0 \tag{2.5}$$

where g is gravitational acceleration (9.81 m s^{-1}) and ρ is the density of air at the surface. We are assuming that the surface ω is defined by the slope of the terrain, which may not hold in the case of strong advection or synoptic forcing, and It should be noted that this

approximation is one potential source of error. However, the magnitudes vertical velocities calculated below 500 m were < 1 cm s^{-1} in all cases that were examined, and tended to be relatively small compared to the magnitudes aloft. In addition, to help mitigate errors resulting from this calculation, θ_v profiles will be examined for expected impacts of ascent.

The calculation of divergence and the vertical motions at 3-hourly interval allowed insight into the processes creating a more favorable environment for deep convection and allowed comparison with mechanisms proposed in past studies.

2.1.1.2 Temperature and Moisture Advection

As pointed out earlier, temperature and moisture advection associated with the NLLJ may help facilitate nocturnal convection (e.g, Maddox 1983). More recent work has suggested that advection of buoyancy gradients by the westerly component of the NLLJ may contribute to the evolution of the southerly NLLJ (Gebauer et al. 2018; Smith et al. 2019) in addition to its potential contribution to facilitating convection. To better understand NLLJ evolution and nocturnal convection, horizontal advection was calculated using:

$$-\mathbf{V} \cdot \nabla \phi \tag{2.6}$$

where $\mathbf{V} = \mathbf{i}u + \mathbf{j}v$ is the horizontal velocity vector at the central site, ϕ is the variable being advected and $\nabla\phi$ is the gradient of the variable being advected.

Our advection calculations focused on the advection of temperature and water vapor. These quantities are relevant to convective initiation and to the NLLJ dynamics, especially given the proposed importance of horizontal advection by the westerly winds to the previously discussed concept of a heteorogeneous NLLJ.

2.1.1.3 Wind Components

The calculation of the geostrophic and ageostrophic winds were undertaken since past studies have clearly illustrated the importance of the geostrophic and ageostrophic winds to the

NLLJ dynamics. The wind can be broken up into geostrophic and ageostrophic components:

$$\mathbf{V} = \mathbf{V}_a + \mathbf{V}_g \tag{2.7}$$

and $\mathbf{V}_g$ is calculated with:

$$\mathbf{V}_g = \frac{1}{f}\mathbf{k}\ \mathbf{x}\ \nabla_p \Phi \tag{2.8}$$

where Φ is the geopotential of an isobaric surface and f is the Coriolis parameter:

$$f = 2\Omega sin\phi \tag{2.9}$$

with Ω = 7.292 x 10^{-5} rad s^{-1} and where ϕ is the latitude.

The partitioning of the winds into geostrophic and ageostrophic components provided insight into low-level jet dynamics and their relative role in temperature and moisture advection. The proportion of temperature advection associated with the geostrophic component has implications on whether quasi-geostrophic (QG) theory can be applied to explain ascent associated with the NLLJ. For example, ω associated with the QG-advection term states that it is advection by the geostrophic component of the wind.

2.2 ERA5 Reanalysis Data

Even though the spatial and temporal resolution of ARM rawinsonde data is sufficient to capture many key aspects NLLJ evolution, 3-h gaps still exist in data and spatial extent is limited to the five sites. In addition, mesoscale processes occurring near but outside the domain of the ARM sites may be influencing NLLJ evolution. To mitigate these gaps in ARM rawinsonde data, our analysis is supplemented with data from the European Centre for Medium-Range Weather Forecasts (ECMWF) ERA5 reanalysis (Hersbach et al. 2020). The spatial and temporal resolution of the ERA5 provides sufficient resolution to examine mesoscale features that may influence NLLJ evolution. The ERA5 has a 31 km horizontal, 1-h temporal and 25 hPa vertical resolution. ERA5 data displayed in figures includes fields that were directly obtained or calculated from directly obtained fields.

Calculations and interpolations with ERA5 data were performed with the Metpy Python library (May et al. 2008 - 2020), this library was used for several reasons. First, Metpy contains a comprehensive list of meteorological calculations. Second, Metpy is able to read metadata from commonly used meteorological reanalysis and numerical model data files. Since Metpy automatically reads metadata from these files, this means that calculations always have the correct units, thus reducing the chance of errors in calculations. Another benefit of Metpy's ability to read metadata is that coordinate information is also automatically obtained, this converts latitude's and longitude's into distances required for calculations of spatial gradients, as well as the latitude for calculating the Coriolis parameter. The third reason Metpy was used is that it is able to interpolate data. These interpolation routines include: 1-D interpolation, interpolation to iso-surfaces (ie. from isobaric to height surface or vice-versa) and interpolation for vertical cross-sections.

Variables that were calculated from ERA5 data include: geostrophic and ageostrophic winds, w, horizontal advection, pressure perturbations, θ_v and mixing ratio. All other fields used in displays of ERA5 data were standard fields that were directly obtained. ERA5 data were also used to construct zonal (A to C in Figure 2.3) and meridional (E to D in Figure 2.3) cross sections to help provide insight into mesoscale processes that may be influencing NLLJ evolution. Data on isobaric surfaces were interpolated to height surfaces every 10 m up to 8 km above mean sea level (MSL). In addition, to provide a spatial overview of NLLJ intensity, ERA5 data was interpolated to height above ground level (AGL). This was done by first interpolating data to height above MSL surfaces and then subtracting the height of the terrain, which is a field from ERA5 data. The peak v and u components below 2 km AGL were used as estimates for the southerly and westerly NLLJs respectively.

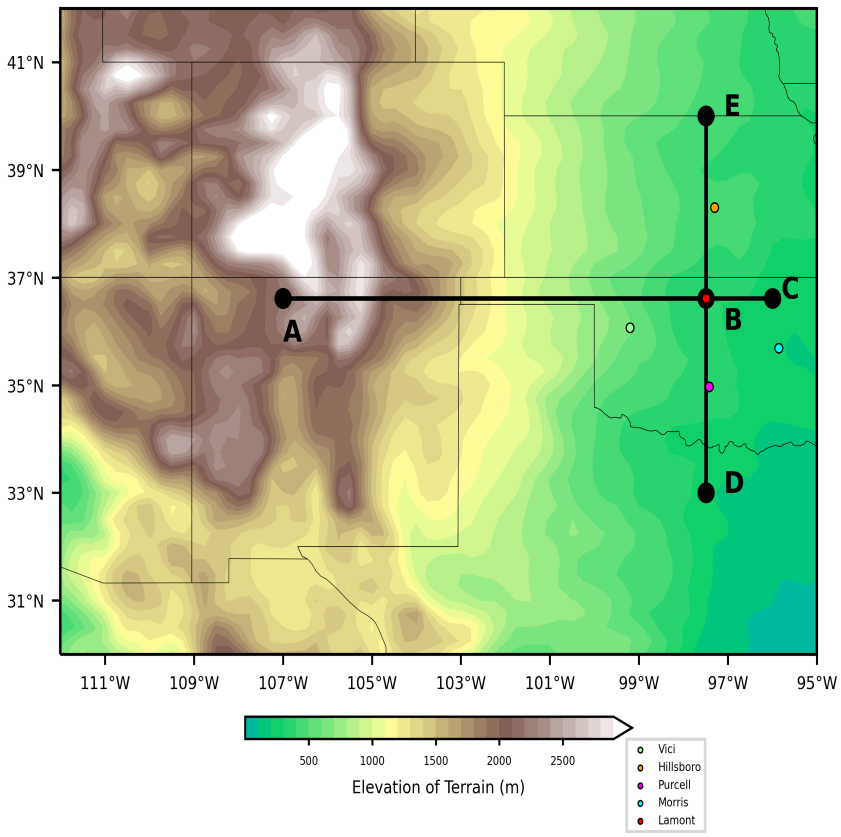

Figure 2.3: Locations of zonal (A to C) and meridional (D to E) cross sections, intersecting at the central ARM facility (Lamont, B). Also plotted are: 5 ARM site locations and height of topography obtained from ERA5 reanalysis data.

2.3 Recovery Periods

This thesis focused on the evolution of the NLLJ following the passage of two cold fronts through the IHOP_2002 domain. The dates during IHOP_2002 occurring in-between cold-front passages are described as recovery periods in this Thesis. Categorizing dates by recovery periods allows for the study of the underlying processes influencing the day-to-day intensification of the NLLJ, as cold fronts will disrupt mesoscale baroclinic zones often associated with NLLJ development. Analysis from the National Oceanic and Atmospheric Administration (NOAA) Weather Prediction Center (WPC) indicates that cold fronts moved through the domain on 25 May, 5 June, and 13 June (Fig.2.4). The period of dates from 26 May to 4 June will be referred to as the first recovery period, and the period of dates from 6 to 11 June will be referred to as the second recovery period (12 June was omitted due to convection over the ARM sites).

An overview of the day-to-day evolution in each recovery period is provided in Chapter 3, providing insight into the evolution observed after the two frontal passages. Subsequently, a greater focus is given to NLLJ evolution during the second recovery period since this period contains a more complete data-set. The second recovery period was selected for a more thorough examination of NLLJ evolution and of the role of the NLLJ in facilitating convection through the return of unstable conditions.

Specifically, to examine NLLJ evolution and the return of unstable conditions, the second recovery period is divided into phases and one date is selected from each phase. The phases and corresponding dates are as follows; pre-moistening phase (7 June), moistening phase (8 June) and post-moistening phase (10 June). This selection of dates allows for the added bonus of utilizing the analysis by Tollerud et al. (2008) which examined mesoscale moisture transport by the low-level jet over Kansas on 9 June 2002 using aircraft and lidar data collected for IHOP_2002. Their analysis of moisture transport by the NLLJ will be compared with analysis of moisture transport from the other dates analyzed in this thesis in

Chapter 3 to provide a more complete picture of how the NLLJ is contributing to the return of moisture over these dates.

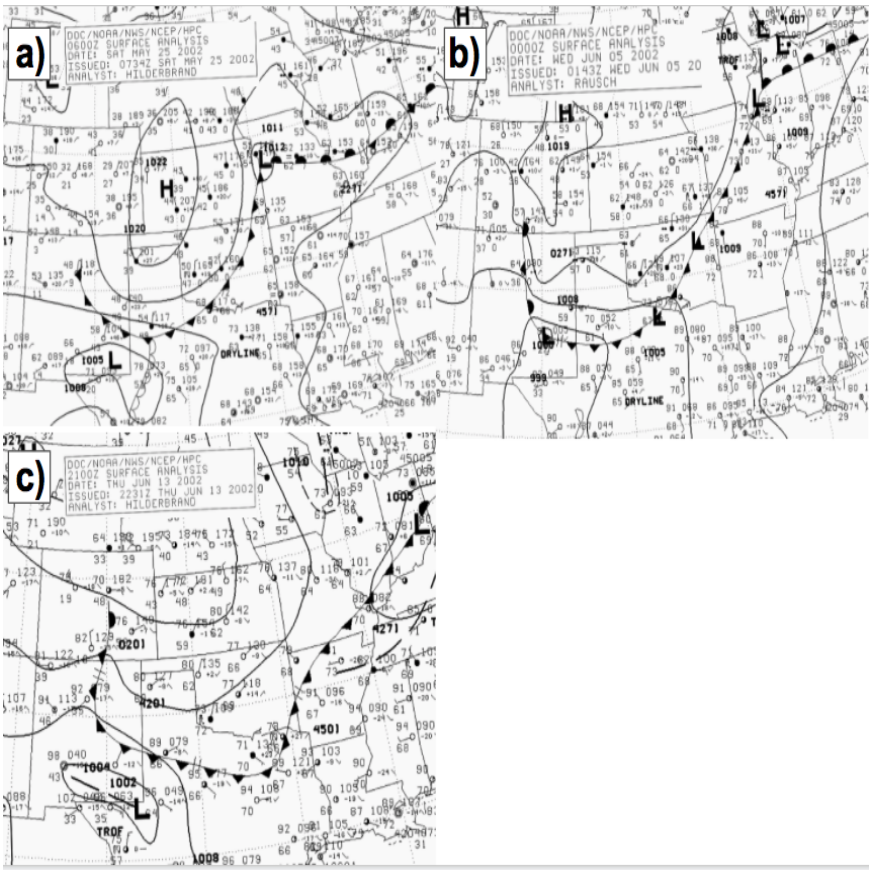

Figure 2.4: Cold frontal passages over the Southern Great Plains during IHOP_2002, as analyzed from the National Oceanic and Atmospheric Administration (NOAA) Weather Prediction Center (WPC) at times a) 0600 UTC 25 May 2002, b) 0000 UTC 5 June 2002 and c) 2100 UTC 13 June 2002.

Chapter 3

Overview

This chapter begins by examining the synoptic conditions within the first and second recovery periods to provide context of the synoptic scale environment where NLLJ evolution was taking place. This analysis is followed by an overview of the evolution of the NLLJ during the two recovery periods during IHOP_2002 and how this evolution impacted moisture return. In both recovery periods the NLLJ strengthened in the days following the passage of the cold front. This discussion is followed by an overview of NLLJ evolution during the first (30 May-4 June 2002) and second recovery period (6-11 June 2002) at Lamont. The final section of this chapter summarizes NLLJ evolution described in this chapter.

3.1 Synoptic Conditions

To provide the synoptic context for the two recovery periods, the average winds at 700 hPa for two periods were obtained from the ERA5 Reanalysis 3.1. This pressure level was selected since it was relatively close to heights where the peak westerlies occurred during the second recovery. In the 700 hPa flow, the mean winds over the domain during this first recovery period (Fig. 3.1a) were characterized by a cyclonic flow around a low located to the south-southeast of the domain and slight ridging to the north resulting in quite light winds with an easterly component over southern Oklahoma and a western component just over the border in southern Kansas. In contrast, the second recovery period had southwesterly winds of 5-10 m s^{-1} or greater over the domain ahead of a trough with stronger winds to the west (Fig. 3.1b).

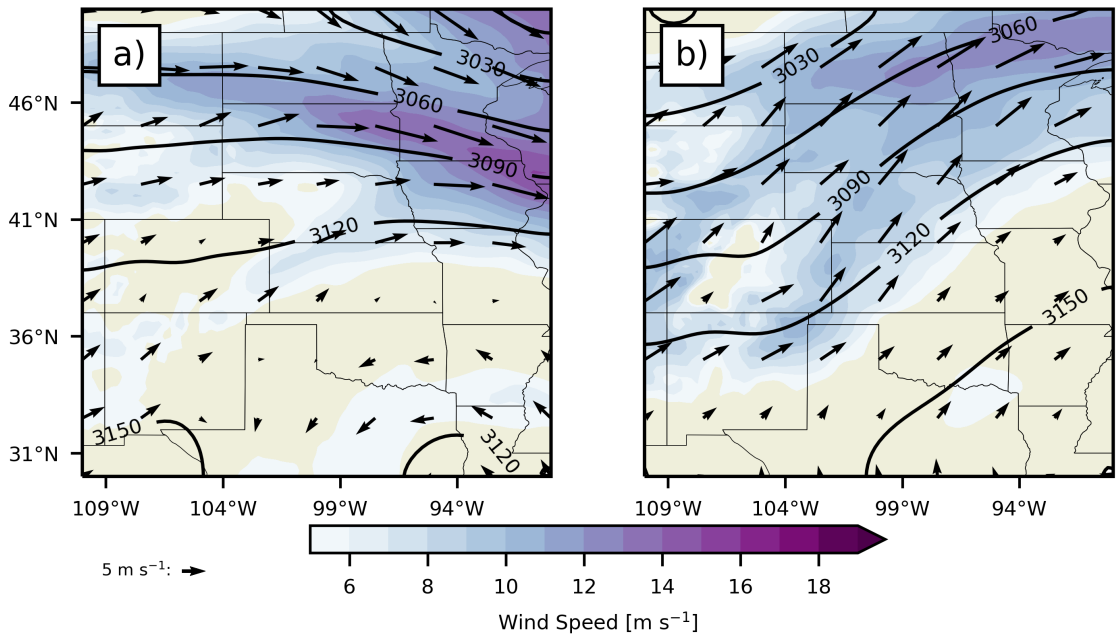

Figure 3.1: 700 hPa level geopotential height contours (hPa), wind vectors and wind magnitudes shaded (m s^{-1}) shaded and 700 hPa from the ECMWF ERA5 reanalysis. a) Composite of the 1st period, 30 May to 4 June 2002; b) Composite of the 2^{nd} period, 6 to 12 June 2002.

3.1.1 Moisture Return

Vertically integrated moisture fields from the ERA5 indicate that moisture divergence took place over the ARM sites which was associated with negative meridional moisture flux (Fig. 3.2). The 5 June cold frontal passage was associated with negative meridional moisture flux, going from 350 kg m^{-1} s^{-1} on 4 June to -100 kg m^{-1} s^{-1} on 6 June, corresponding to a peak in moisture divergence, consistent with the cold front resulting in the drying of the overlying airmass at the ARM sites. Following the 5 June frontal passage, intensification of meridional moisture flux followed a near linear trend until 1200 UTC on 9 June, at which point it was $\sim$500 kg m^{-1} s^{-1}, with a local maximum of moisture convergence occurring from 8-9 June. This moisture convergence suggests that the set of dates during the second

recovery period is still within the late-spring regime noted by Wang and Chen (2009) where upper-level coupled low-level jets contribute to 70% of precipitation.

Moisture return during the second recovery period at the central ARM site was initially characterized by a relatively dry boundary layer (mixing ratio values of $<$8 g kg^{-1}) for the first two days after the 5 June frontal passage, followed by a period of rapid moistening which occurred on 8 and 9 June. During the period of rapid moistening mixing ratio within the boundary layer increased from $\sim$8 g kg^{-1} to $\sim$14 g kg^{-1}. After the period of rapid moistening, values of mixing ratio changed little for the remaining dates in the period (Fig. 3.3). Moistening in the second recovery period corresponded to a period of intense moisture advection, with values of $\sim$0.3 g kg h^{-1}, peaking from 0000-1200 UTC on 8 June. Negative moisture advection with magnitudes of -0.5 g kg h^{-1} was occurring from 0000-1200 UTC on 10 June at heights of 1.5-2.5 km (Fig. 3.3). The height and timing of negative moisture advection on 10 June suggest advection of drier air from the west is impacting ARM sites, advection of PBL characteristics from the west has been associated with heterogeneous NLLJs (Gebauer et al. 2018; Smith et al. 2019), therefore examining NLLJ evolution on this date may provide insight into heterogeneous NLLJs.

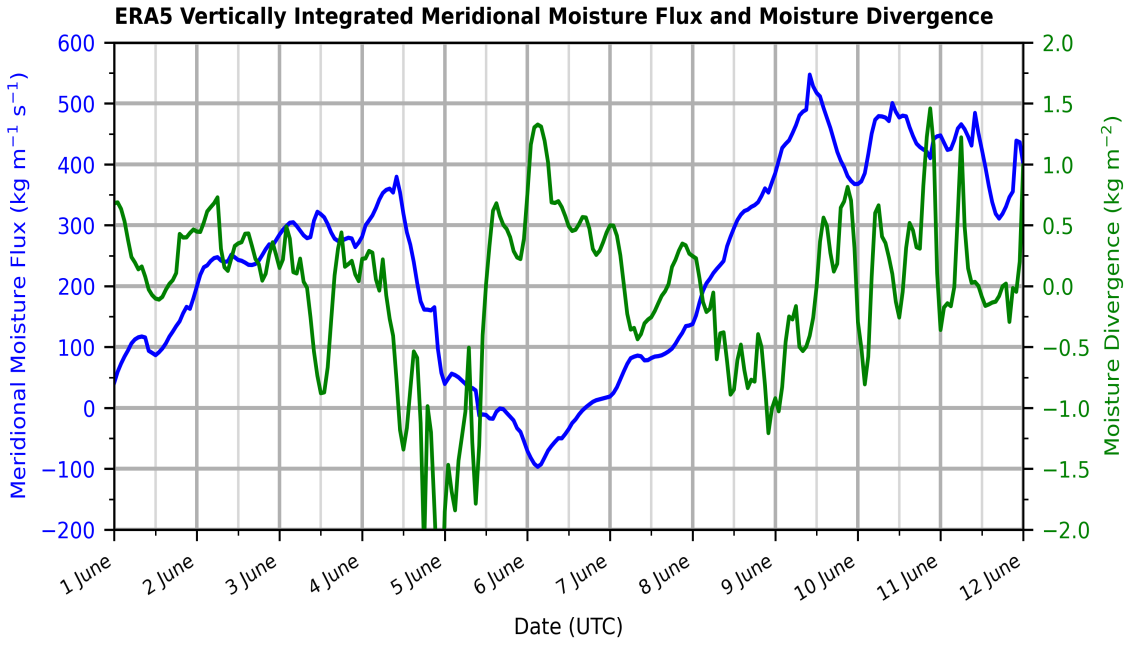

Figure 3.2: Vertically integrated meridional moisture flux (blue line) and vertically integrated moisture flux, spatially averaged over the ARM domain using hourly ERA5 data from 6 June to 12 June 2002. With the western and eastern bounds using longitudes from the western and eastern ARM sites and the northern and southern bounds using latitudes from the northern and southern ARM sites.

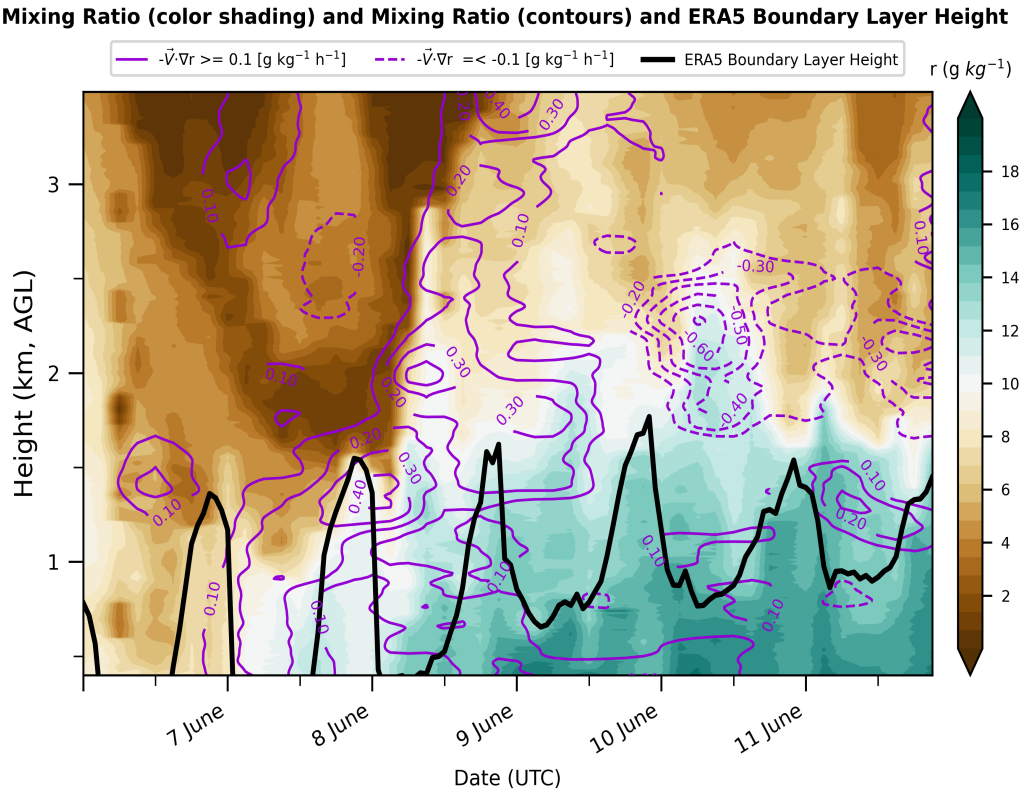

Figure 3.3: A time series from 6-12 June 2002 valid at the central ARM site (Lamont), showing mixing ratio (shaded) and moisture advection (purple contours) from rawinsonde data, with PBL height from ERA5 data as indicated by the solid black line.

3.1.2 Intensification of the NLLJ

Utilizing the criteria of Bonner (1968), the peak southerly flow at Lamont began at or below category 1 (wind speed equal or exceeding 12 m s^{-1}) following both frontal passages and subsequently rose to category 3 (equal or exceeding 20 m s^{-1}) 2 to 3 days later (Fig. 3.4). This systematic change is further explored by examining the magnitude and height of the peak v-wind components in the NLLJ at the five rawinsonde sites during the night (0600-1200 UTC/0000-0600 CST) (Fig. 3.5).

A dramatic increase in the strength of the southerly flow following the frontal passage occurs at all five sites (Fig. 3.5a). The wind maximum at most sites began at less than 10 m s^{-1} following the reestablishment of the southerly flow and then reached between 20 - 25 m s^{-1} later in the period. The height of the maximum in the southerly winds also evolved following the passage of the cold fronts. Following the first front, the height of the southerly maximum increased from $\backsim$200-400 m above ground level AGL[1] on 30 May to heights of 600 to 700 m on 4 June (Fig. 3.5c). This increase in height was also evident in the second period, albeit less dramatic and with greater variations with time and between stations (Fig. 3.5c). The elevated peak southerly winds at Morris and Purcell (above 1.4 km) just after the second frontal passage were likely associated with the lifting of the pre-frontal southerly flow over the cold front. Otherwise, the height of the southerly winds at the other three sites increased from below 500 m to heights between $\backsim$625 to 750 m during this second period. The range of heights of the maximum southerly winds is within the findings of past studies such as Whiteman et al. (1997). However, these results clearly suggest that the evolution of the structure of the NLLJ may vary systematically within a synoptic framework even during the warm season.

As expected for consideration of the IO mechanism, the southerly NLLJ also has a supergeostrophic component (Fig. 3.6a). The magnitude of the supergeostrophic enhancement varies from night-to-night with the strongest ageostrophic enhancement of $\backsim$7 m s^{-1}

[1] Above ground level (AGL) will be used for all heights unless otherwise noted

on 1 June following the first frontal passage and again on 11 June during the second recovery period. While there is an ageostrophic enhancement, the data in Fig. 3.6 shows that the increase in the maximum southerly wind is driven largely by the increase in geostrophic component with time. This result again suggests the importance of the synoptic framework.

As occurred for the southerly NLLJ, the height of the maximum westerly winds also increased during the 1^{st} recovery period. The height of the westerly NLLJ for this 1^{st} recovery period was generally located above the southerly NLLJ especially later in the period where the westerlies were generally located between 1 and 1.5 km. During the 2^{nd} period, however, the height of the westerly NLLJ showed more variations between the sites especially earlier in the period, perhaps consistent with a more synoptically disturbed flow. The intensity of the westerly NLLJ exhibited a similar day-to-day pattern of as that observed in the southerly NLLJ (Fig. 3.5b). Westerly NLLJ speeds increased from 2.5-7.5 m s^{-1} on 30 May to 10-18 m s^{-1} on 3 June, and followed a similar evolution in the second recovery period (Fig. 3.5b). The spatial variations in the intensity of the westerly NLLJ was again similar to the southerly NLLJ, with greater intensity tending to occur at Vici, Hillsboro and Lamont (Fig. 3.5b). In contrast to the southerly NLLJ, the height of the westerly NLLJ did not exhibit a pronounced temporal trend, however, on 10 and 11 June heights do appear to be converging at 1500-2000 m at all sites except Vici. These variations in the westerly NLLJ between the two recovery periods are consistent with findings by Walters and Winkler (2001) which suggest that synoptic flow impacts characteristics of westerly NLLJs. Additionally, analytical work by Shapiro et al. (2016) suggests that sub-synoptic scale processes may influence characteristics of the westerly NLLJ.

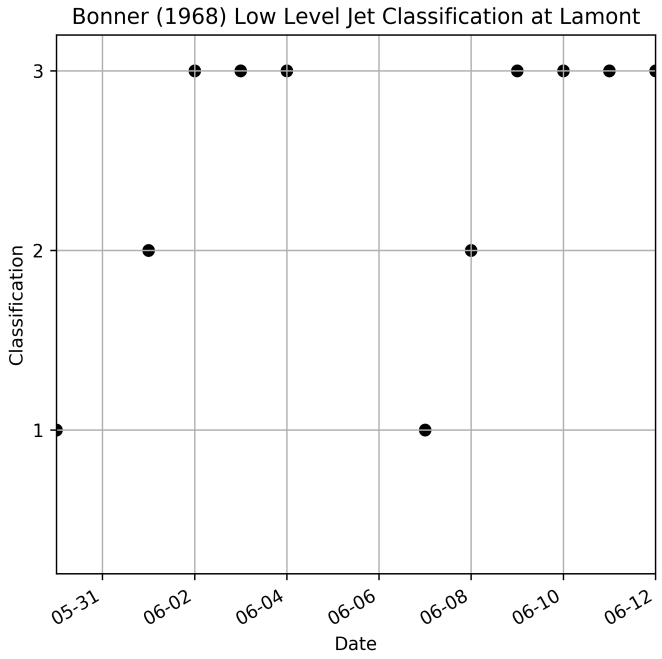

Figure 3.4: Classification of the strength in the southerly component of the NLLJ below 3 km in height utilizing the criterion of Bonner (1968). For the category 1, the wind speed must equal or exceed 12 m $^{-1}$ with vertical shear of 6 m $^{-1}$ or more above and below the height of the maximum. For category 2, the wind speed must equal or exceed 16 m $^{-1}$ with 6 m $^{-1}$ of vertical shear, while for the 3rd category, the peak must equal or exceed 20 m $^{-1}$ and the minimum winds above and below the southerly maximum must decrease by at least 10 m $^{-1}$.

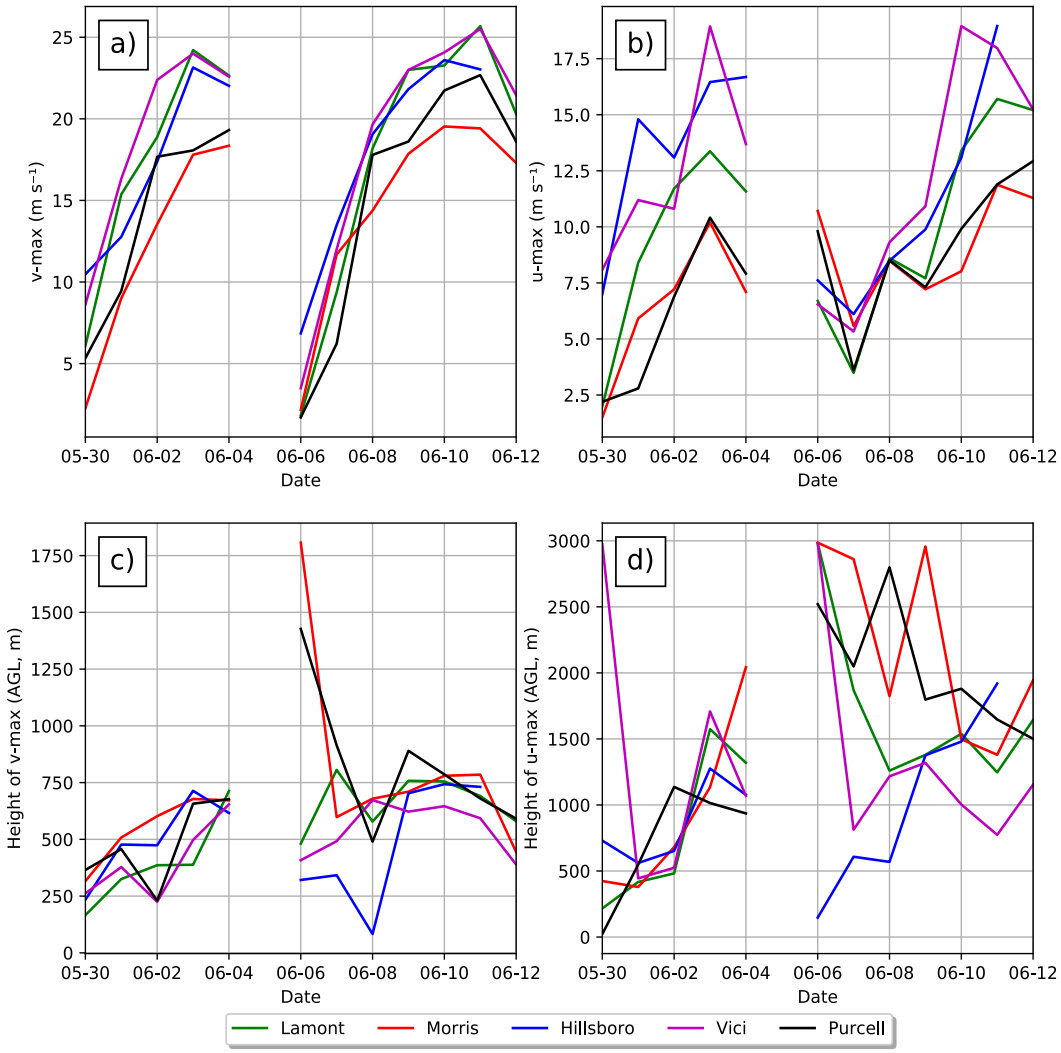

Figure 3.5: Peak NLLJ u and v component wind speeds during the interval 0300-1200 UTC for each day from 30 May-12 June 2002. a) Magnitude of v_{max}. b) Magnitude of u-max. c) Height of the v_{max}. d) Height of the u-max. Heights are above ground level (AGL) for each site.

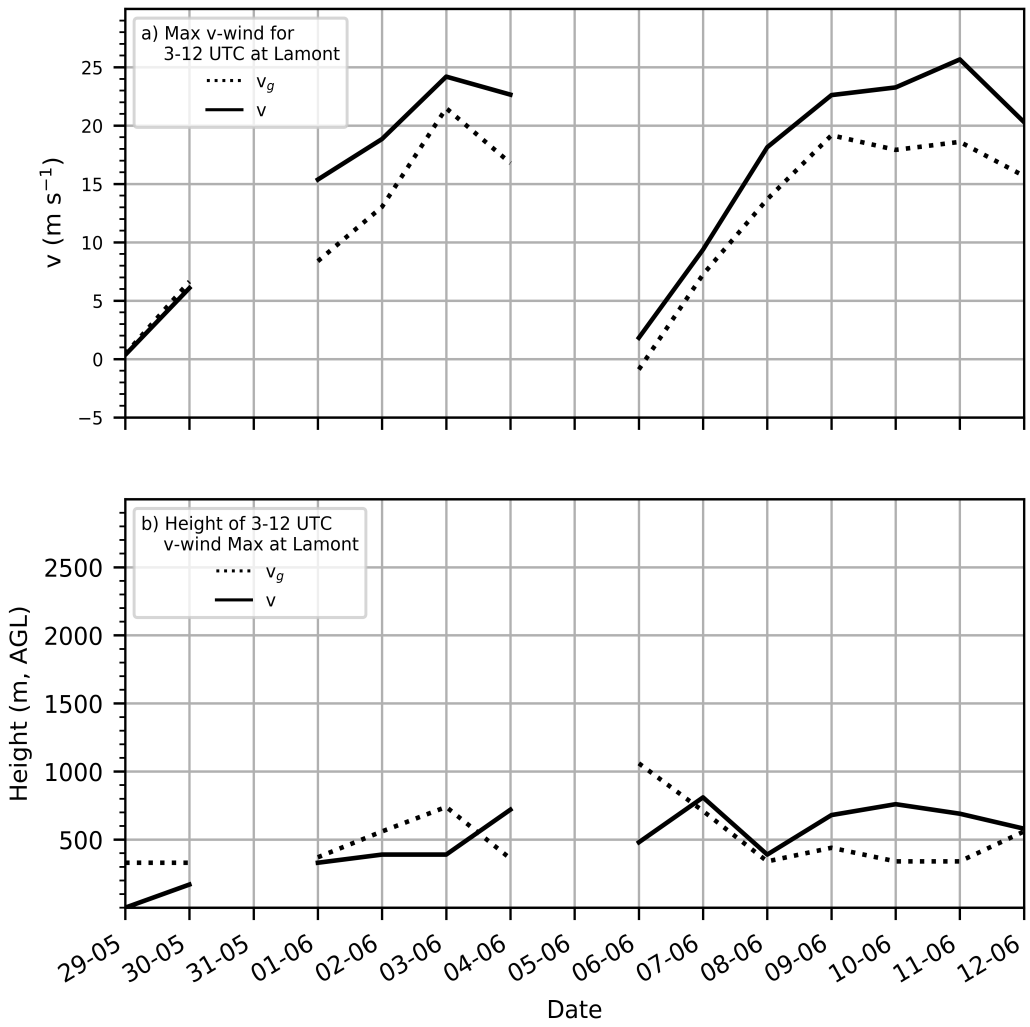

Figure 3.6: The maximum southerly component of the wind (solid line) and of the geostrophic wind from the same time (dotted line) during the overnight hours (0300 to 1200 UTC) from radiosondes launched from the central facility at Lamont during the two recovery periods. Note the sloping terrain and the use of constant pressure surfaces precluded the estimation of a geostrophic wind below 350 m. a) Maximum winds. b) Height of the maximum wind.

3.2 Overview of Low-level Jet Evolution

As noted earlier, the diurnal variations below 3 km in the westerlies were primarily ageostrophic in nature. For example, on 8 June from 0900-1200 UTC an ageostrophic enhancement of $\sim$4 m s^{-1} took place at heights near 1.5 km (Fig. 3.7a). A westerly NLLJ located at 500-1500 m first appeared on 8 June and returned the following nights in the recovery period. The westerly NLLJ was primarily ageostrophic in nature with an enhancement of 2-6 $^{-1}$ on 8, 10 and 11 June. During the daytime hours on these dates, u had an easterly ageostrophic component of of 0-5 m s^{-1} within the moist boundary layer, this is consistent with upslope flow associated with daytime heating along the slope.

As noted earlier, the ageostrophic enhancement to the v_g is relatively small when compared to the increases in v_g that took place during the two recovery periods (Fig. 3.6a). Specifically, during the first period, the 0000 UTC southerly wind increased by 11 m s^{-1} (from 6 to over 17 m s^{-1}), while the maximum southerly geostrophic winds observed during the night increased by $\backsim$13 m s^{-1} (from $\backsim$6 to 19 m s^{-1}). During the second recovery period, the southerly nocturnal geostrophic flow grew by 22 m $^{-1}$ (from nearly 3 m s^{-1} to $>$25 m s^{-1} for times between 0300 and 1200 UTC), while the daytime (0000 UTC) southerly wind increased by 21 m s^{-1} (from -3 to nearly 18 m s^{-1}). These large increases relative to the smaller ageostrophic enhancements seem to suggest the 1st order importance of the general increase in the strength of the daytime southerly winds and southerly geostrophic wind in controlling the magnitude of the southerly NLLJ. Thus, the increases in southerly geostrophic flow and the smaller ageostrophic enhancement combine to produce the strong southerly NLLJ.

During both recovery periods, the observed daytime (i.e., 1200-0000 UTC) southerly flow and the nocturnal southerly geostrophic wind exert a strong control on the southerly NLLJ (Fig. 3.6a). These findings are consistent with the results of Parish (2016) which document the intensity of the background southerly geostrophic wind due to an east-west horizontal pressure gradient driven by seasonal heating exerting a strong influence on the

magnitude of the southerly NLLJ. That investigation utilized data for the months of June and July over a five year period (2008 to 2012) from the North American Mesoscale Forecast System. Our results suggest that the changes in the geostrophic wind response happens on synoptic time-scales.

A period of most rapid intensification of low-level v_g began at 1200 UTC on 7 June and continued until 8 June at 1200 UTC. Over this time, v_g increased up to 10 m s^{-1} at heights below 2 km. The daytime intensification of v_g is consistent with the results of Parish (2016) which suggest the intensity of the background southerly geostrophic wind due to an east-west horizontal pressure gradient driven by heating exerts a strong control on the magnitude of the southerly NLLJ.

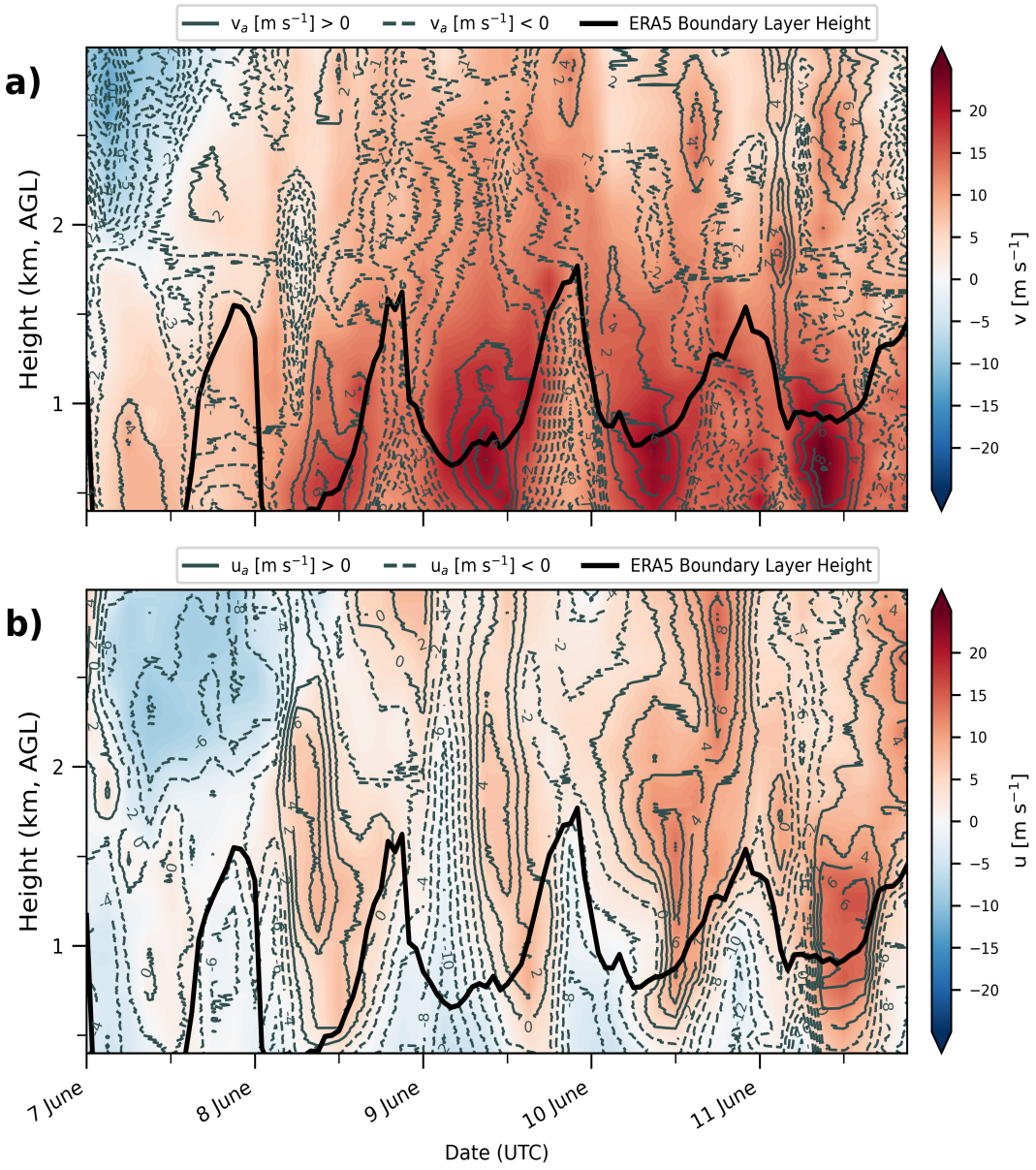

Figure 3.7: Time series during 6 June to 13 June 2002 from rawinsonde observations at Lamont showing the full wind component (color fill) and ageostrophic component (contours) of the a) meridional wind and b) the zonal wind. ERA5 PBL height at Lamont is shown as the solid black line.

3.3 Investigating the Role of Thermal Gradients

Gebauer and Shapiro (2019) argued that the strongest v_g would be found near the ground around sunset based on finding a mean negative along-slope surface buoyancy gradient (warmer temperatures to the west) in the late afternoon from their examination of 19 years of surface data from the Oklahoma Mesonet. Their study proposed that the along-slope gradient in buoyancy at the surface had the same magnitude of baroclinic impact on the NLLJ as the Holton (1967) mechanism that assumed constant buoyancy along the slope.

Our use of sounding data also allows us to move beyond horizontal gradients of θ_v at the surface and examine their vertical structure. We find that a diurnally reversal in the buoyancy gradient occurs, but with a complex vertical structure (Fig. 3.8). Higher values of θ_v to the west are indeed generated over the depth of the daytime boundary layer in association with solar heating, while during the night the thermal gradient decreases and even reverses with warmer temperatures to the east (Fig. 3.8). However, the height of this reversed gradient depends on the depth and characteristics of the night-time and morning boundary layer. Warmer temperatures to the east were found near the surface at 0900 and 1200 UTC on 7 June when a strong and shallow surface inversion was present over Lamont (Fig. 3.8) and a constant height surface in the warm air just above the strong surface inversion at the central site intersects the cooler air below the strong, shallow inversion at Vici, upslope to the west.

The low-level θ_v gradient reversal was correlated with the height of the v_{max} (Fig. 3.8a). After 7 June, the reversal in the gradient extended over deeper layers and became concentrated aloft. The vertical profiles of the θ_v gradient between the western and central sites for 10 June from 0900 to 1200 UTC are shown in Figure 3.8. The gradient in θ_v near the surface has warmer temperatures to the west with this buoyancy difference decreasing during the night from 0900 to 1200 UTC and then increasing at 1500 UTC. Interestingly, enhanced westerlies coincided with the θ_v gradient at 1500 UTC, suggesting that this may be more than an artifact of differences in the morning transition of the boundary layer.

Examining changes to surface radiation balance along the slope can help in understanding if radiative effects contributing to the θ_v gradient reversal. As noted in the methods section, during IHOP radiation data were collected from SIRS sites. This data indicates that on 8 June, the central site had little change in upwelling longwave radiation (UWLR) compared to sites located further upslope (Fig. 3.9a). Instead the gradient was associated with increases in downwelling longwave radiation (DWLR) (Fig. 3.9b). As noted earlier, moistening was occurring over the ARM sites on 8 June, this may offer an explanation for some variations in DWLR that occurred at this time. On 10 June, the SIRS site located in northwestern Kansas exhibited a similar evolution in UWLR and DWLR as the central site on 8 June (Fig. 3.10). This behaviour may help explain why the low-level θ_v gradient reversal became more elevated on later dates, less surface cooling as moisture advanced further upslope on later dates.

Hence, the gradients in θ_v are linked to variations in the depth and characteristics of the boundary layer over the slope along constant height surfaces rather than the surface properties on the slope alone. This situation means that, through the thermal wind relationship, a surface maximum in v_g no longer occurs at night as previously proposed consistent with earlier findings (e.g., Fig.3.6) that indicate the maximum southerly geostrophic wind occurs aloft near the height of the peak nocturnal southerly wind. In addition, these subtle differences in the horizontal gradients in θ_v aloft may help explain the variations in the height and timing of the maximum v considering that the maximum v occurred on various nights from 0600 to 1200 UTC (Fig. 3.8a).

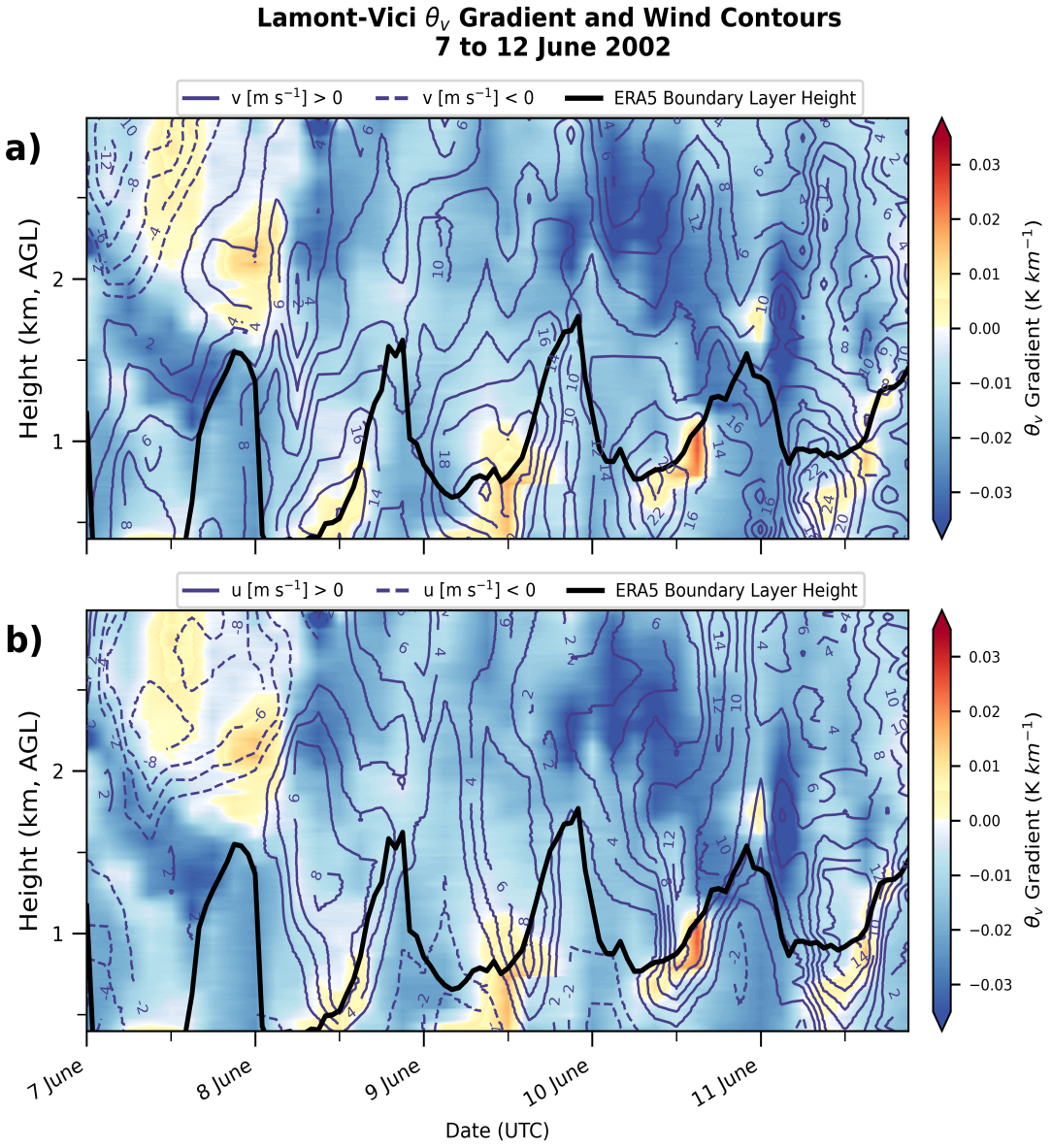

Figure 3.8: Time series from 7-11 June 2002 of the θ_v gradient between the central and western ARM sites. calculated from sounding data between the western and central ARM sites, with a) zonal wind and b) meridional wind components from Lamont.

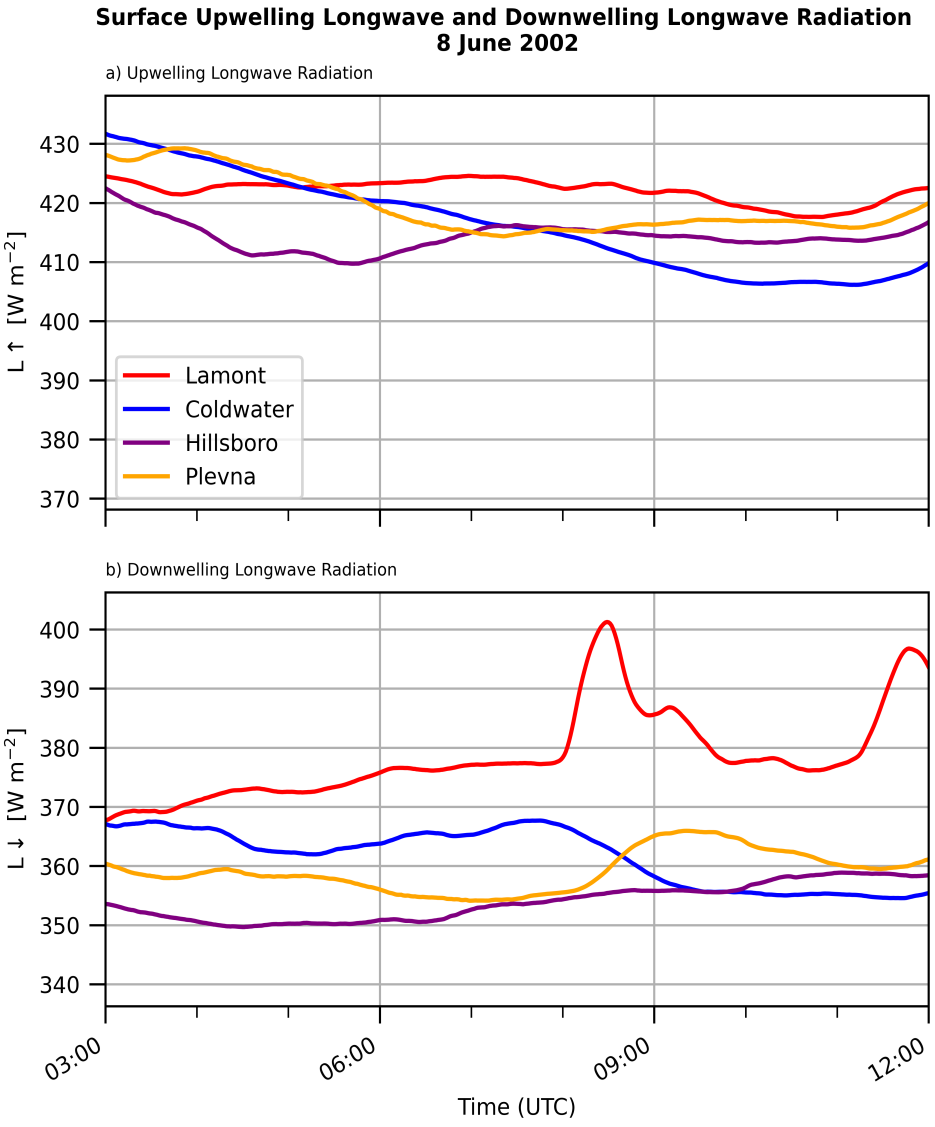

Figure 3.9: a) Upwelling longwave radiation and b) downwelling longwave radiation measurements from Radiation ARM Solar-Infrared Radiation System (SIRS) sites in the overnight hours on 8 June 2002.

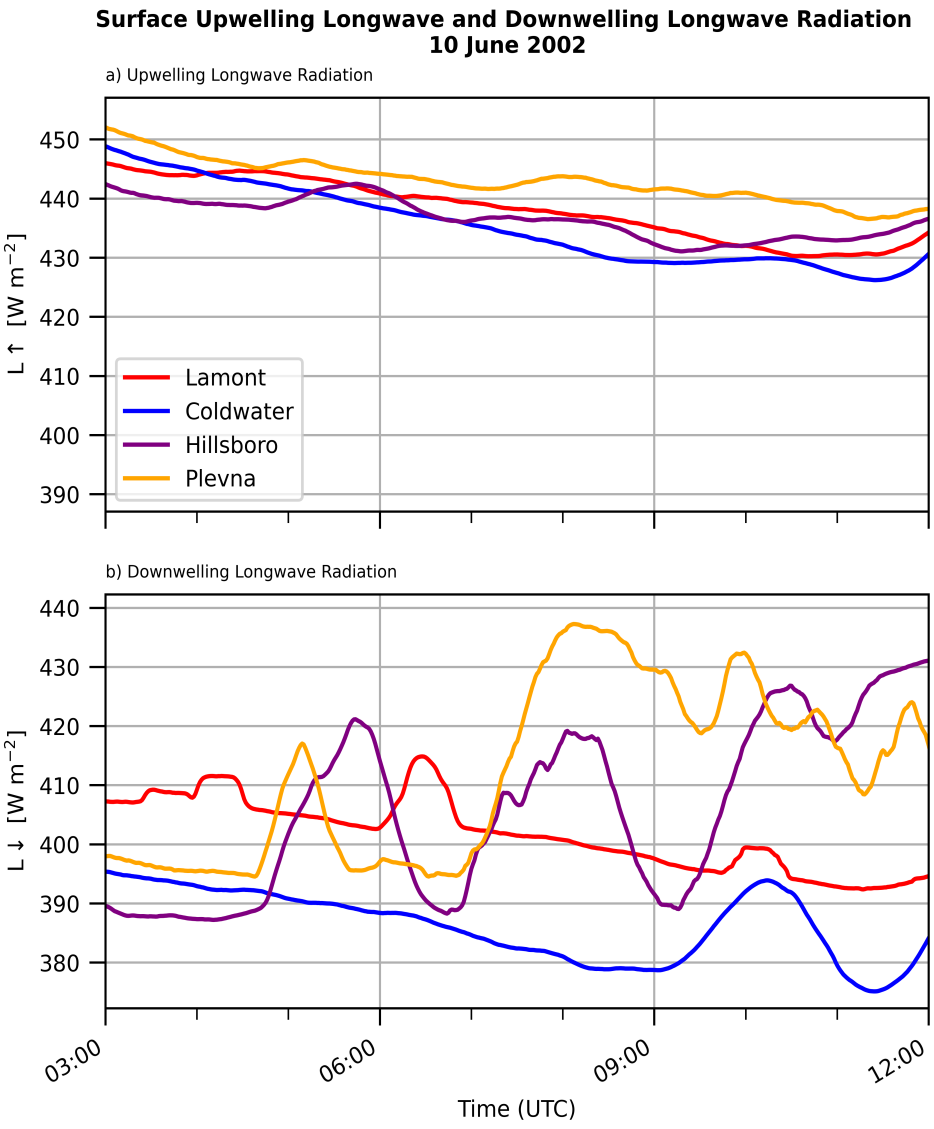

Figure 3.10: As in 3.9 except for 10 June 2002.

3.4 Summary

These findings suggest that characteristics of the NLLJ follow a post-frontal synoptic framework, where NLLJ magnitudes increase and heights lower for the southerly wind-maximum and converge at 1000-2000 m for the westerly wind-maximum. The increase in the southerly NLLJ is largely due to an increase in the geostrophic flow with a nighthly ageostrophic enhancement. This evolution of the NLLJ also coincides with an intensification of ageostrophic upslope flow, indicative of thermal gradients returning to the slope. As was discussed in the introduction, thermal gradients along the slope can create a complex environment with multiple mechanisms that can facilitate NLLJs. The westerly NLLJ may exhibit a less obvious trend due to being more susceptible to influence by an increasing synoptic background flow as well as sub-synoptic scale processes with thermal gradients returning to the to the region after a frontal passage. The following 3 chapters will provide a better understanding of the day-to-day evolution of the NLLJ. The subsequent analyses in these chapters includes the use of data from the ERA5 data set, which allows for a more in-depth look at the gradients along the slope than is provided by the ARM soundings.

Chapter 4

Pre-Moistening Phase

After examining spatial and temporal variations during the recovery periods, a case study format is used to examine NLLJ evolution during the pre-moistening phase corresponding to 7 June 2002. The focus of this chapter is documenting the evolution of the NLLJ that occurred on this date to better understand its mechanisms and characteristics before thermal gradients and active synoptic conditions return to the region. To investigate the mechanisms driving this evolution, we begin by describing the synoptic conditions on 7 June.

4.1 Synoptic Conditions

On 7 June at 0000 UTC, mid-level flow (500 hPa) was located to the north with a zonal jet-streak over North Dakota and Montana with wind speeds diminishing to the south (Fig. 4.1). 500 hPa height contours suggest an anticyclonic curvature to upper-level flow with winds out of the northwest at the ARM sites. This relative location of the ARM sites to the mid-level jet streak is not favorable for development of upper-level coupled low-level jets, since the sites are located nearest to the front right quadrant (also called right exit region) of the jet-streak. Walters (2001) considered this type of large-scale pattern as quiescent. Their study found composites of low-level jets occurring in this environment tending to have an area of high pressure to the southeast, which is consistent with MSLP contours that indicate an area of low pressure was confined to western Nebraska stretching south to northwest New Mexico (Fig. 4.2).

Quiescent synoptic-scale conditions are also reflected in surface analysis which suggest thermal gradients along the slope being the primary driver of surface winds over the Southern Plains in the late afternoon (2100 UTC 6 June) (Fig. 4.2). The surface θ_v gradient was oriented southwest to northeast, from the Texas Panhandle to central Nebraska

where θ_v increased in the upslope direction by 10-15 K over a distance of $\sim$200 km (Fig 4.2a). Effects of heating along the sloping terrain to lower tropospheric winds have been noted in previous studies and linked to dryline formation (Ogura and Chen 1977; Benjamin 1986; Sun and Wu 1992; Ziegler and Hane 1993; Bluestein and Crawford 1997; Crawford and Bluestein 1997; Peckham and Wicker 2000; Parsons et al. 2000). Simulations by Sun and Wu (1992) found that a weak low-level easterly component along the slope that was induced by differential heating was important for driving moisture gradients and dryline formation.

Low-level winds occurring along the θ_v gradient appear to be contributing to a moisture gradient in western Kansas and the Texas Panhandle (Fig. 4.2). This moisture gradient is evident in the analysis of mixing ratio contours, with the 8 g kg^{-1} contour located along the Kansas and New Mexico border, and the 12 g kg^{-1} contour near the Oklahoma border of the Texas Panhandle (Fig. 4.2). Gradients in surface θ_v and moisture suggest heterogeneous PBL characteristics are located at $\sim$99-101°W, this is reflected in PBL heights from ERA5 data (Fig. 4.3). The PBL heights are located on the western edge of the thermal gradients where heights are $>$2500 m, except over southeastern Colorado where a local minimum with values of 1500-2000 m is located.

Spatial variations in PBL characteristics suggest that ARM sites are located to the south-east of the most favorable location for development of southerly NLLJs by boundary layer mechanisms. With the most intense surface θ_v gradient located in western Kansas and central Nebraska, this is a preferred location of southerly NLLJs developing by several mechanisms: IO, thermal wind reversal and differential heating along the slope. These environmental conditions may explain why the central site had a Bonner category 1 NLLJ develop this night.

The boundary layer conditions across the ARM domain at 2100 UTC on 6 June (Figs. 4.2 and 4.3) included light winds at the surface and weak gradients in both θ_v and boundary layer heights on the slope. These conditions are consistent with the observations of a weak

Bonner category 1 NLLJ over the central site as mechanisms of the IO operating on a strong background v_g, gradients in differential heating along the slope, and reversals of the thermal wind are relatively weak and unlikely to produce a strong NLLJ. Stronger southerly flow and more significant gradients in θ_v at the surface and in boundary layer heights, however, were found in the western Oklahoma Panhandle, western Kansas, and central Nebraska (Figs. 4.2 and 4.3). A stronger NLLJ is more likely to occur over these regions, although western Nebraska is impacted by a synoptic disturbance with westerly winds.

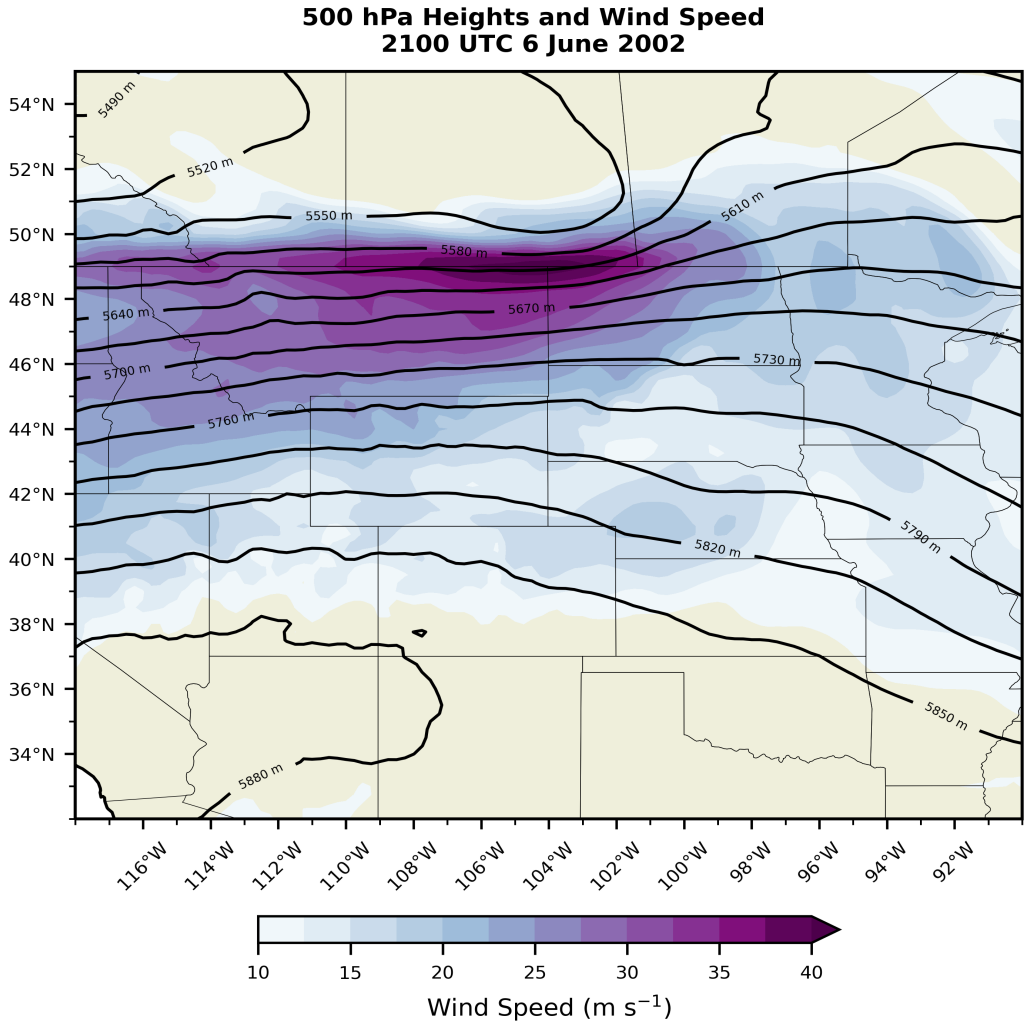

Figure 4.1: ERA5 reanalysis 500 hPa geopotential height contours and wind speed over the central United States for 2100 UTC 6 June 2002.

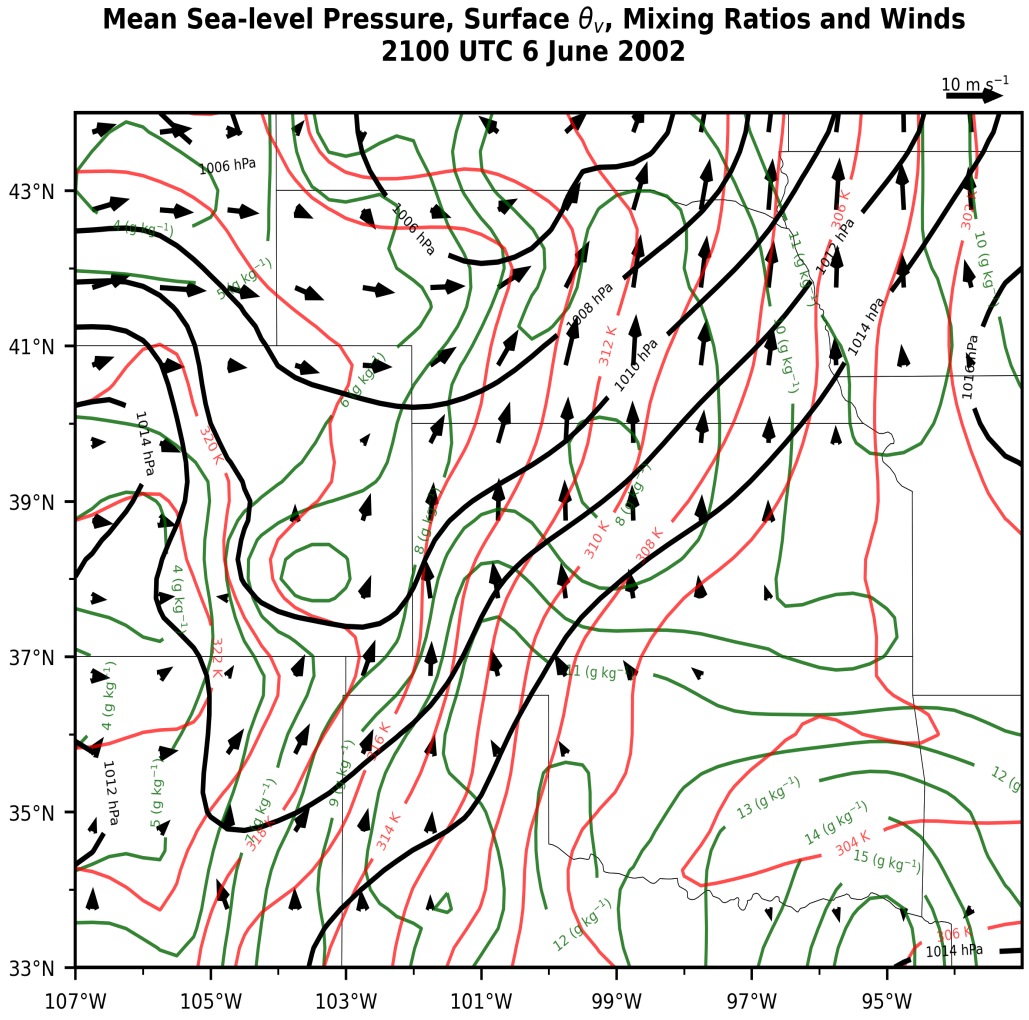

Figure 4.2: Surface mean sea level pressure contours (black with 2 hPa increments), θ_v contours (red with 2 K increments), mixing ratio contours (green with 1 g kg^{-1} increments) and surface winds vector data from the ERA5 Reanalysis over the Southern Plains at 2100 UTC 6 June.

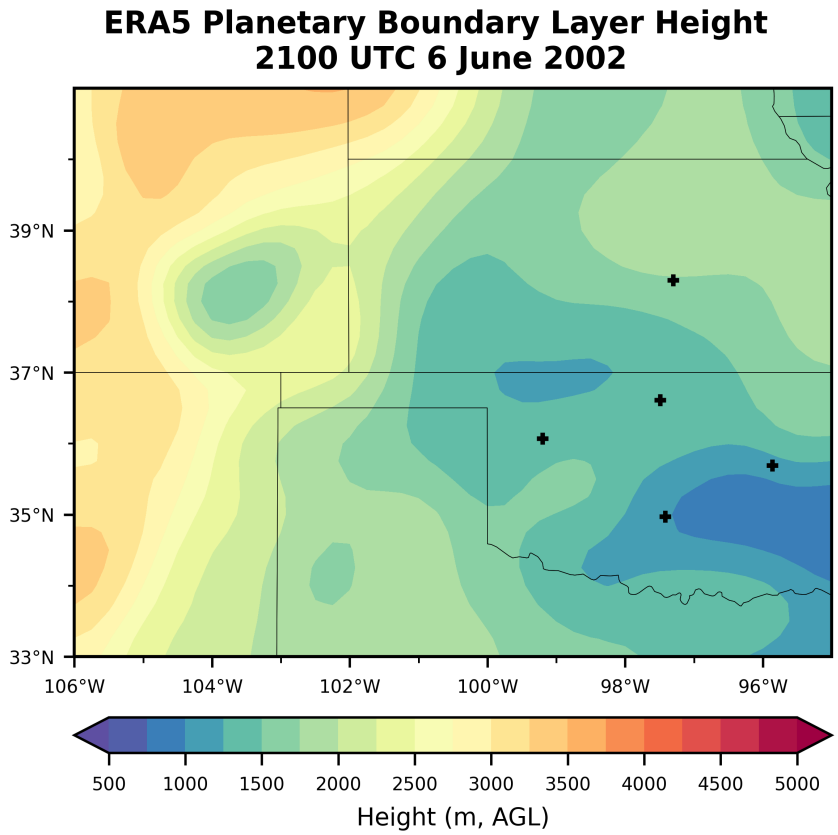

Figure 4.3: Planetary boundary layer heights from ERA5 data over the Southern Great Plains at 2100 UTC on 6 June 2002. The location of the 5 ARM sites are indicated by black crosses.

4.2 NLLJ Evolution

This section describes the the southerly and westerly NLLJ that occurred on 7 June over the SGP and factors from the previous section that may have influenced evolution of the low-level winds.

4.2.1 Evolution of the Low-Level Southerly Flow

Wind vectors, speed at the height of the v_{max} at heights below 2 km were constructed using ERA5 reanalysis data to help determine spatial characteristics of the southerly NLLJ (Figure 4.4). Figure 4.4 suggests that peak intensity of the southerly NLLJ occurred at 0600 UTC, at this time the most intense low-level (below heights of 2 km) southerly flow was located in southeastern Colorado and western Kansas with speeds of $\sim$20 m s^{-1} at heights of 400-600 m (this area is hereafter referred to as the jet core). Wind vectors at the height of the v_{max} became more westerly with time, going from southeasterly at 0300 UTC (Fig. 4.4a) to southwesterly from 0600-1200 UTC (Fig. 4.4b,c,d). This veering with time resulted in the southerly NLLJ exhibiting an anticyclonic spatial pattern at the time of peak intensity. This veering with time of the v_{max} along with the southwest-northeast orientation of the jet core resembles the anticyclonic southwest-northeast (Ac-SWNE) low-level jet type described by Walters and Winkler (2001). Further analysis of the composites by Walters (2001) found this configuration was associated with queiscent synoptic conditions which is consistent with analysis of synoptic conditions from earlier in this chapter.

Analysis of surface conditions (Fig. 4.2) indicated that the most favorable area for an NLLJ associated with an IO in western Kansas and southeastern Nebraska. The position of the v_{max} at 0300 UTC does agree with this preferred location (Fig. 4.4a). Intensity of the NLLJ also appears to be associated with the PBL heights (Figs. 4.3 and 4.4). This location left the ARM sites on the southeastern periphery of the NLLJ. As was pointed out earlier, a local minimum in PBL heights was located near the same area as the maximum in wind speeds associated with the NLLJ. This finding suggests that heterogeneous PBL characteristics were contributing to NLLJ intensity with a more complex relationship than that proposed by Parish (2016).

Although the ARM sites were on the southern periphery of the NLLJ, meridional cross sections suggest that northward advection of moisture was associated with enhancements

to low-level southerly flow flow. north-south cross sections were constructed over the longitude of the central site (∼97.5°W) utilizing ERA5 data. These cross sections reveal a weak southerly NLLJ (<10 m s^{-1}) was occurring throughout the night south of ∼37°N (Fig. 4.5). Consistent with analysis of the v_{max} a more intense southerly NLLJ was located north of 37°N. Figure 4.5 indicates large variations (5-10 m s^{-1}) in v_g occurred over these latitudes from 0300 UTC to 1200 UTC. These variations in v_g were charactered by a decrease of ∼10 m s^{-1} near 39°W from 0300-0900 UTC followed by an increase of ∼20 m s^{-1} at 1200 UTC. Although an IO would be expected over these times, the variations in v_g make it difficult to determine its contribution, since an ageostrophic enhancement may result from the time it takes for flow to adjust to the changes. he southerly NLLJ developed a greater ageostrophic component beginning at 0900 UTC (Fig. 4.5b). This geostrophic enhancement suggests additional processes besides an IO are influencing NLLJ evolution. This evolution is also consistent with the AC-SWNE low-level jet type described in Walters and Winkler (2001), since it was found that this type tended to have a larger geostrophic component. Regardless of the mechanism, this enhancement to low-level southerly winds was associated with greater moisture advecting north.

Low-level moisture with mixing ratio values of 10-12 g kg^{-1} advected to the north over night (Fig. 4.5). At 0300 UTC, the northern extent of this moisture was located at 36.5°N at heights below 1.5 km MSL (Fig. 4.5a), over the following 6 h these values of mixing ratios advanced north to ∼38°N, and by 1200 UTC this moisture was located throughout the extent of the cross section. A NLLJ of ∼10 m s^{-1} would be needed for moisture to advect north by 1° of latitude (111 km) over a 3 h period. Adding the v_g and v_g arrows in Fig. 4.5b suggests wind speeds of 5-10 m s^{-1} were in place over this area, making it reasonable to conclude the moistening north of 36.5°N was a result of the southerly NLLJ.

The enhanced southerly flow seen in vertical cross sections is evident in the rawinsonde measurements taken at the 5 ARM sites. This southerly enhancement was characterized by a increases of 5 to 10 m s^{-1} for the v component of the wind compared to the late afternoon

(2100-0000 UTC) (Fig. 4.6). Spatial-temporal variations of the southerly NLLJ on 7 June were characterized by a west to east trend in timing of the peak intensity of the v_{max} (Fig. 4.6). For example, at the western site, the southerly NLLJ peaked at 0600 UTC at a height of $\sim$500 m, then decreased by 1-2 m s^{-1} in subsequent hours (Fig. 4.6a), meanwhile at the eastern site a dramatic intensification of the southerly NLLJ occurred from 0600-1200 UTC (Fig. 4.6a).

Intensification of v_{max} from 0900-1200 UTC at the eastern site was associated with moistening where mixing ratios increased by $\sim$4 g kg^{-1} at the same height (Fig. 4.7b). The height of the spike in moisture is consistent with advection by the southerly NLLJ and confirms the poleward transport of moisture depicted in meridional cross sections. In addition, mixing ratios from the southern site indicate low-level moisture was located to the south of the ARM sites (Fig. 5.15d). These findings support past studies that suggest the southerly NLLJ is an important source of moisture transport over the SGP (Helfand and Schubert 1995; Jiang et al. 2007).

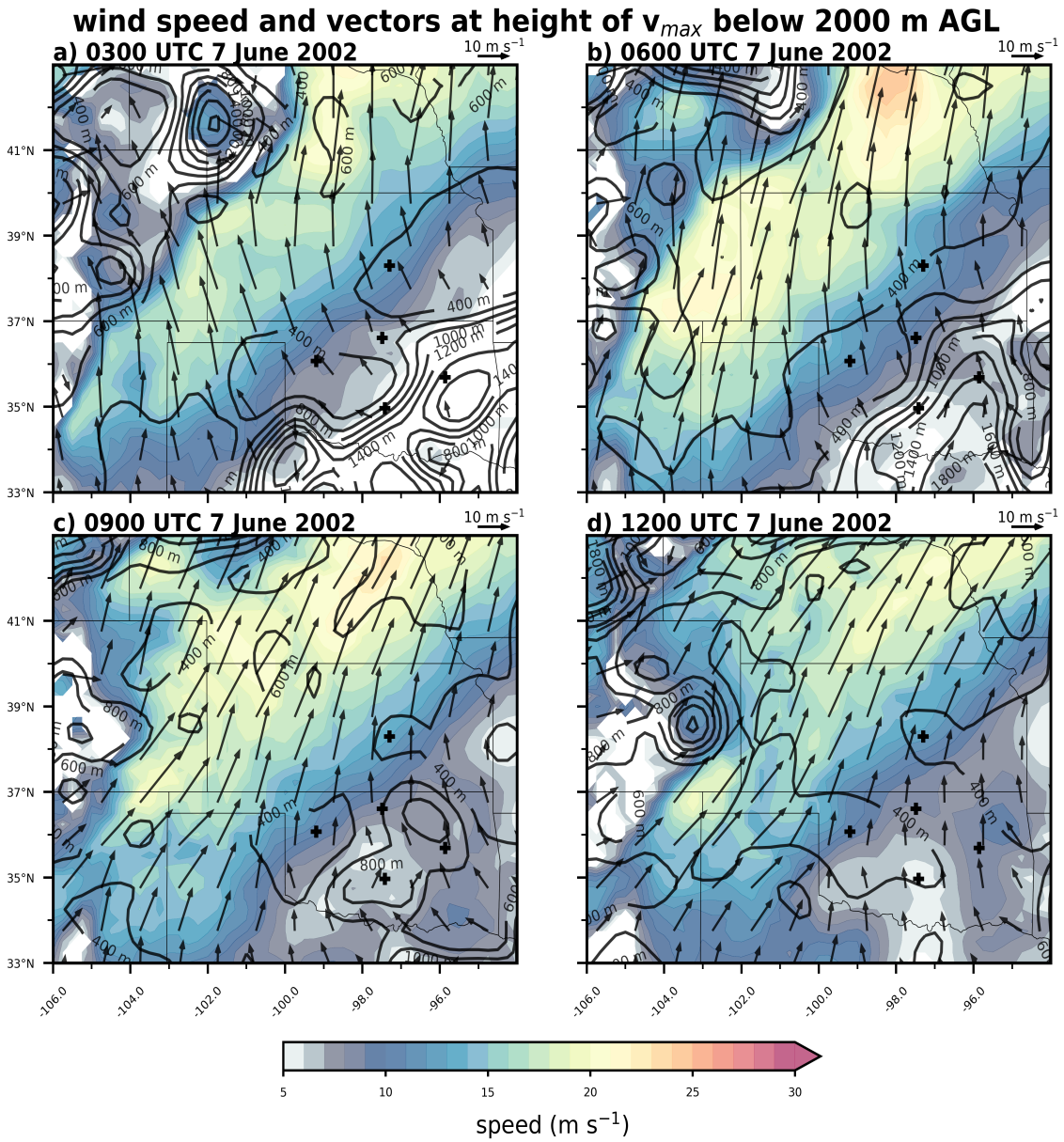

Figure 4.4: Wind speed, height contours (every 200 m, AGL) and vectors taken at the height of the maximum value of $|v|$ (v_{max}) below 2000 m over the Southern Great Plains on 7 June at times: a) 0300 UTC, b) 0600 UTC, c) 0900 UTC and d) 1200 UTC. The location of the 5 ARM sites are indicated by black crosses.

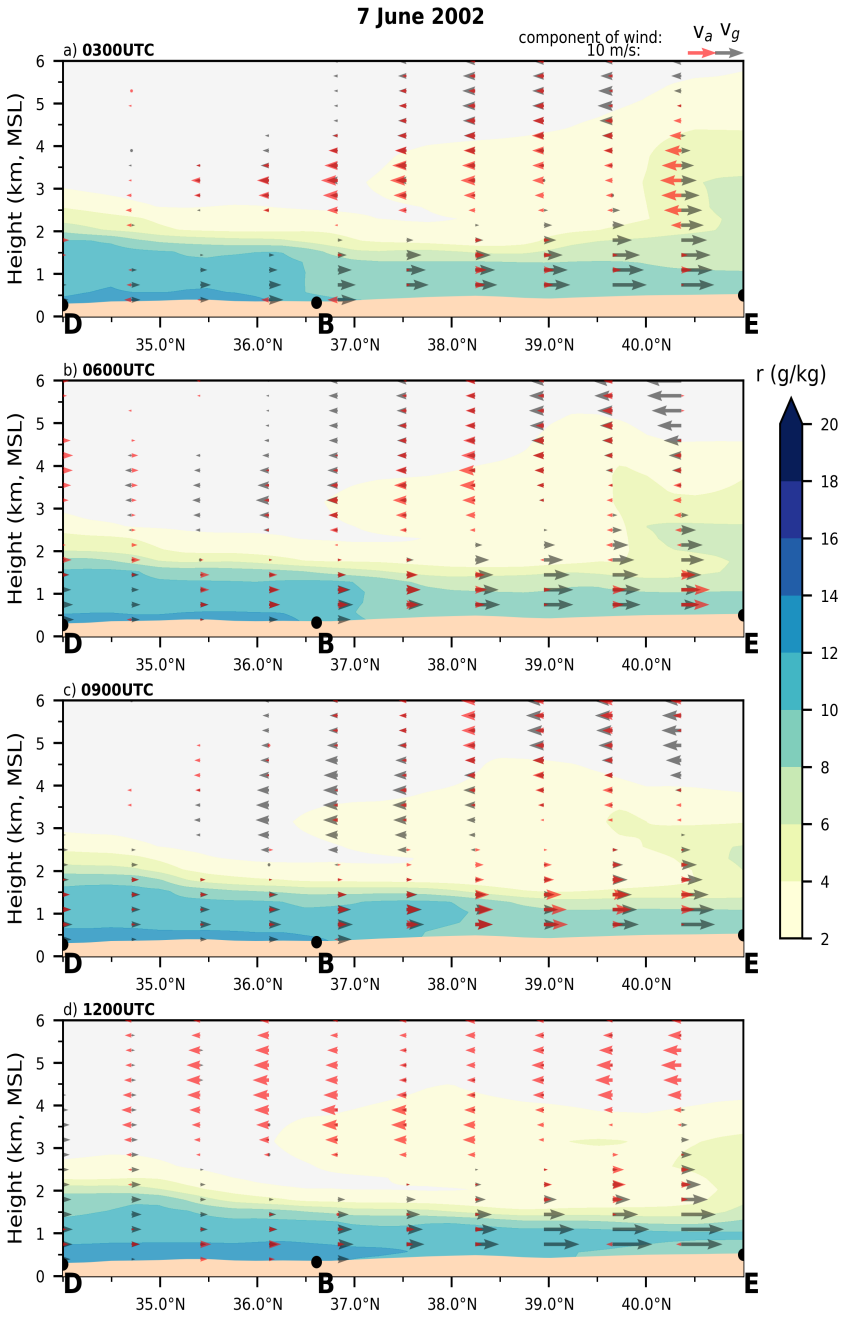

Figure 4.5: 7 June meridional cross section from 34-41°N at 97.5°W corresponding to the longitude of the central ARM site (B). Constructed from ERA5 reanalysis data containing the v_g component of the wind (black arrows), the v_a component of the wind (red arrows) and mixing ratio (color fill). At times: a) 0300 UTC, b) 0600 UTC, c) 0900 UTC and d) 1200 UTC.

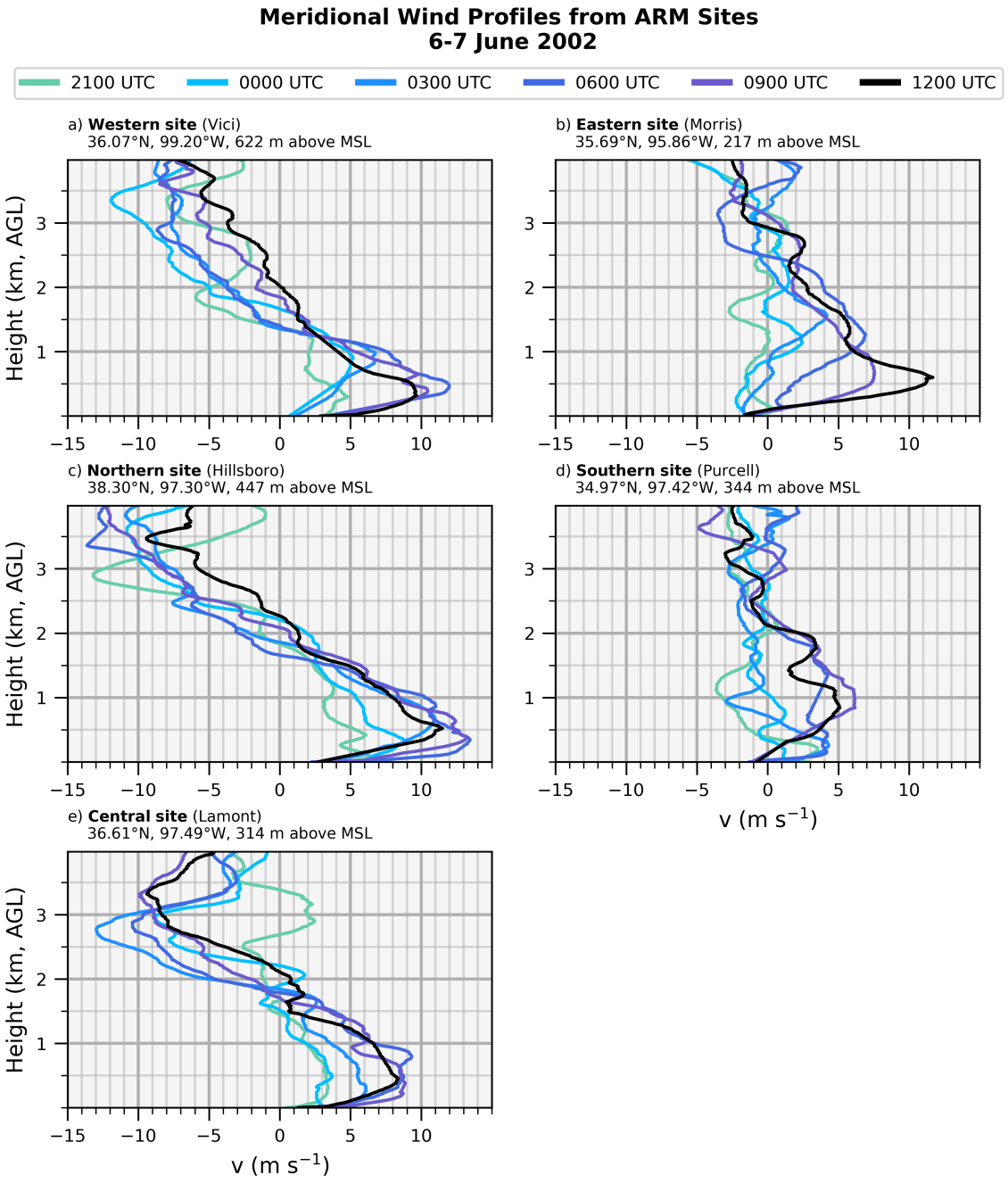

Figure 4.6: Vertical profiles of *v* from 2100-1200 UTC 6-7 June 2002 taken from sounding data collected from the 5 ARM sounding sites: a) western site (Vici), b) eastern site (Morris), c) northern site (Hillsboro), d) southern site (Purcell), and e) central site (Lamont).

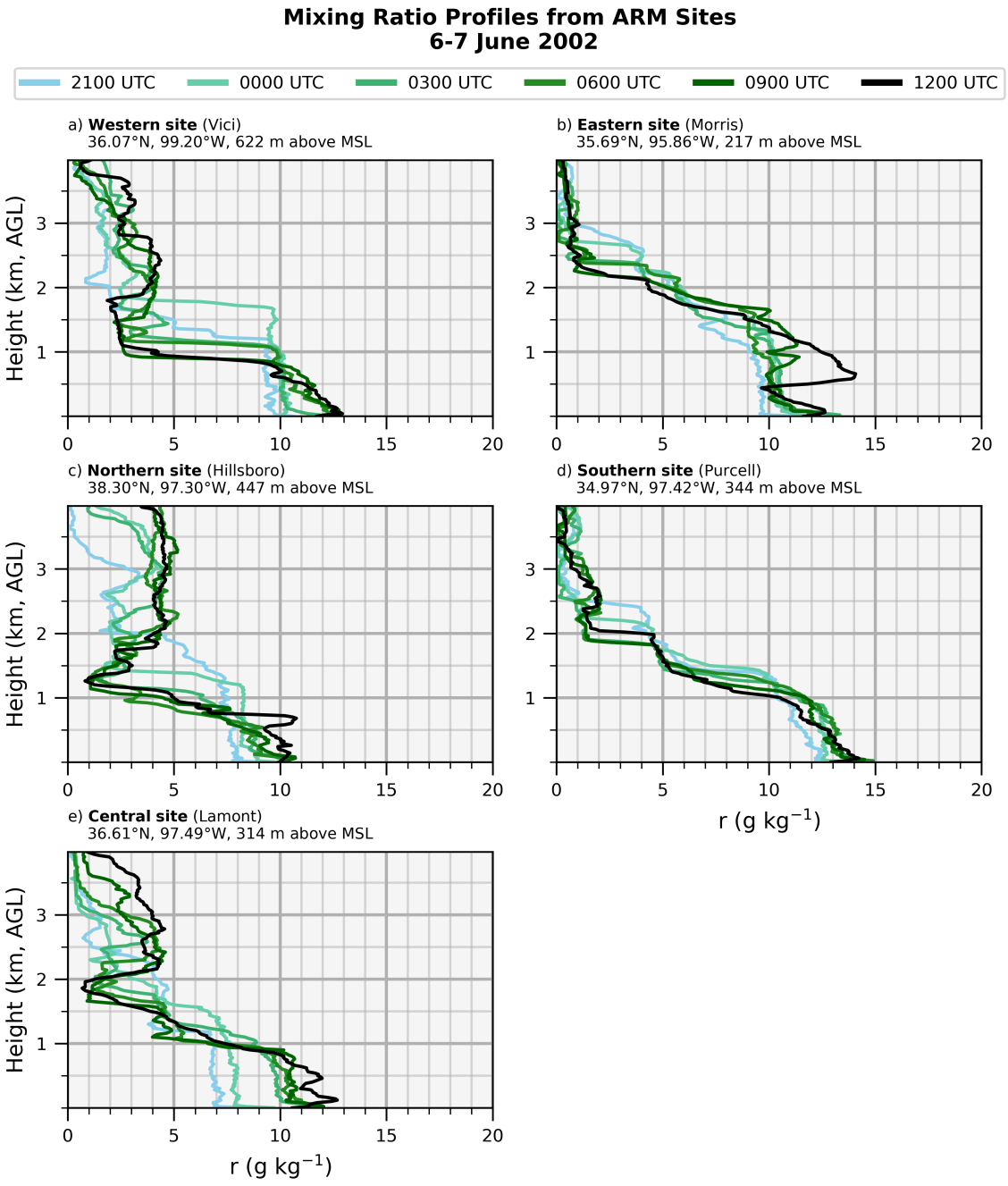

Figure 4.7: Vertical profiles of mixing ratios (mixing ratio) from 2100-1200 UTC 6-7 June 2002 taken from sounding data collected from the 5 ARM sounding sites: a) western site (Vici), b) eastern site (Morris), c) northern site (Hillsboro), d) southern site (Purcell), and e) central site (Lamont).

4.2.2 Evolution of the Low-Level Westerly Flow

As pointed out earlier, the most dramatic changes in low-level southerly flow occurred in the vicinity of a gradient in PBL heights which was located in southeastern Colorado during the late afternoon (2100 UTC). A similar but more pronounced behaviour is seen in the evolution of the low-level zonal winds. At 0300 UTC wind vectors at the height of the u_{max} in the ERA5 reanalysis data have a maximum in their intensity in southeastern Colorado, southwestern Kansas and the Oklahoma Panhandle (Fig. 4.8a). At this time the u_{max} is characterized by speeds of 15-20 m s^{-1} and south easterly in direction at heights of 800-1000 m. A dramatic change occurred 3 h later (Fig. 4.8b). This change was characterized by a shift in direction from southeast to southwest and intensification of $\sim$5 m s^{-1}. An influence of the synoptic feature identified earlier in the synoptic overview likely played a role in these dramatic changes. Impacts of this feature is evident in Fig. 4.8a as a strong gradient in characteristics (height and intensity) of the u_{max} moved north with time with an accompanying northward movement in the strong southwesterly winds. The u_{max} continued to become more westerly and remained about the same intensity but became located over a larger area at 0900 UTC (Fig. 4.8c) followed by weakening and northward shift in the maximum at 1200 UTC (Fig. 4.8d).

Intensification of westerly flow exhibited some heterogeneous characteristics with a slight decrease in intensity at $\sim$100-101°W which was evident at 1200 UTC. Similar heterogeneous features in NLLJs have been observed in the PECAN field campaign (Gebauer et al. 2018; Smith et al. 2019). Gebauer et al. (2018) suggested that heterogeneous NLLJs during PECAN were associated with heterogeneous PBLs with more intense mixing occurring in deeper PBLs to the west resulting in a more intense IO. Smith et al. (2019) suggested something similar, but added the possible role of advection of buoyancy gradients and differential PBL winds.

The ARM sites were located southeast of the westerly low-level wind enhancements except for the northern and western sites (Fig. 4.8). Vertical profiles of u from the ARM

soundings are consistent with nocturnal low-level westerly enhancements to being confined to the northwest portion of the ARM domain (Fig. 4.9). At the western and northern site a westerly wind maximum developed below 1 km from 0900-1200 UTC (Fig. 4.9a,c) with winds at these heights being easterly prior to 0900 UTC and becoming westerly by 1200 UTC. While less obvious at sites to the southeast, there were some hints of a westerly intensification at these locations (Fig. 4.9b,d). Near heights of 1 km, the southern and eastern sites the u component of the wind went from $\sim$-5 m s^{-1} to 0-3 m s^{-1}. This intensification may have been associated with the u_{max} found in the Shapiro et al. (2016) analytical model since a thermal wind reversal was likely occurring at the eastern site with possibly a weak IO. One similar aspect of evolution of the westerlies at the ARM sites to those found in the analytical model is the lowering of the u_{max} with time. Westerly enhancements to the east may have been made less obvious by the easterly acceleration occurring at earlier hours (Fig. 4.9a,c). For example, at the central site easterly enhancements of $\sim$10 m s^{-1} occur at heights of 2-3 km from 0000-0300 UTC (Fig. 4.9e), and at the eastern and southern sites an easterly component intensifies near the surface by $\sim$5 m s^{-1} from 0000-1200 UTC.

The easterly low-level wind enhancements contributing to NLLJ structure are evident in Fig. 4.8 and exhibit an west to east temporal trend. For example, at 0300 UTC southeasterly winds are located in western Oklahoma and the Texas Panhandle with intensities of $\sim$10-15 m s^{-1} at heights of 200-600 m. Then over the following 6 h a southeasterly low-level flow with intensities of $\sim$5-10 m s^{-1} develops in the southeastern half of Oklahoma. Since this enhancement of low-level flow also had a southerly component, the mechanism driving this enhancement may have contributed to moisture advection associated with the southerly NLLJ. Therefore although the low-level southeasterly flow remains relatively weak in southeast Oklahoma, this southerly enhancement may have contributed to the return of convectively unstable conditions. Potential mechanisms for this low-level wind evolution will be examined further in the following section.

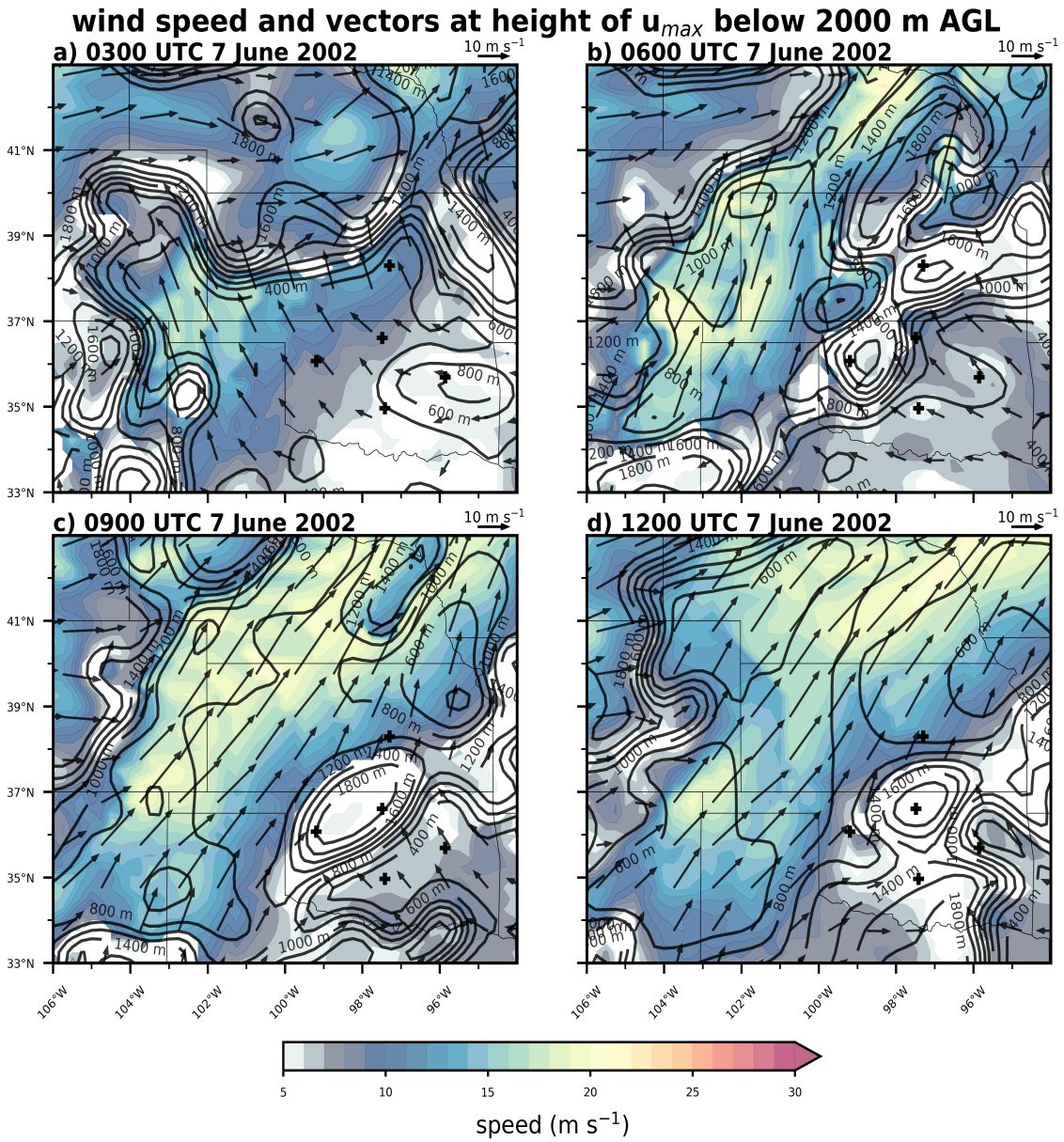

Figure 4.8: Wind speed, height contours (every 200 m, AGL) and vectors taken at the height of the maximum value of $|u|$ (u_{max}) below 2000 m over the Southern Great Plains on 7 June at times: a) 0300 UTC, b) 0600 UTC, c) 0900 UTC and d) 1200 UTC. The location of the 5 ARM sites are indicated by black crosses.

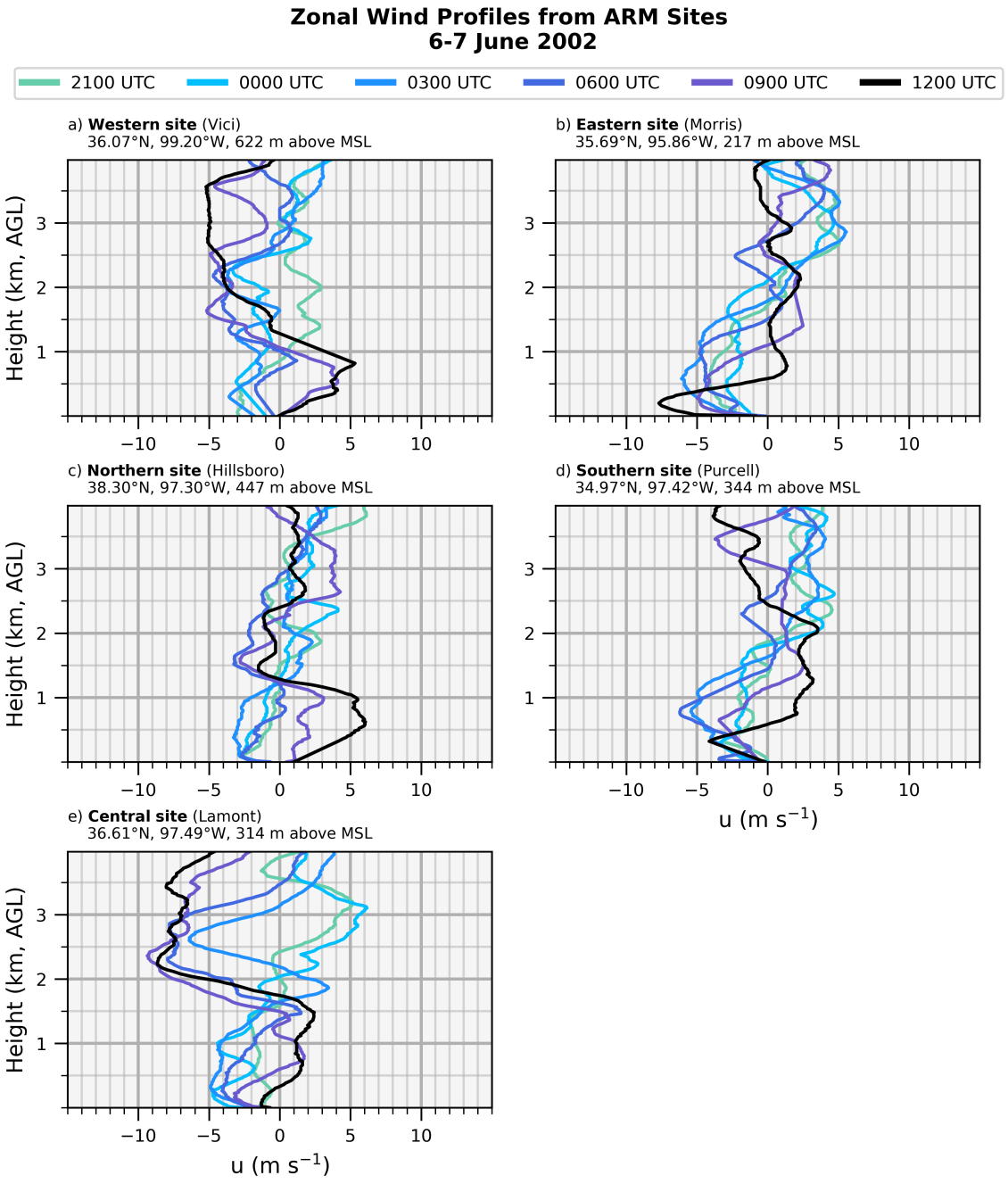

Figure 4.9: Vertical profiles of *u* from 2100-1200 UTC 6-7 June 2002 taken from sounding data collected from the 5 ARM sounding sites: a) western site (Vici), b) eastern site (Morris), c) northern site (Hillsboro), d) southern site (Purcell), and e) central site (Lamont).

4.3 Potential Mechanisms

Vertical θ_v profiles reveal a difference in PBL θ_v values between the western and central sites (306 K versus 302 K) but not the central and eastern sites (Fig. 4.10a,b,e). This differential heating to the west would favor more intense IO's at the western and northern sites. Vertical profiles of the v component are consistent with the most intense southerly NLLJs observed at the western and northern sites (Fig. 4.6). This also supports for mechanism proposed by Parish (2017) for explaining Bonner (1968) climatology, especially since the western site is the nearest ARM site to the frequency maximum of southerly NLLJs. Although evolution of the v_{max} at the western and northern sites are consistent with being produced by an IO, this does not explain evolution at the eastern site which went from 2 m s^{-1} at 0600 UTC to a peak intensity of $\sim$ 11 m s^{-1} at 1200 UTC. Since idealized analytical models and simulations indicate that peak intensity from an IO should occur between 0600-0900 UTC for latitudes of $\sim$35°N (Du and Rotunno 2014; Shapiro et al. 2016; Fedorovich et al. 2017), this suggests other mechanisms may be contributing to the southerly enhancement at the eastern site.

Analysis of surface conditions and θ_v profiles indicate that near uniform heating occurred in eastern Oklahoma. These conditions are favorable for indicating a thermal wind reversal mechanism proposed by Holton (1967) may have influenced NLLJ structure at the eastern site. Evolution of the θ_v profiles at the 5 ARM sites from 0900-1200 UTC were characterized by a strong inversion associated with radiational cooling near the surface (heights below 100 m), with by cooling of $\sim$5 K (Fig. 4.10). The height of the v_{max} at the eastern site is located near the same height above MSL as the surface at the western site, allowing for estimation of effects from a thermal wind reversal. Using a simple thermal wind calculation to determine what impacts could be expected by thermal wind reversal between the eastern and western sites, we find that a thermal wind expected at the eastern site would be $\sim$15 (m s^{-1}) km^{-1}. This finding is consistent with observed changes to v at the eastern site, which had a dv/dz change of $\sim$12 (m s^{-1}) km^{-1} below 500 m from 0600-0900 UTC

(Fig. 4.6b). It is important to keep in mind that these changes in the thermal wind may have been superimposed on other mesoscale or synoptic-scale processes influencing the PGF.

Vertical profiles of the PGF calculated using rawinsonde data from the ARM sites reveals changes occurred from 2100-0000 UTC with magnitudes of $\sim$5-10 hPa (1000 km)$^{-1}$ (Figs. 4.11a,c). Since these changes were relatively uniform with height this suggest they are not the result of baroclinic processes since they imply no change to the thermal wind took place. This perturbation in the PGF exhibited an east-west spatial variation where an intensification occurring between the western and central sites (Fig. 4.11)a), while the PGF to the east decreased by a similar magnitude (Fig. 4.11)c). This spatial variation may offer an explanation for the low-level easterly winds that developed first to the west if this was from an isallobaric acceleration. The timing of intensification to the PGF between the central and eastern sites supports that the easterly intensification at low-levels was isallobaric. Since the uniform enhancement to the PGF implied this was not associated with baroclinic processes, evidence for the cause of the associated pressure perturbation may be found in horizontal divergence fields. For example, if this pressure perturbation is associated with divergence this would support that changes in the PGF are from a mass response.

Horizontal divergence from the ERA5 reanalysis data on the 850 hPa pressure level indicates divergence was occurring between the western and central sites and supporting that the change in the PGF was barotropic. This data indicates that divergence increased by $\sim$5 x10^{-5}s^{-1} to $\sim$10 x10^{-5}s^{-1} over western Kansas and Oklahoma from 2100-0300 UTC (Fig. 4.13a,b). This intensification of divergence was accompanied by convergence increasing by $>$15 x10^{-5}s^{-1} immediately to the west. Although this may be an artifact of its proximity to higher terrain and needs to be taken with caution, it should be noted that convergence was generally weak over this area at 2100 UTC. Changes in wind vectors indicate flow became more easterly and intensified over the same time, consistent with the changes in horizontal divergence resulting from the enhanced easterlies. From this analysis it is not clear how much of this easterly acceleration was isallobaric since based

on the surface pressure field (Fig. 4.2) an IO would also be expected to produce an easterly acceleration between 2100 and 0300 UTC. Since this easterly acceleration was most intense in the vicinity of a gradient in PBL heights, another possible explanation could be the cessation of mixing down of westerly momentum in deeper PBLs to the west as found in dryline simulations by Sun and Wu (1992).

East-west vertical cross sections at the latitude of the northern ARM site were constructed using ERA5 data over points A to B in Fig. 4.13 to help understand the interaction between the pressure field and low-level winds. Heterogeneous PBL heights are evident at 2100 UTC with a deep PBL located west of 105°W with heights of ∼3 km extending into the westerly flow aloft characterized by speeds of ∼10-15 m s^{-1} (Fig. 4.14b). Sun and Wu (1992) found that the mixing down of westerly momentum favored the development of drylines by causing convergence and hindering the westward movement of upslope flow. A relatively linear thermal gradient is also evident in the well mixed boundary layer between ∼104°W and 98°W with warmer air to the west. Conditions at the surface, however, appear to be strongly super-adiabatic. The deepening in the boundary layer and weak ascent occurs near the western edge of the thermal-gradient. The general structure resembles a dryline, but with far weaker gradients in boundary layer characteristics. While the thermal gradient from 103-105°W is associated with an ageostrophic upslope component with magnitudes of ∼10-15 m s^{-1}. The lack of ageostrophic flow west of 102° indicates that the PGF is much weaker and would be less favorable for an easterly acceleration near the surface from the IO mechanism. These findings suggest despite a pronounced low-level easterly component developing by 0300 UTC in Figure 4.8a, the easterly acceleration in southeastern Colorado is not explained very well from an IO.

As noted earlier, easterly low-level flow developed in association with an intensification of the PGF at the ARM sites. This intensification was associated with a negative pressure perturbation (measured as the departure from the 2100-2300 UTC average) evident in the cross sections (Fig. 4.15b). 4.15b depicts a negative pressure perturbations over ∼103°W

and east of 101°W with magnitudes of ∼-1.5 hPa occurring below 3 km (Fig. 4.15b). The pressure perturbation is associated with speed divergence occurring aloft (heights of 5-7 km MSL) which is evident over 103-105°W. This divergence developed as the westerlies intensified from 2100-0300 UTC. The location of this westerly intensification aloft suggests it may be associated with an IO acting on the deeper PBL winds to the west. Wind vectors at 500 hPa are consistent with the effects of an IO occurring at this level near 105°W (Fig. 4.16. The 500 hPa winds near 105°W went from ∼10-15 m s^{-1} out of the northwest at 2100 UTC (Fig. 4.16a), then intensifying and becoming more westerly at 0300 UTC (Fig. 4.16b). Divergence over southeastern Colorado likely resulted from intensification while convergence occurring downstream possibly from the veering effects of an IO. Walters (2001) found similar speed divergence in their composites aloft was found in composites that occurred with low-level jets that developed in quiescent environments.

Although this evolution of mid-level flow offers a plausible explanation for changes to the PGF at low-levels, possible causes of this evolution will be left for future investigations since the focus of this study is on low-level flow. Based on this analysis it is speculated that heterogeneous PBLs created a favorable environment for the development on NLLJs from two contrasting effects acting at low and mid-levels, these effects were: 1) low-level easterly acceleration resulting from the cessation of the mixing down of westerly momentum over the deeper PBL to the west; 2) mid-level divergence from an IO acting on a background northwesterly flow. These two effects favored a low pressure perturbation near the surface on the east side of the PBL transition zone. This speculation is in agreement with Walters (2001) who proposed that the superposition of low-level convergence with upper-level divergence was an important factor in the formation of low-level jets. More quantitative analysis is needed to confirm this, however this speculation links some aspects of work on coupled low-level jets to smaller scales. One possible explanation for the existence of subgeostrophic flow aloft and the transition to geostrophic balance during the night is the mixing of momentum caused by cumulus clouds driven by solar insolation. As these

clouds often decrease after sunset, the flow could return to geostrophic balance. Synoptic influences may have also played a role in this process. Regardless on the underlying mechanisms, perturbations in the PGF associated with heterogeneous PBLs explained several aspects of NLLJ evolution at the ARM sites even though this was occurring much farther west.

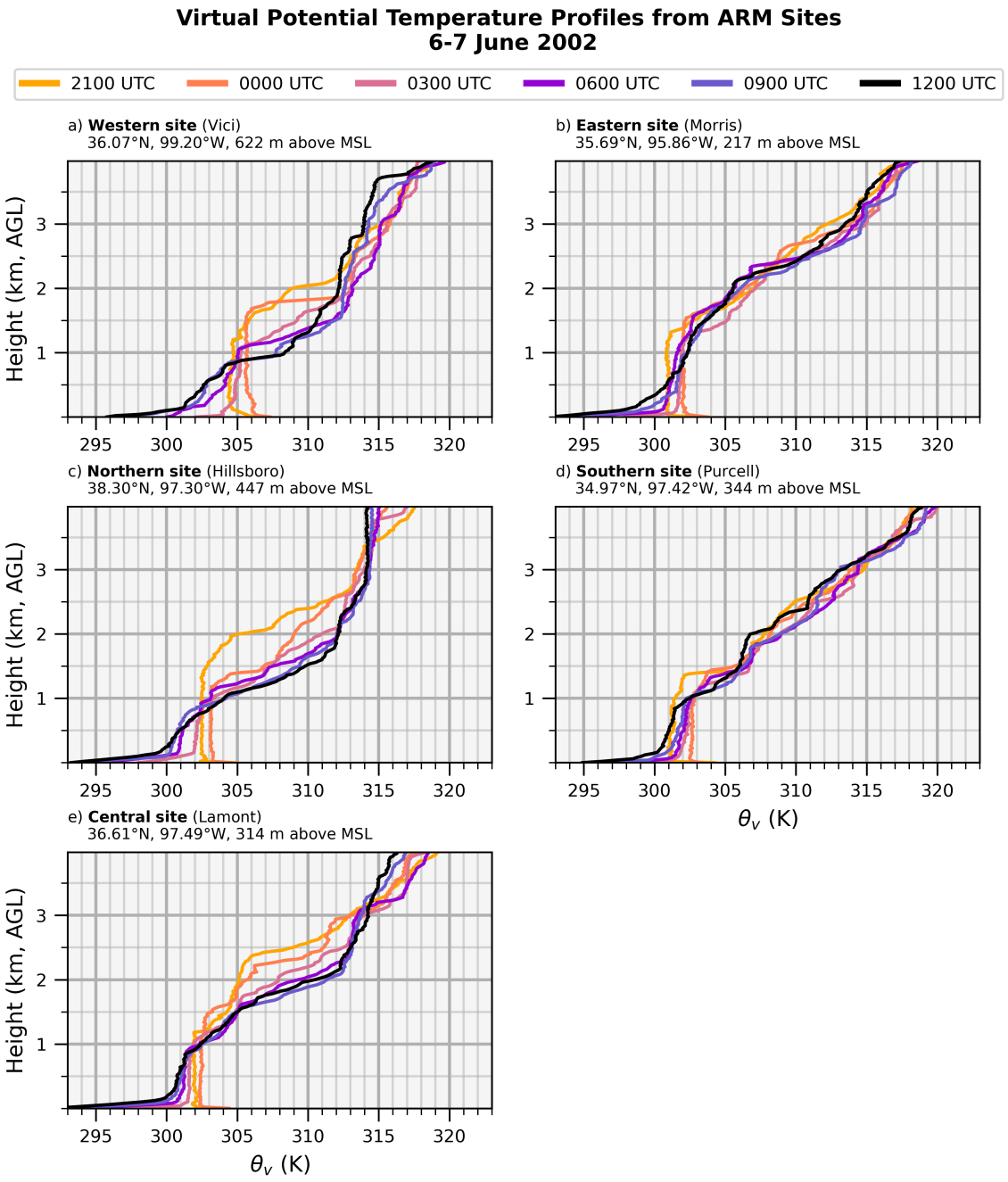

Figure 4.10: Vertical profiles of virtual potential temperature (θ_v) from 2100-1200 UTC 6-7 June 2002 taken from sounding data collected from the 5 ARM sounding sites: a) western site (Vici), b) eastern site (Morris), c) northern site (Hillsboro), d) southern site (Purcell), and e) central site (Lamont).

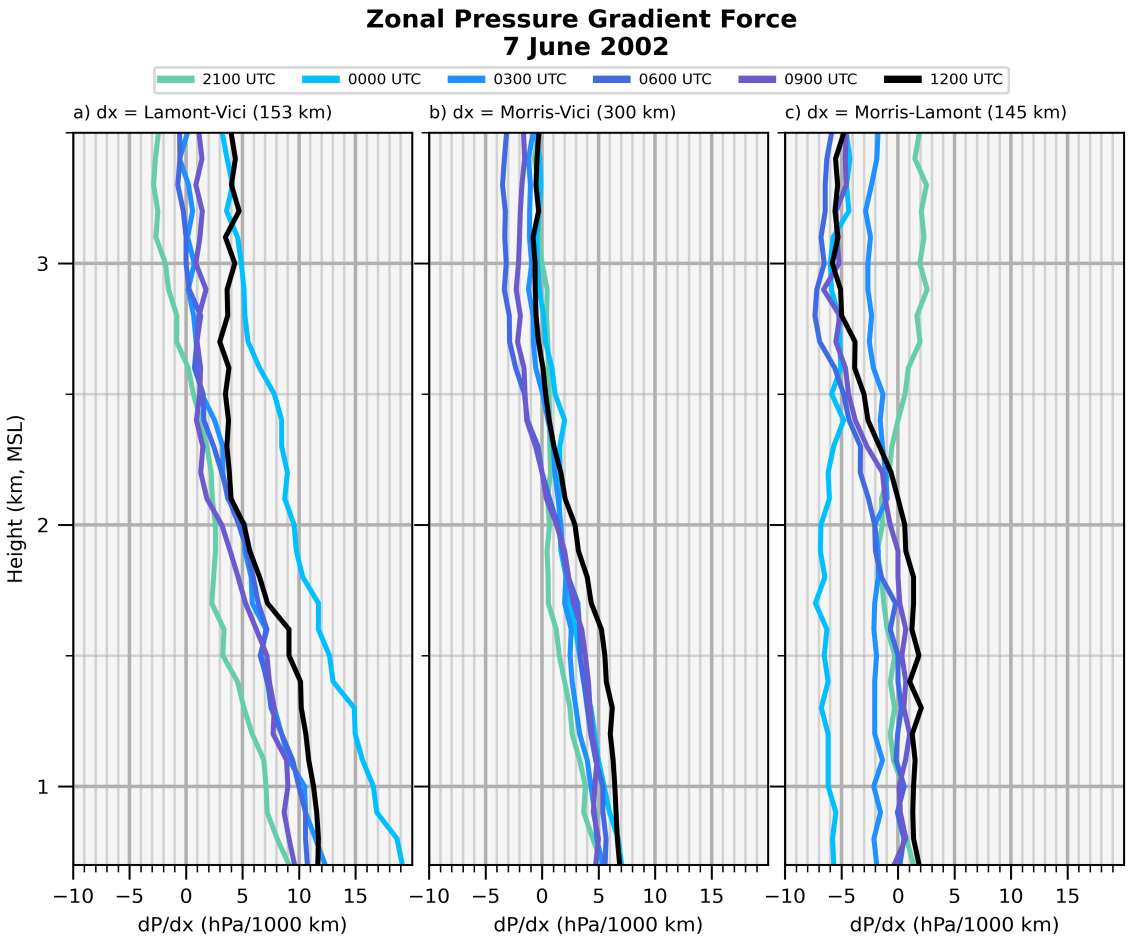

Figure 4.11: The zonal pressure gradient force for 2100-1200 UTC 6-7 June 2002 with the horizontal derivative taken using the horizontal difference between the a) central and western sites, b) eastern and western sites and c) eastern and central sites.

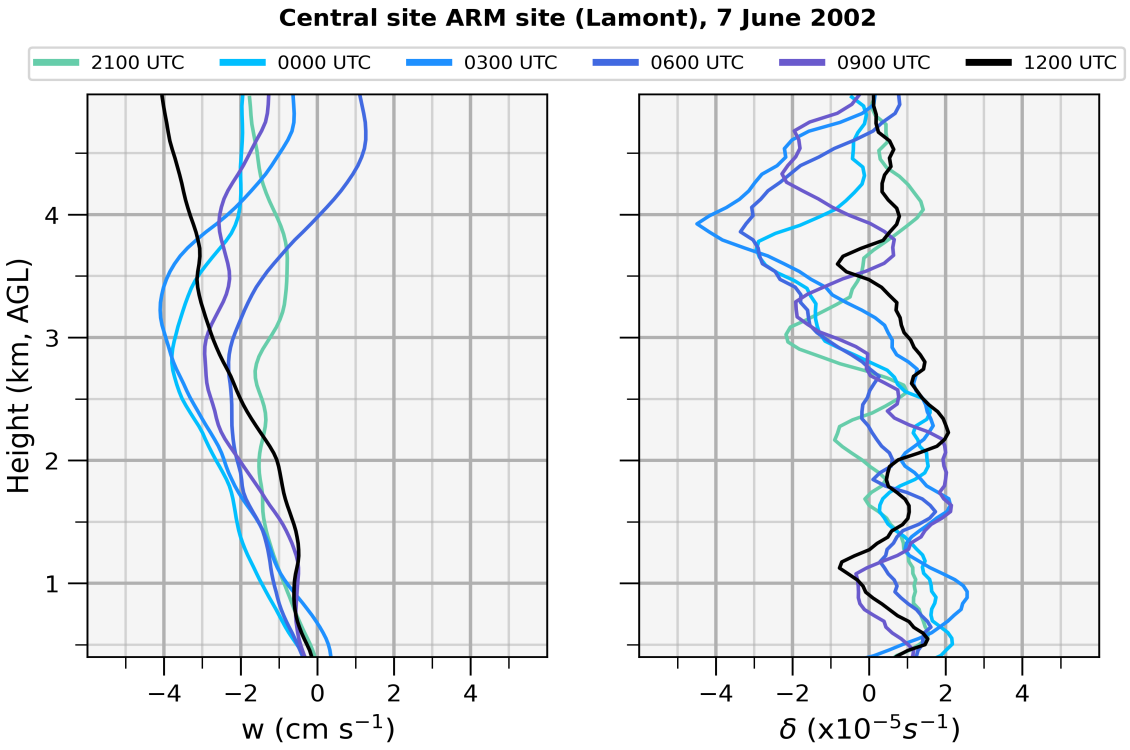

Figure 4.12: Rawinsonde derived profiles of vertical velocity (w) and divergence (δ) valid at the central site (Lamont) from 2100-1200 UTC 6-7 June 2002. Gradients calculated from sounding data collected from 4 ARM sounding sites: western site (Vici), eastern site (Morris), northern site (Hillsboro), d) southern site (Purcell).

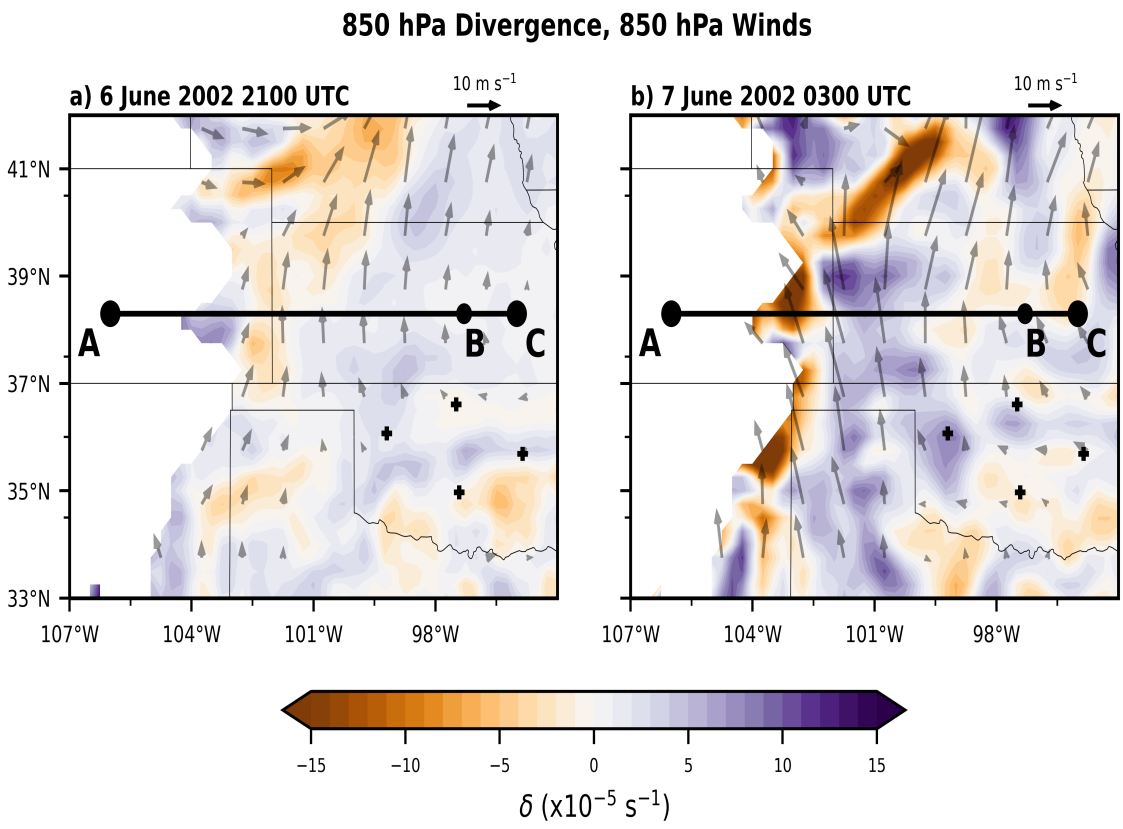

Figure 4.13: Horizontal divergence (δ) and wind vectors for the 850 hPa pressure level from ERA5 reanalysis data for the SGP region at times: a) 2100 UTC 6 June 2002 and b) 0300 UTC 7 June 2002. Black crosses are locations of the ARM rawinsonde sites. The black line shows area where vertical cross sections for figures 4.14 and 4.15 were constructed over.

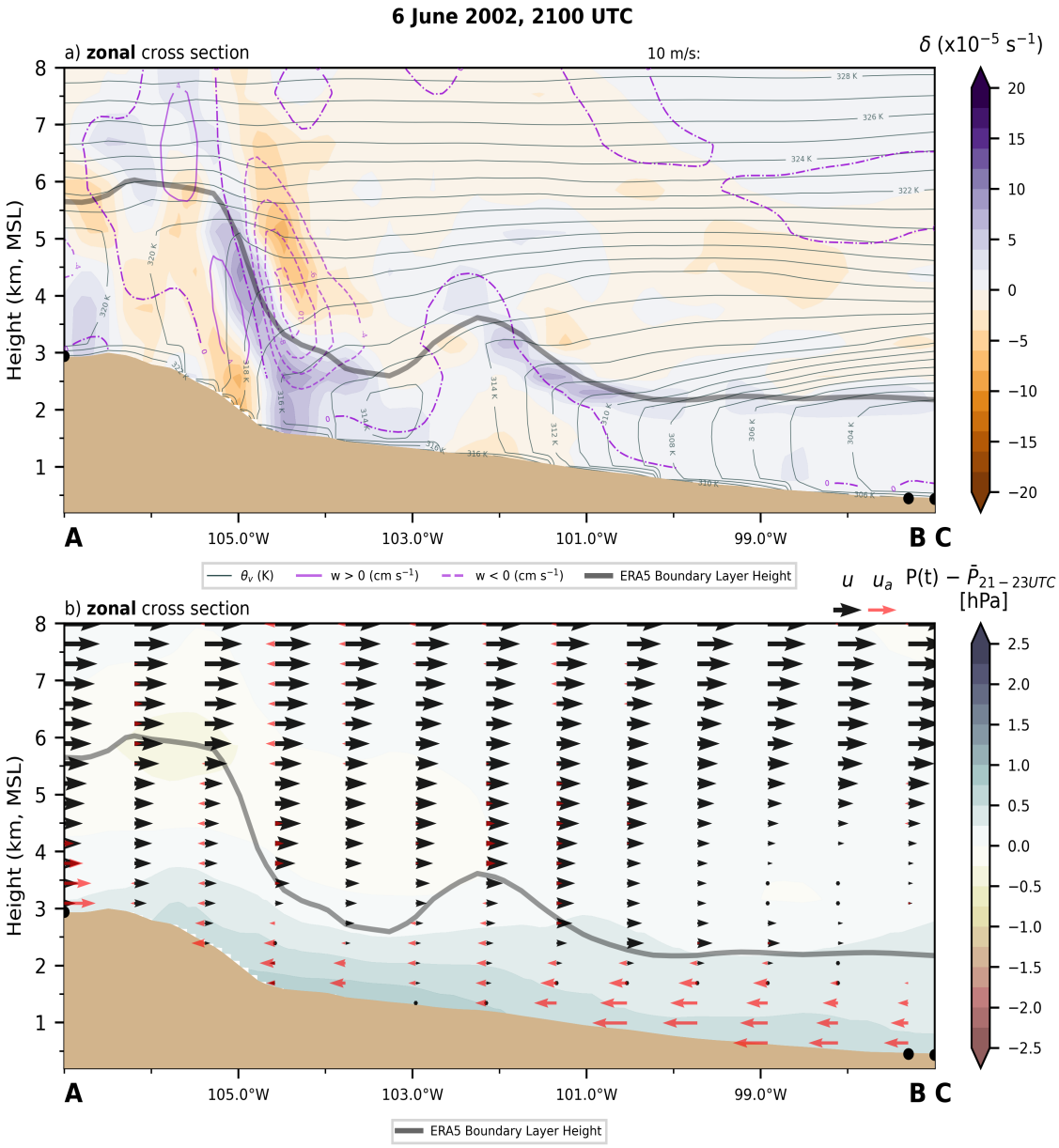

Figure 4.14: Zonal cross sections valid at 2100 UTC 6 June 2002 constructed from ERA5 reanalysis data showing: a) δ (color fill), θ_v (grey contours) and w (solid and dashed violet contours). Averages for perturbations taken from 21-23 UTC 6 June 2002.; b) pressure perturbation (color fill), u component of the wind (black arrows) and u_a component of the wind (red arrows).

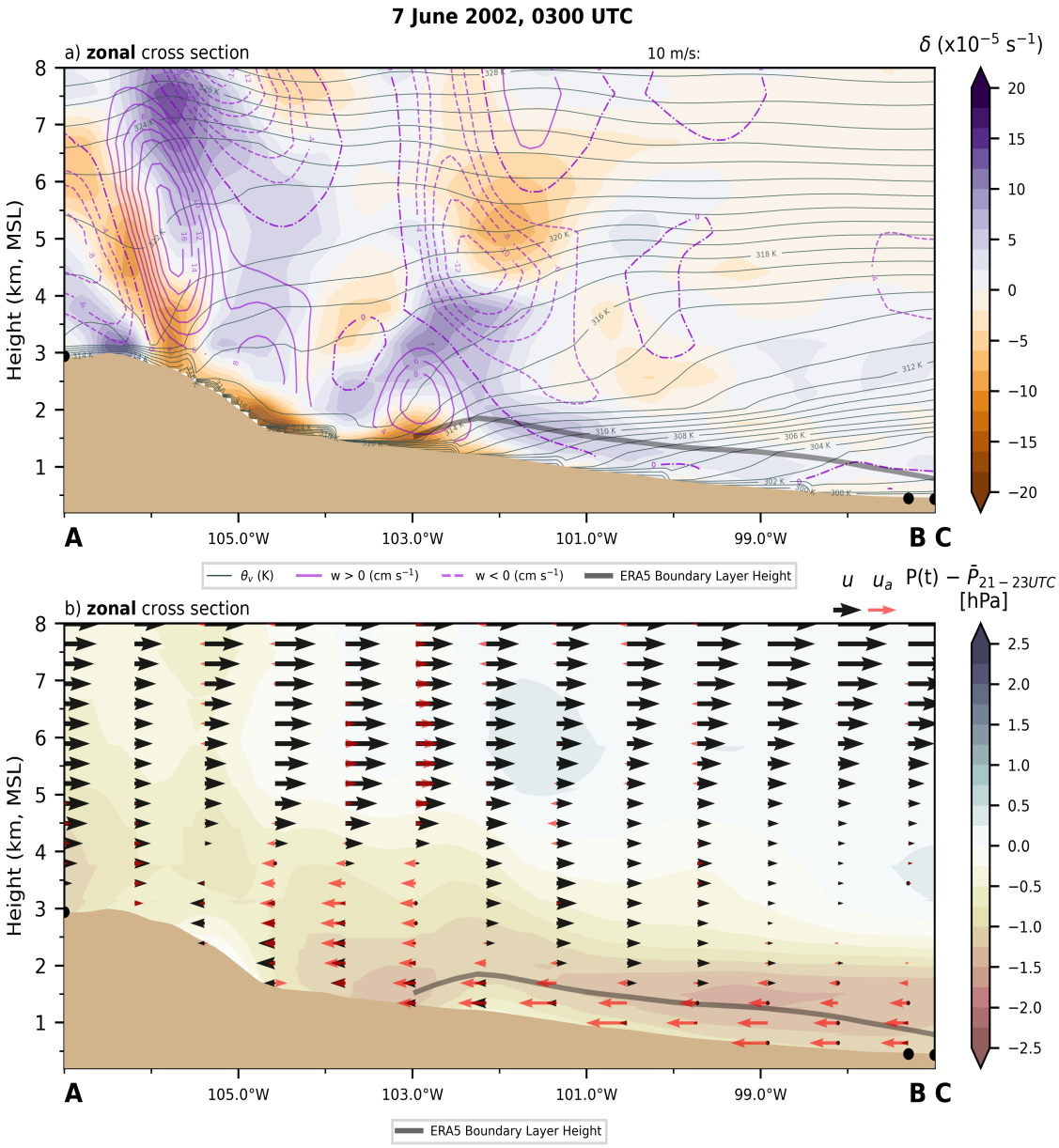

Figure 4.15: As in Figure 4.14 except for 0300 UTC on 7 June 2002

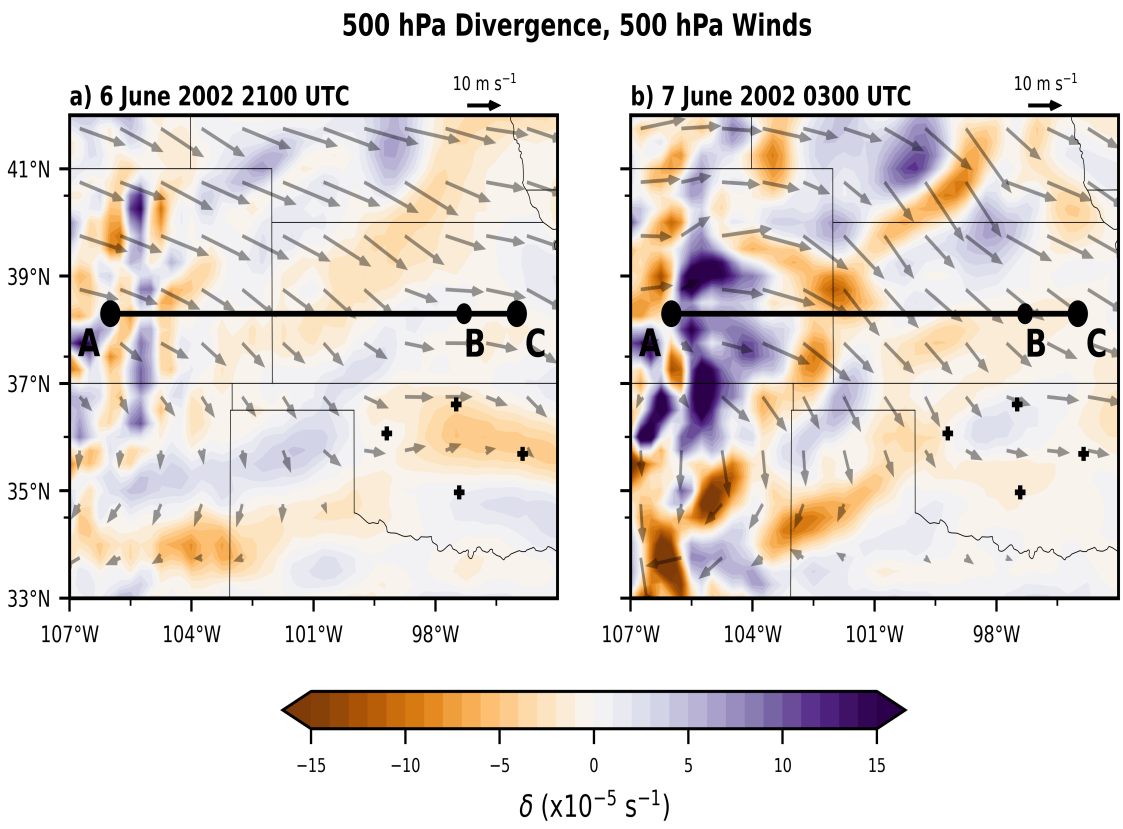

Figure 4.16: As in Figure 4.13 except at the 500 hPa pressure level.

4.4 Discussion

This chapter documented evolution of the NLLJ that developed over the SGP at the onset of a period of rapid moistening. While the southerly NLLJ on 7 June was weak, it was stronger than would be expected from boundary layer mechanisms. Despite being weak, the southerly NLLJ was still able to moisten the environment by transporting moisture from south. The most intense acceleration of the southerly NLLJ occurred at the eastern site where v increased from $\sim$0 m s^{-1} at 0000 UTC to $\sim$10 m s^{-1}. These stronger winds may explain why the largest moistening was observed at the eastern site which moistened by $\sim$4 g kg^{-1} peaking at the height of the southerly NLLJ. The southerly NLLJ exhibited an unusual evolution and structure, deviating from that expected from PBL mechanisms. These unusual characteristics include being more intense and occurring later than what would be expected from an IO mechanism (Du and Rotunno 2014). Southerly NLLJ structure at the eastern site is consistent with changes to v_g expected from a thermal wind reversal associated with the intense and shallow radiational inversions at the ARM sites.

Vertical profiles of the zonal PGF from the ARM sites indicate a pressure perturbations on scales of $\sim$150 km may have contributed to evolution of the NLLJ. This is especially evident in the evolution of u component of the wind at the central site. This pressure perturbation appears to be associated with low-level easterly flow. The core of the southerly NLLJ was located in eastern Colorado and western Kansas, with intensities of 15 to 20 m s^{-1}. Evolution of the southerly NLLJ was tied to a negative pressure perturbation which appeared to have been induced by easterly upslope flow that developed after decoupling. This upslope flow likely resulted in low-level divergence and associated subsidence at heights near upper portions of the daytime PBLs at the ARM sites.

Chapter 5

Moistening Phase

This chapter documents evolution of the NLLJ on 8 June 2002 and how it was associated with the return of conditions favorable for convection following the 5 June frontal passage. A different organization than the previous chapter is used to accommodate the additional goal. This new organization begins with an overview of synoptic and mesoscale conditions followed by analysis of vertical cross sections. Subsequent sections examine rawinsonde data from the 5 ARM sites to provide a better understanding of the association between NLLJ evolution and destabilization.

5.1 Synoptic Conditions

Calm synoptic conditions persisted over the ARM sites on 8 June, with a zonal 500 hPa flow of $\sim$5-15 m s^{-1} over the southern half of Nebraska, decreasing into Kansas and Oklahoma to $<$5 m s^{-1} (Fig. 5.1). Analysis of surface θ_v suggests the stronger mid-level flow in Nebraska was associated with a cold front. θ_v fields indicate north-easterly surface winds were co-located with a negative θ_v gradient (decreasing θ_v to the north) (Fig. 5.2). This cold front remained north of the Nebraska-Kansas border throughout the night (Fig. 5.2), so it is unlikely to have directly influenced NLLJ evolution at the ARM sites. The 500 hPa height field indicates a trough moving in from the west, located over Idaho and Utah (Fig. 5.1). Although the 500 hPa trough was located too far west to be a concern at this time, this synoptic flow regime has been associated with dryline formation (Mitchell and Schultz 2020).

A developing dryline was evident by an increasing moisture gradient extending from the Texas Panhandle to the Nebraska-Kansas border (latitudes of $\sim$35-39°N) on 8 June. In the late afternoon, this moisture gradient was characterized by mixing ratio values increasing

by $\sim$8 g kg^{-1} to the east, occurring over a distance of $\sim$200 km (longitudes of $\sim$100-102°W) (Fig. 5.2). This gradient in boundary layer characteristics is also reflected in PBL heights from the ERA5 reanalysis data (Fig. 5.3). This gradient is characterized by boundary layer depths of $\sim$1000 to 1250 m over western Oklahoma and central Kansas increasing to $\sim$2500 m along the borders of Colorado/Kansas and New Mexico/Texas. As with the previous date (7 June), another gradient in boundary layer depths is located in central Colorado and is also associated with a surface low located in eastern Colorado. Surface winds over most of the domain (south of $\sim$41°N and east of 105°W) were mainly southerly as a result of a surface low located in northeastern Colorado (Fig. 5.2). As with 7 June, a second gradient in PBL heights is located in north-central Colorado, on the edge of stronger mid-level flow. Although these conditions are generally similar to 7 June, one difference is that the southerly surface winds are more intense and extend further east. This surface low resembles does resemble that expected from a lee trough, however, the association between it's location and the thermal gradients suggest that it is at least partly driven by daytime surface heating. These surface conditions are favorable for the development of southerly NLLJs, owing to the inertial oscillation acting on the southerly surface v_g in-place during the day (Parish 2016).

The v_{max} below 2 km obtained from ERA5 data suggests the core of the southerly NLLJ was located in eastern Colorado and northwestern Kansas, occurring at heights of 800-1000 m and reaching a peak intensity of 25-30 m s^{-1} at 0600 UTC (Fig. 5.4). Evolution of v_{max} was characterized by wind vectors veering with time, being southerly at 0300 UTC (Fig. 5.4a) and becoming more southwesterly with time. The magnitude of veering was not spatially uniform, wind vectors west of $\sim$100° exhibited more pronounced veering with time. For example, over central Oklahoma and Kansas the direction of the v_{max} wind vectors remain the same or even become slightly more easterly from 0300 to 0600 UTC, meanwhile in the eastern Texas Panhandle and western Kansas the direction goes from southeasterly to southwesterly (Fig. 5.4a,b). This convergence pattern continues to shift

east overnight, being located near the central and northern sites at 0900 UTC (Fig. 5.4c), 3 h later it is located between the central and eastern site (Fig. 5.4d).

As with the v_{max}, the u_{max} also exhibited heterogeneous characteristics, this was more evident in earlier hours. At 0300 UTC a westerly u_{max} located above the v_{max} occurring west of $\sim$99°W, meanwhile to the east, the u_{max} was southeasterly and located at heights of 200-400 m (Fig. 4.8a). The heterogeneous pattern of the u_{max} became more complex at 0600 UTC with the u_{max} becoming westerly and elevated over most of Oklahoma, with speeds of 5-10 m s^{-1} at heights of 1800-2000 m, meanwhile over the core of the southerly NLLJ the u_{max} intensified to speeds of $\sim$25 m s^{-1} and became more shallow, being located at heights of 1000-1400 m (Fig. 4.8b). In later hours the u_{max} became more uniform. At 0900 UTC the u_{max} over north-central Oklahoma and central Kansas became more similar to that occurring over the core of the southerly NLLJ, where it was characterized by speeds of 15-20 m s^{-1} at heights of 800-1400 m (Fig. 4.8c). Relatively little change occurred in the u_{max} from 0900-1200 UTC compared to earlier hours with the most notable change being a reduction in speed of $\sim$5 m s^{-1} over northwestern Kansas and eastern Colorado (Fig. 4.8d).

As noted earlier similarities between 7 and 8 June were present in mesoscale conditions during the daytime. Analysis of ERA5 data indicates that in both cases the core of the NLLJ was located directly east of the surface low in northeast Colorado. This surface low was also located directly east of a gradient in PBL heights with deeper boundary layers to the west. On 7 June it was suspected that these features may have produced a mesoscale pressure perturbation when decoupling in the deeper boundary layer resulted in mid-level divergence while decoupling in the shallow boundary layer to the east triggers an upslope surge near the surface. The combined effects favored an area of low-level divergence and likely resulted in a mesoscale pressure perturbation in the shallow boundary layer to the east. An easterly u_{max} was evident at 0300 UTC on 8 June in the eastern boundary layer.

This suggests that easterly flow may have contributed to a pressure perturbation in a similar process to a day earlier.

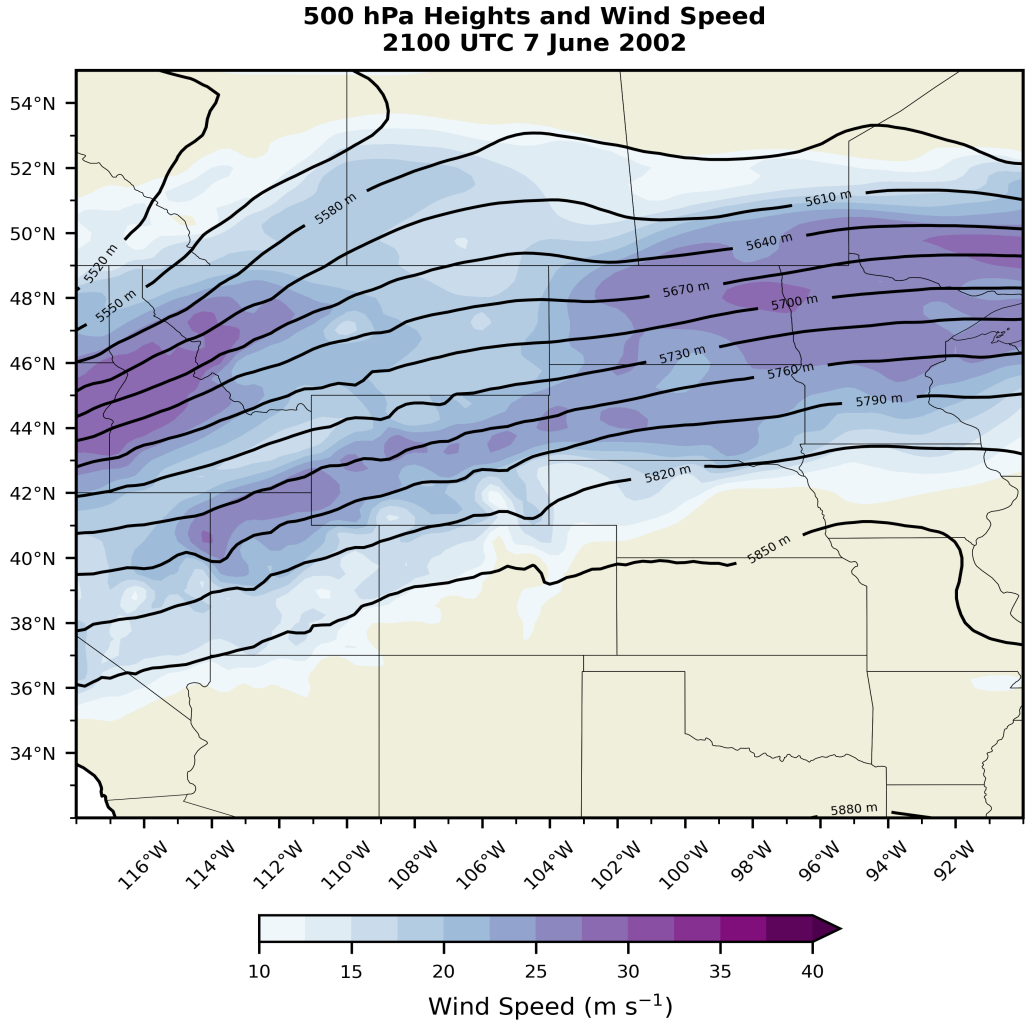

Figure 5.1: As in Figure 4.1 except for 2100 UTC 7 June 2002.

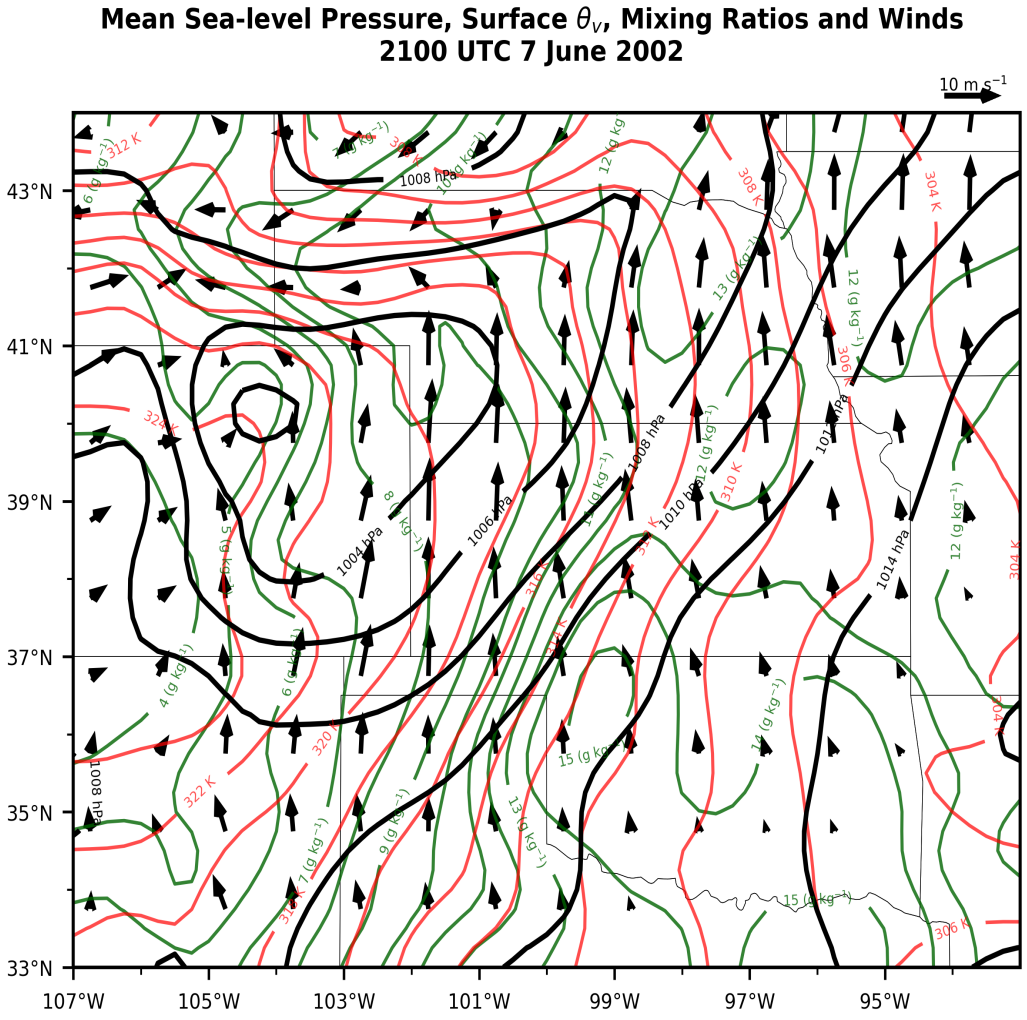

Figure 5.2: As in Figure 5.2 except for 2100 UTC 7 June 2002.

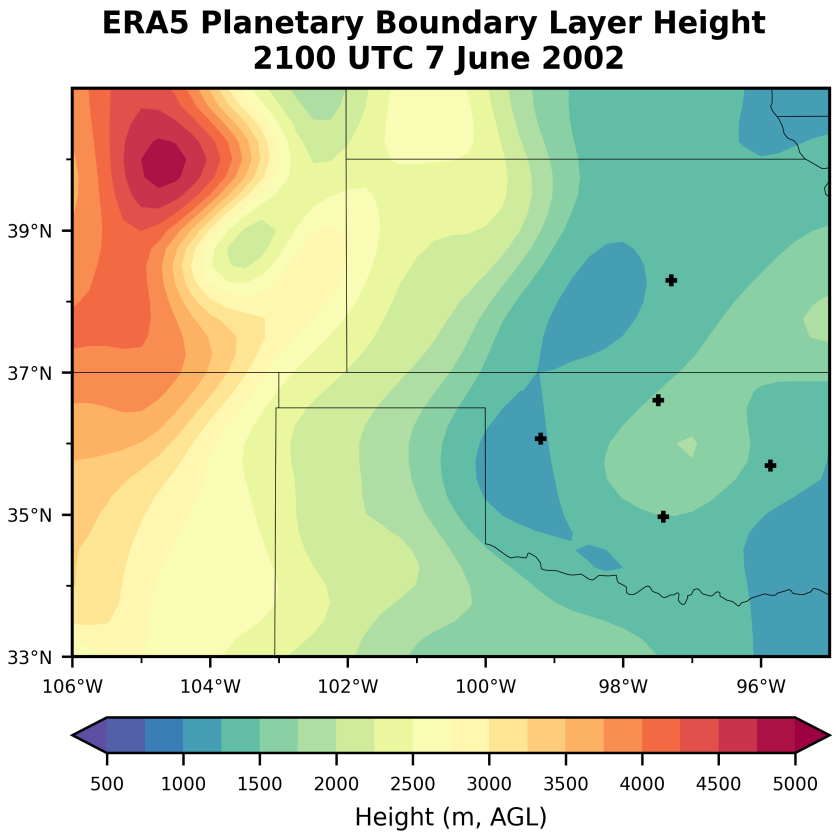

Figure 5.3: As in Figure 4.3 except for 2100 UTC 7 June 2002.

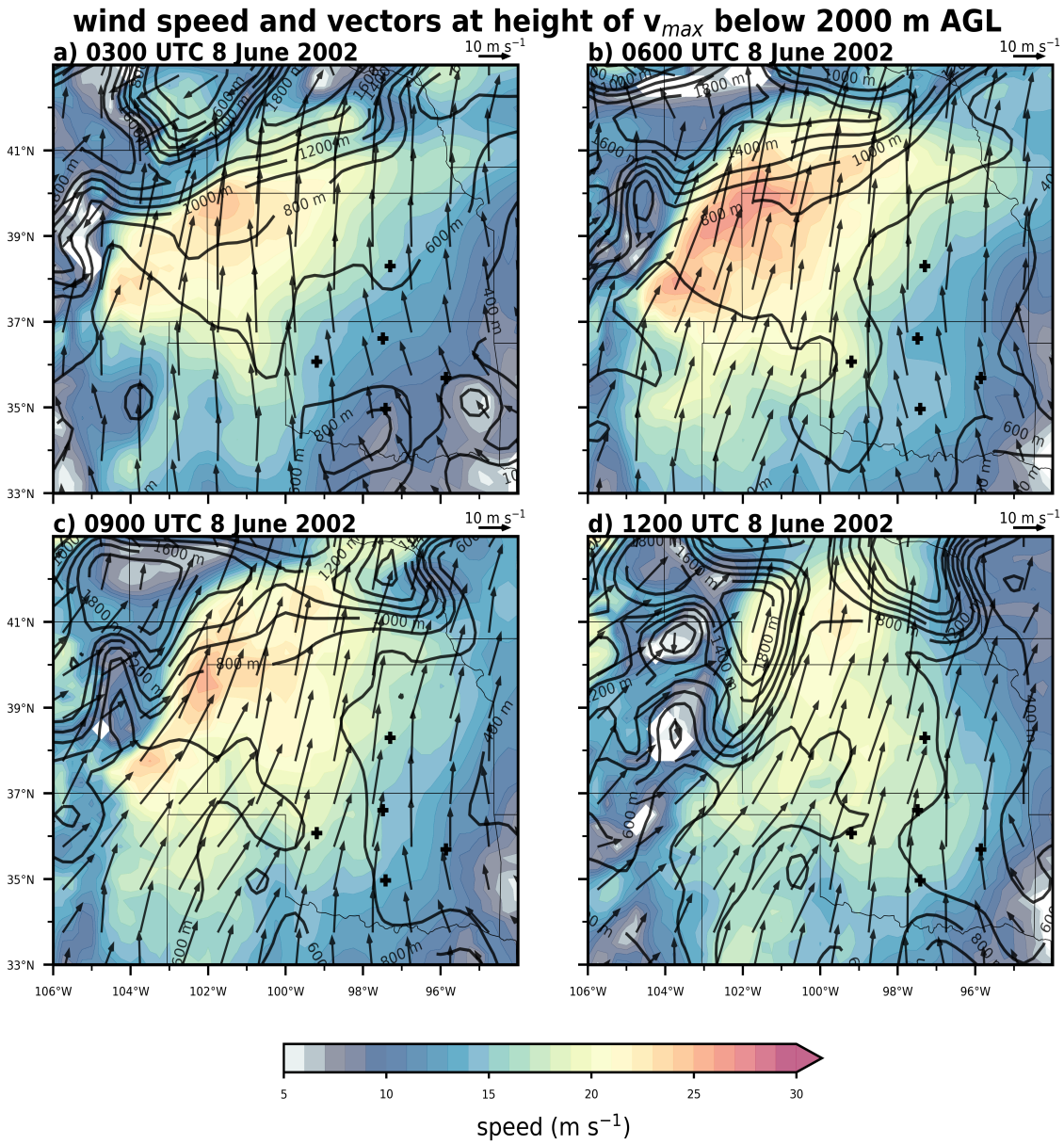

Figure 5.4: As in Figure 4.4 except for 8 June 2002 at times: a) 0300 UTC, b) 0600 UTC, c) 0900 UTC and d) 1200 UTC.

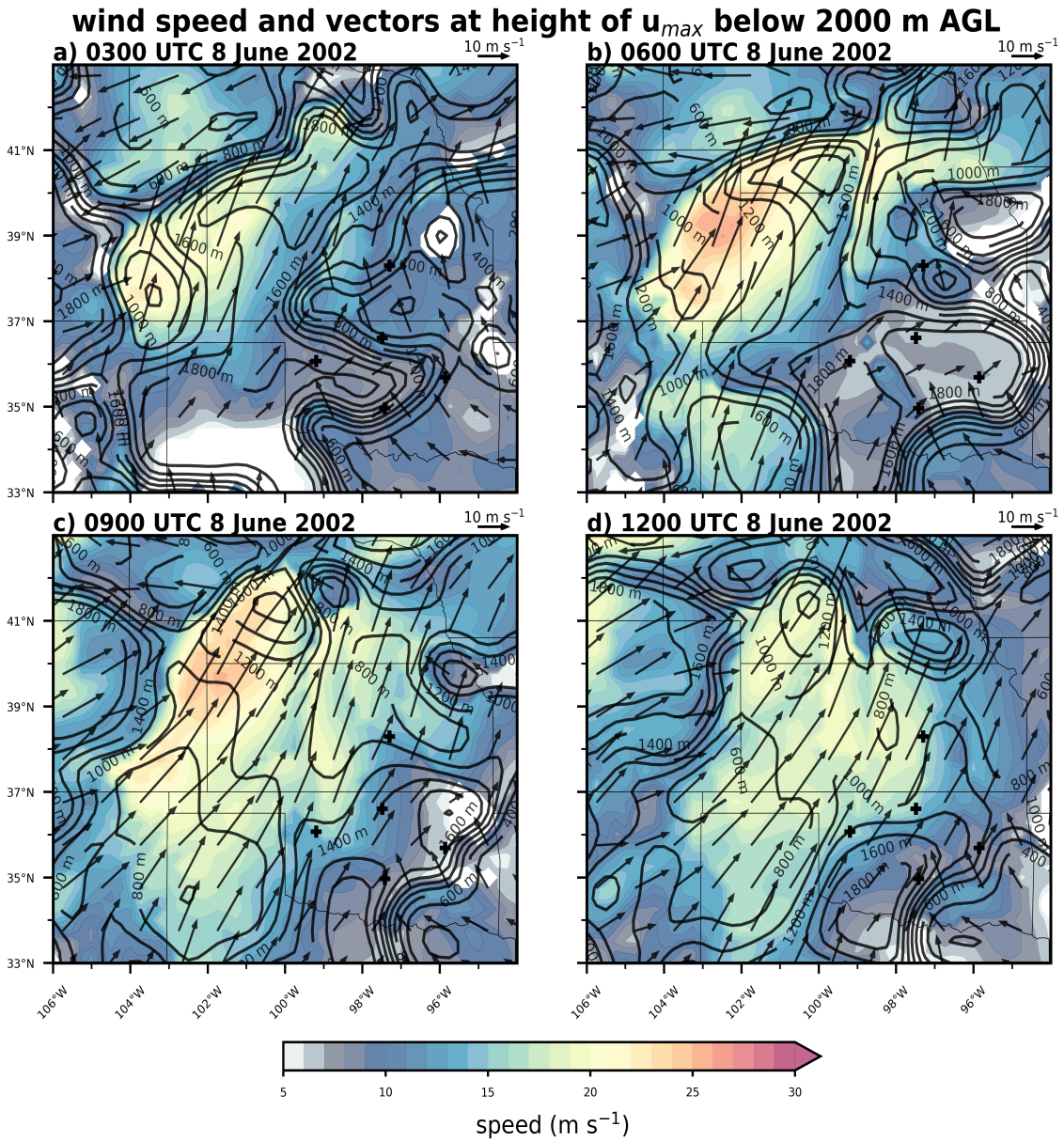

Figure 5.5: As in Figure 4.8 except for 8 June 2002 at times: a) 0300 UTC, b) 0600 UTC, c) 0900 UTC and d) 1200 UTC.

5.2 Analysis of Meridional Cross Sections

North-south vertical cross sections in Figure 5.6 were constructed using ERA5 data to provide insight on evolution of the vertical structure of the southerly NLLJ on 8 June and how this evolution contributed to moistening the environment. These cross sections reveal low-level southerly flow of 15-20 m s^{-1} being in-place over most of the night north of 37°N at heights below 2 km MSL. Values of $v_a + v_g$ at heights of 800-1000 m are consistent with magnitudes of the v_{max} noted earlier. The most intense southerly flow was located over latitudes where the sharpest gradients in PBL characteristics along the slope were located (∼37-41°N) (Figs. 5.6a,b,c,d). This area exhibited a similar pattern of intensification to the day prior (7 June). This pattern was characterized by an intensification of v_g by ∼5-10 m s^{-1} taking place from 0300-0600 UTC and located over latitudes of ∼37-39°N. This intensification was followed by a decrease of ∼5 m s^{-1} from 0600-0900 UTC, then an intensification of 10-15 m s^{-1} over the subsequent 3 h. The lack of changes in v_a suggest a geostrophic intensification of the southerly NLLJ. These large variations in v_g observed in ERA5 cross sections appear to be relatively uniform over depths of 1-2 km, the lack of a change in the thermal wind is indicative of the PGF being impacted by a barotropic pressure perturbation.

Although variations of v_g were smaller in magnitude to the south, enhancements to the depth of v_g were associated with deeper moisture advancing from the south. From 0600-1200 UTC, a deeper intensification of the v_g appears to have contributed to moisture advection. At 0600 UTC, mixing ratios of 10-12 g kg^{-1} were located over the 1-1.5 km MSL layer at the central site, becoming deeper south of 35°N (Fig. 5.6b). By 0900 UTC, this deeper layer of moisture to the south was located near 37.5°N (Fig. 5.6c), 3 h later it is located over 37.5-38.5°N (Fig. 5.6d). Even greater moisture is seen advancing north from 0900-1200 UTC south of 35.5°N (Fig. 5.6b,c). This pattern suggests that the deeper v_g enhancement was contributing to moistening on 8 June and moisture advection not confined to the v_{max} of the southerly NLLJ.

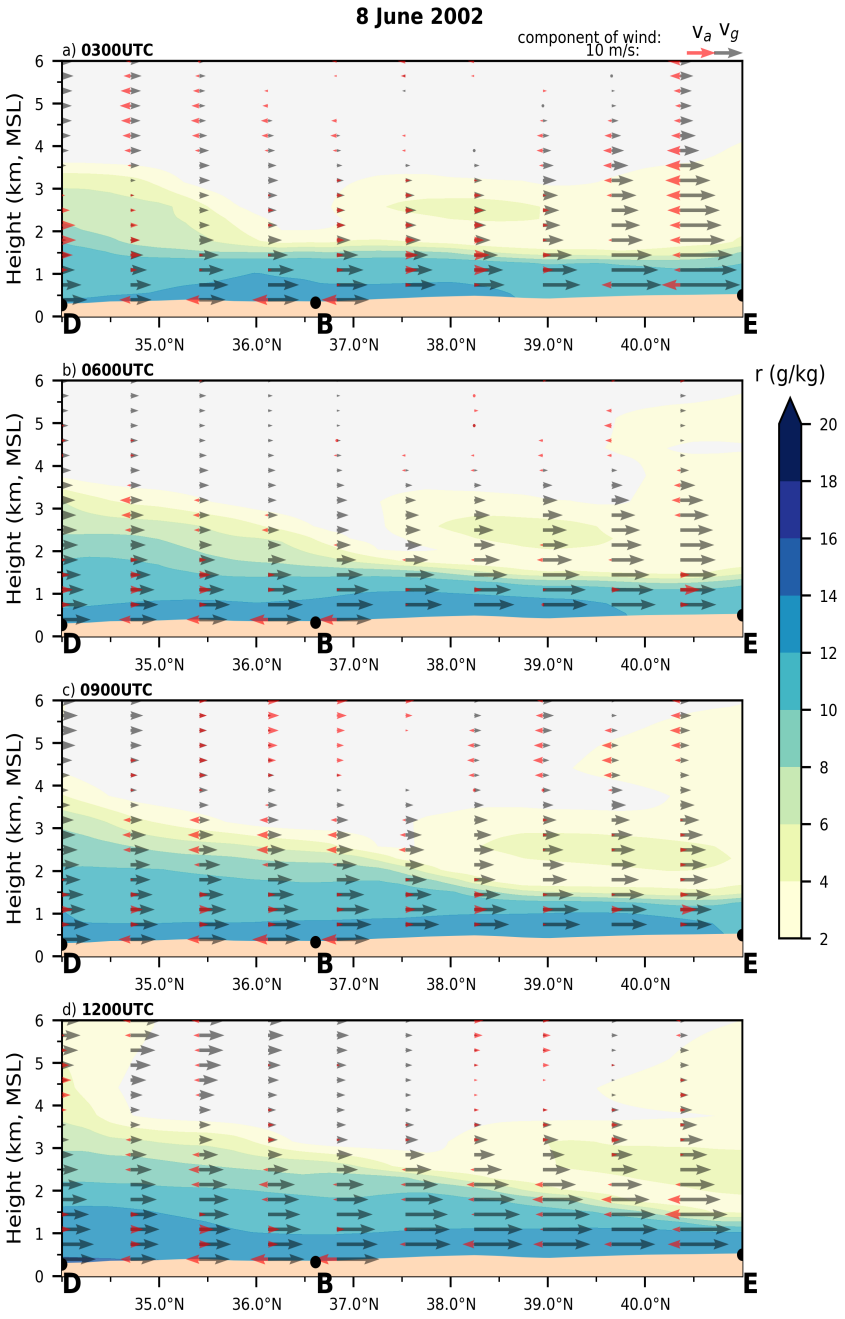

Figure 5.6: As in Fig. 4.5 except for 8 June 2002.

5.3 Analysis of Zonal Cross Sections

Zonal vertical cross sections indicate the evolution of the NLLJ was associated with variations PBL characteristics along the slope during the daytime. These variations in PBL characteristics reveal three distinct PBLs were in-place during the daytime, with a deep, warm and dry PBL located west of 105°W (hereafter referred to as: dry PBL) and a shallow, cool and moist PBL east of 101°W (hereafter referred to as: moist PBL) and a PBL with intermediate characteristics in between (hereafter referred to as: transition PBL). The dry PBL was characterized by PBL heights of ∼4 km, θ_v values of ∼322 K and mixing ratio values of 2-4 g kg^{-1}. In contrast, the moist PBL was characterized by depths of ∼1 km, θ_v values of 315-310 K and mixing ratio values of 8-12 g kg^{-1}. Differences between the transition PBL and moist PBL resulted in a low-level θ_v gradient. This gradient suggests that southerly surface winds were being enhanced by the θ_v gradient along the slope. A local maximum in southerly geostrophic winds were associated with this θ_v gradient, where v_g was characterized by values of ∼20 m s^{-1} at the surface which decreased to ∼0 m s^{-1} at the top of the PBL from 98-102°W. These results are in agreement with findings from Parish (2016) which suggested that the southerly NLLJs often develops as a result of the IO mechanism acting on the enhanced southerly v_g from daytime heating.

For the first several hours after sunset (0300-0600 UTC), intensity of the southerly NLLJ in the moist PBL does indeed correlate to areas with the largest v_g at 0000 UTC, however this correlation does not hold true west of 103°W. For example, v_g is ∼5 m s^{-1} less at 103°W compared to 102°W at 0000 UTC. However both locations have a southerly NLLJ of ∼20 m s^{-1} at 0600 UTC (Fig. 5.9a,b). This discrepancy is occurring near the boundary between the dry PBL and transition PBL, which has a kinematic structure resembling a dryline (Ziegler and Hane 1993; Atkins et al. 1998; Demoz et al. 2006; Buban et al. 2007). Here ascent of ∼14 cm s^{-1} along with convergence near the surface and divergence at the top of the PBL is occurring on the western side and subsidence with an inverted δ profile of a similar magnitude is occurring on the eastern side of the boundary

(Fig. 5.7a,b). Since a more pronounced example of this circulation occurs on 10 June, the possible impacts of this gradient to NLLJ evolution will be explored further in chapter 6. Although this circulation was located far west of the ARM sites, some changes in the w field occur over these sites and may be associated with this gradient. Evolution of the w field was further associated with changes to the orientation of the isentropes along the slope, possibly impacting NLLJ evolution by modifying the baroclinic zone that developed during the daytime.

Decreases in v_g near the surface (at heights $<$500 m) from 0300-0600 UTC was associated with a weaker southerly NLLJ. Changes to the θ_v gradient may offer an explanation for this decrease in v_g. For example, at 101°W, v_g decreased by $\sim$5 m s^{-1} at heights below 500 m (Figs. 5.7a and 5.9a), coinciding with a decrease in the $\Delta\theta_v$ from $\sim$4 K to $\sim$0 K between 101-102°W (Figs. 5.7b and 5.9b). One possible explanation for these changes are more rapid surface cooling to the west. The impacts of this cooling to v will be examined in subsequent sections in this chapter. Changes to the θ_v gradient were also associated with a broad area of subsidence occurring over the transition PBL.

Subsidence over the transition PBL was characterized by vertical velocities of -8 cm s^{-1} to -6 cm s^{-1} at heights of 2-4 km, lowering and intensifying from 0000-0600 UTC (Figs. 5.7b,5.8b,5.9b). This descent was complemented by ascent of similar magnitudes occurring in the moist PBL after 0600 UTC (Fig. 5.9b). This dipole of subsidence to the west and ascent to the east may have contributed to isentropes sloping down to the west at heights of 2-3 km MSL due to vertical advection, this will be examined in more detail later in this chapter using rawinsonde data. This change to the orientation of isentropes was associated enhancements of $\sim$5 m s^{-1} to the southerly v_g occurring directly above the v_{max}. The suspected interplay between vertical velocities, θ_v and v was occurring at 1200 UTC near 99°W. Here a local maximum of ascent with values of $\sim$4 cm s^{-1} is occurring at heights of 2-3 km MSL, coinciding with isentropes developing a much more vertical orientation, along with v_g increasing by 2-5 m s^{-1} from 3 h earlier (Figs 5.10a,b and 5.11a,b).

This warming may have contributed to geostrophic enhancements to v through effects on thermal wind but more quantitative analysis is needed to confirm whether these enhancements were geostrophic (Figs. 5.10b and 5.11b).

The ascent occurring at 1200 UTC near 99°W was associated with convergence at the height of the westerly NLLJ (heights of 1-2 km) (Fig. 5.11a,b). Similar convergence has been documented with NLLJs during the PECAN field campaign (Gebauer et al. 2018; Smith et al. 2019). Gebauer et al. (2018) and Smith et al. (2019) proposed that ascent may result from convergence due an IO acting on differential PBL geostrophic winds along the slope. Their mechanism suggest this occurs when the deeper PBLs to the west undergo a more intense IO due to more intense frictional forces in their daytime PBL. The NLLJ on 8 June 2002 exhibits a similar evolution to cases documented by Gebauer et al. (2018) and Smith et al. (2019), characterized by a greater westerly enhancement west of 99°W. However, at 0000 UTC there is a lack of variation in PBL characteristics from 99-101°W and the geostrophic winds increased by $\sim$5 m s^{-1} to the west with little to no change in depth. The lack of variations in the PBL v_g along the slope raises some doubt that the ascent can be explained by the IO mechanism associated with heterogeneous PBL as proposed by the two previous studies. Since it was pointed out earlier that changes in the orientation of isentropes near the surface along western portions of the slope were consistent with more rapid surface cooling to the west, the Shapiro et al. (2016) mechanism may provide an alternative explanation for the westerly enhancement above the southerly NLLJ.

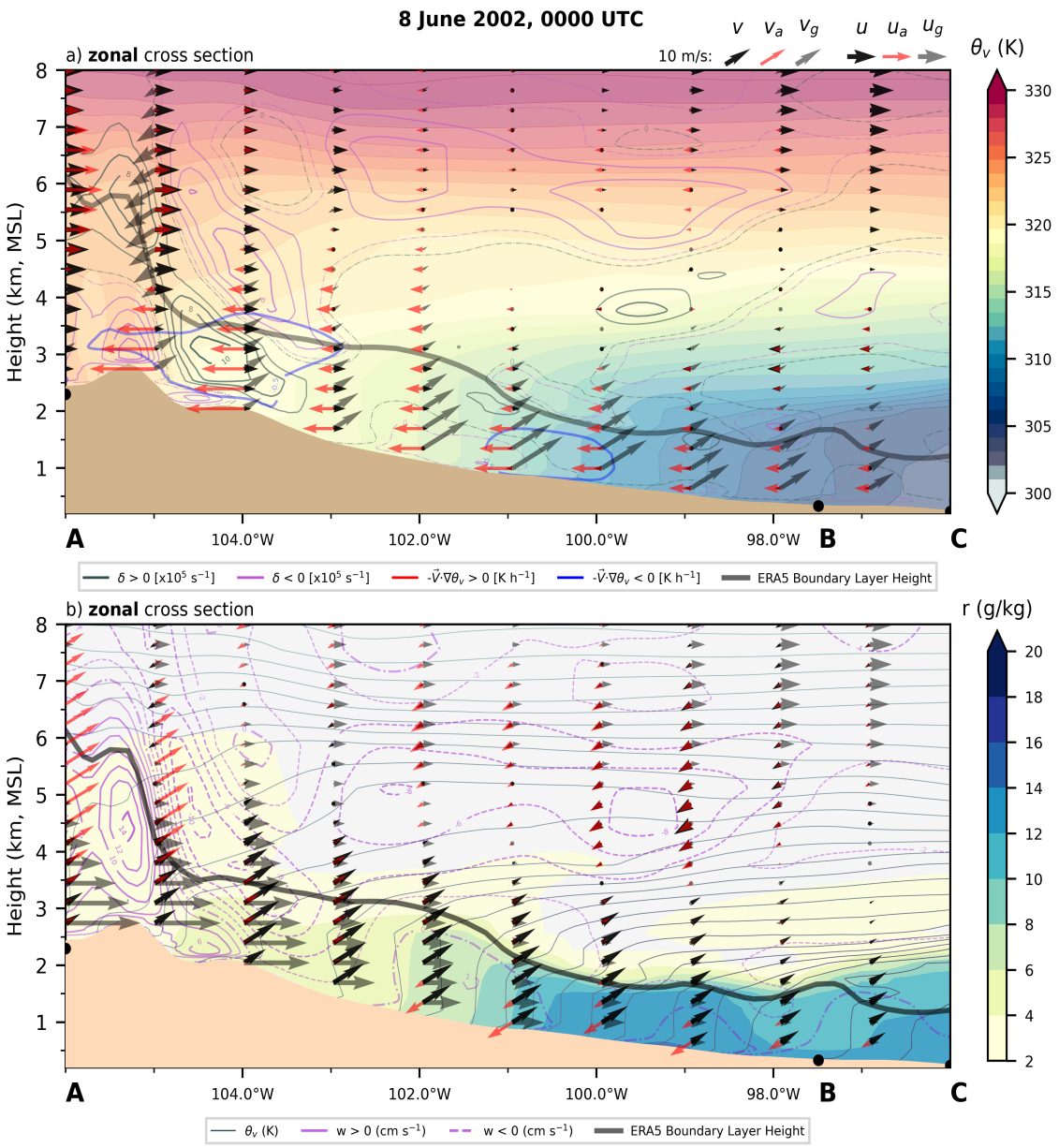

Figure 5.7: 0000 UTC 8 June zonal cross section from 96-106°W at 36.75°N, over the central site (B). Constructed from ERA5 reanalysis data containing geostrophic winds (black arrows), ERA5 boundary layer height ageostrophic zonal winds (red arrows) and for the top panel (a): θ_v color-fill, divergence (dark green contours), convergence (purple contours) and bottom panel (b): mixing ratio (color fill), θ_v (black contoured every degree K), w (purple contours).

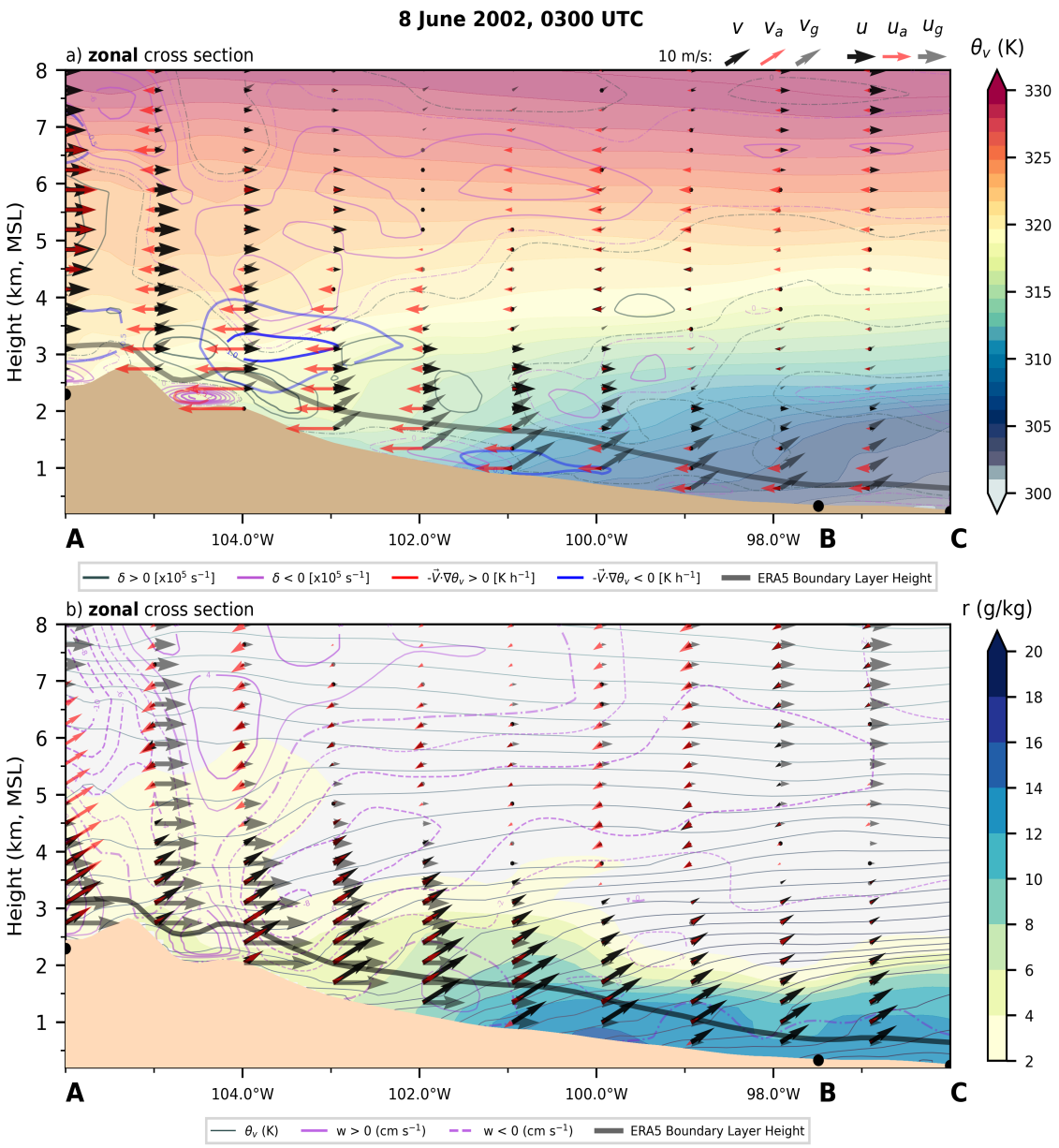

Figure 5.8: As in Figure 5.7 except for 0300 UTC 8 June.

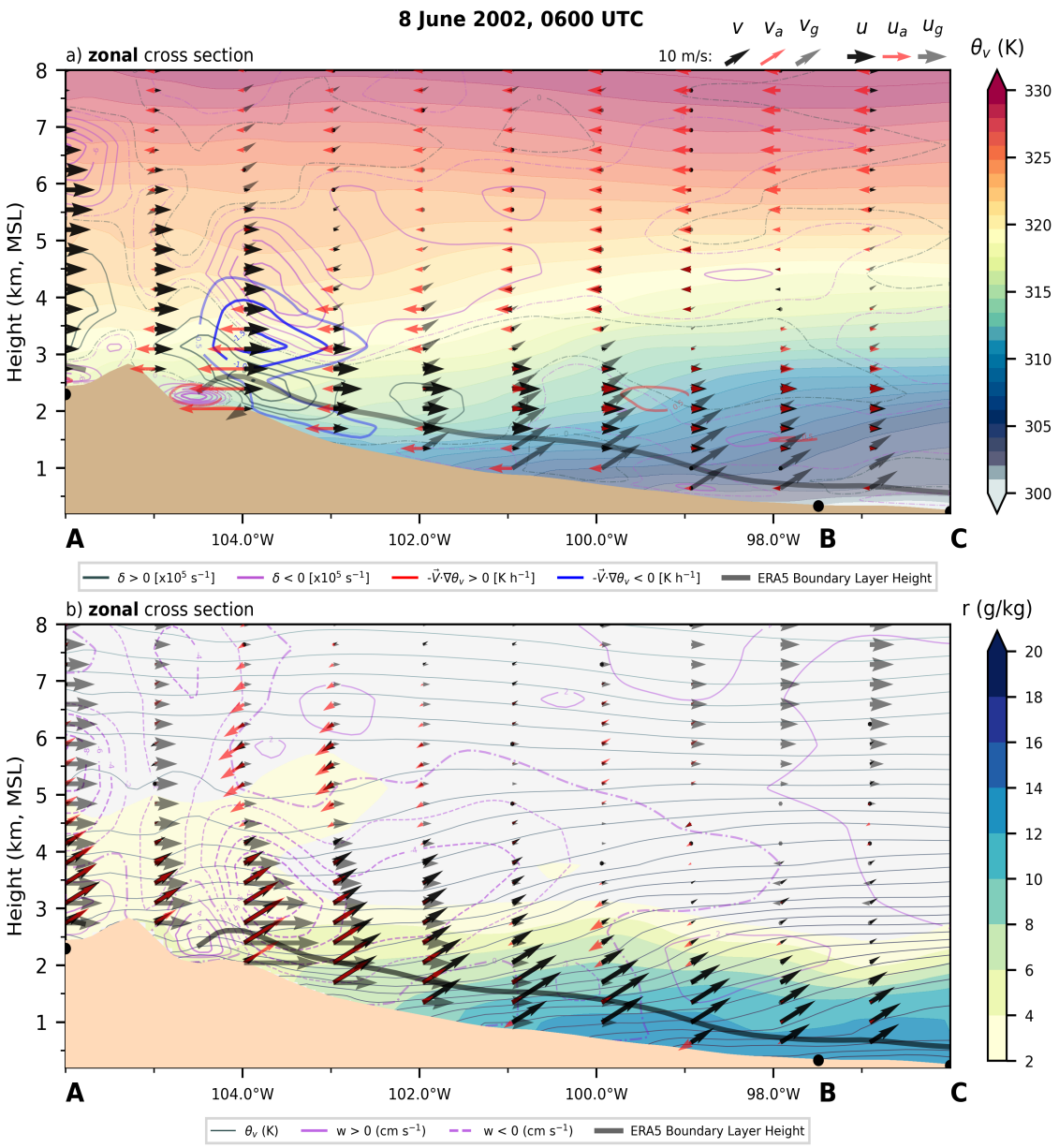

Figure 5.9: As in Figure 5.7 except for 0600 UTC 8 June.

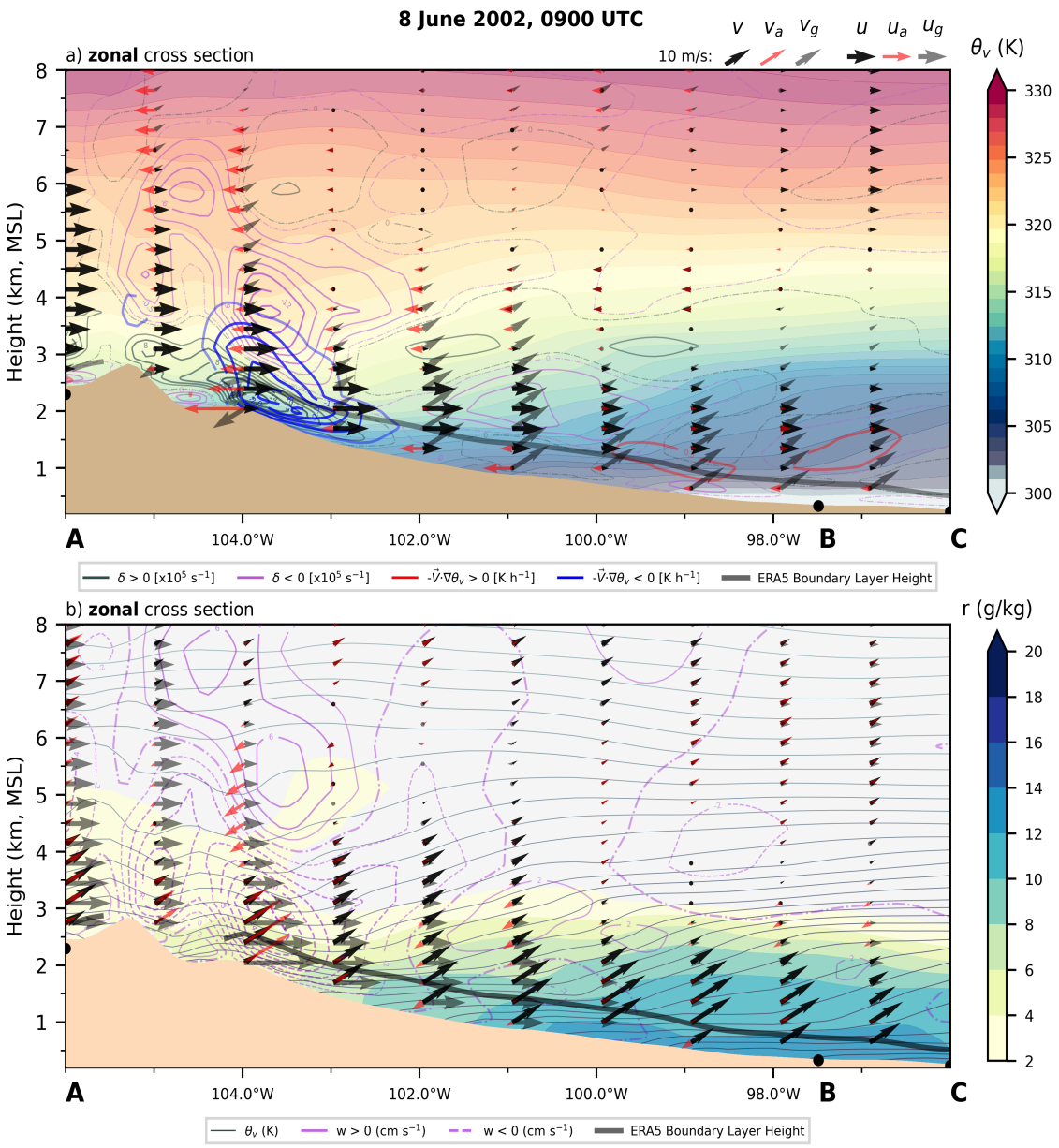

Figure 5.10: As in Figure 5.7 except for 0900 UTC 8 June.

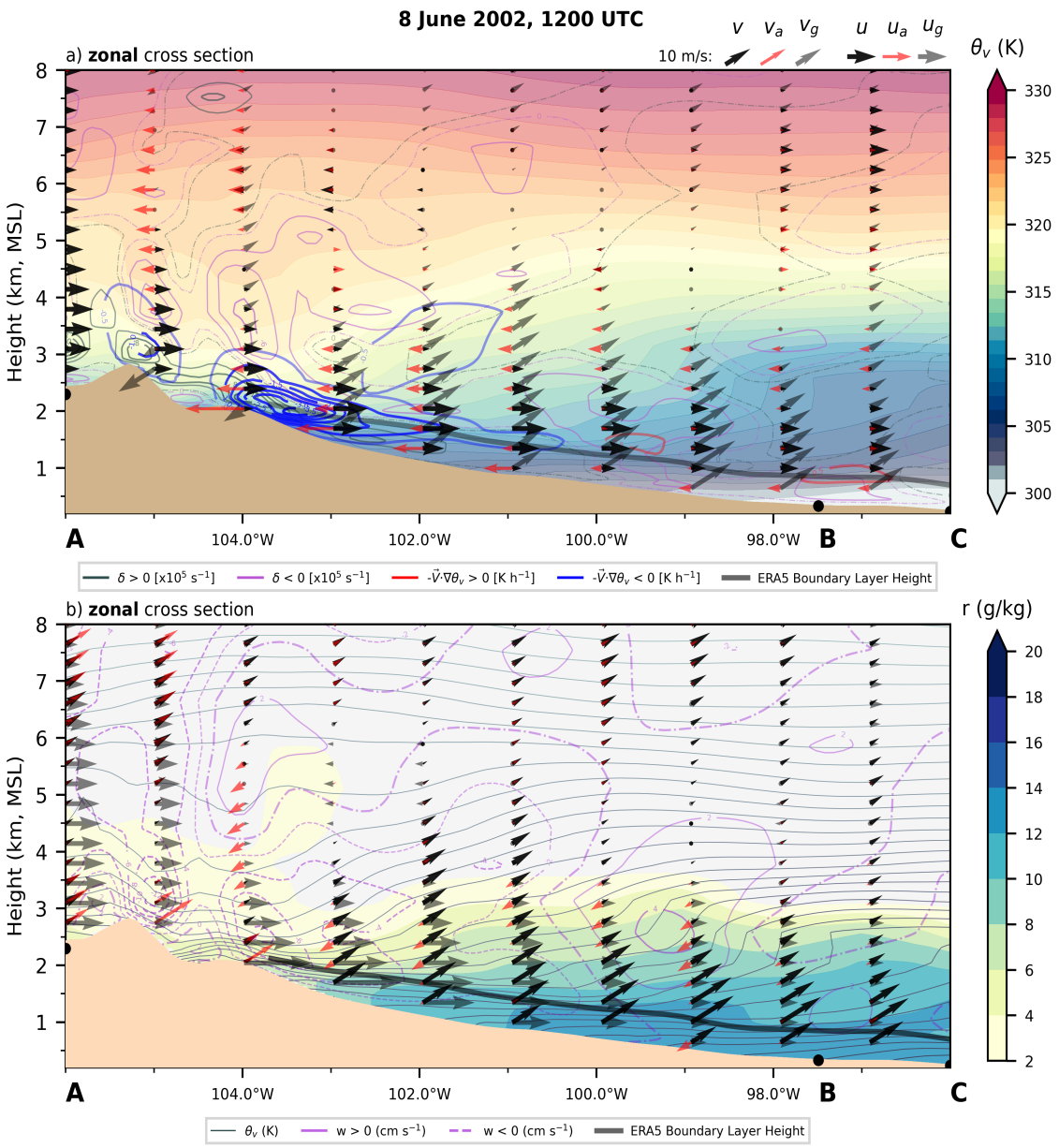

Figure 5.11: As in Figure 5.7 except for 1200 UTC 8 June.

5.4 Evolution of the NLLJ

As shown earlier in Figure 3.4, the magnitude of the southerly NLLJ was category 2 at the central site on 8 June. A pronounced southerly NLLJ developed at all of the ARM sites on 8 June. Rawinsonde data collected from the ARM sites indicates that the southerly NLLJ was characterized by a v_{max} of 10-20 m s^{-1} with 5-10 m s^{-1} of shear above and below the v_{max}. The most intense v_{max} occurred at the western site, and was located at heights of 600-800 m. The NLLJ at this site had intensities of 19 m s^{-1} at 0600 UTC, decreasing slightly to 17 m s^{-1} at 1200 UTC (Fig. 5.12a). In contrast, the eastern site had the weakest southerly NLLJ, which reached a peak intensity of 14 m s^{-1} at 1200 UTC, at a height of 600-800 m. North-south variations were also observed in the southerly NLLJ (Fig. 5.12c,d). A more intense and shallow southerly NLLJ occurred to the north, where it reached peak a strength of 19 m s^{-1} at 0900 UTC at heights of 100-300 m. While to the south a v_{max} of 17 m s^{-1} occurred at 1200 UTC from 500-1000 m, although the v_{max} only increased slightly after 0600 UTC (Fig. 5.12d).

Some spatial variations were the result of the v component undergoing an intensification over a $\sim$1 km deep layer located above the v_{max}. At the central site an intensification of v above the v_{max} took place from 0600 to 0900 UTC, at which time v increased by $\sim$4 m s^{-1} over heights of 1-2 km (Fig. 5.12e). In contrast, at the eastern site, v decreased by $\sim$2 m s^{-1} over heights of 1-2 km (Fig. 5.12b). Meanwhile at the western site, v remained remarkably unchanged below heights of 3.5 km from 0600-0900 UTC (Fig. 5.12a). These findings are consistent with v being influenced by changes to v_g observed in meridional and zonal cross sections. Analysis of zonal cross-sections found that changes to v over deeper layers were associated with the evolution of θ_v gradients at 97-99°W.

Examination of θ_v profiles from the ARM sites reveals cooling consistent with ascent occurred at heights and locations necessary to explain spatial and temporal variations of the thermal wind found in cross sections above the v_{max}. At the central site, cooling of $\sim$4-5 K

coincided with moistening of $\sim$8 g kg^{-1} from 0600-0900 UTC (Figs 5.14e, 5.15e). Horizontal advection temperature and moisture advection accounted for less than half of the cooling and moistening at heights of 2-3 km from 0600-0900 UTC (Fig. 5.18) consistent with changes due to ascent. Rawinsonde derived vertical velocities at the central site confirms that ascent of 2 cm s^{-1} at 0600 UTC occurring at heights of 1-3.5 km (Fig. 5.16a). This ascent was associated with a local maximum of convergence occurring at a height of $\sim$1-1.2 km. Heights where the suspected adiabatic cooling took place are consistent with changes to the thermal wind needed to account for enhancements to v aloft at the central site. Adiabatic cooling from ascent at 97-99°W would result in a northerly thermal wind enhancement since the temperature gradient has become warmer to the west, while the inverse is true at the eastern site. Changes to the thermal wind are evident in meridional cross sections at heights of 2-3 km, here the thermal wind became more northerly by $\sim$5 m s^{-1} km^{-1}, going from $\sim$-5 m s^{-1} km^{-1} to $\sim$0 m s^{-1} km^{-1} near the central site in 0600-0900 UTC (Fig. 5.6a,b). These findings support convergence as an underlying process leading to elevated geostrophic enhancements of v at the central site.

Spatial and temporal variations in v from 0600-0900 UTC were associated with convergence occurring at heights of 1.2-1.4 km at the central site (Fig 5.16b), this coinciding with lower portions of the westerly NLLJ (Fig 5.13e). Zonal variations in the height and intensity of the westerly NLLJ are consistent with contributing to convergence at the central site, with the western site having a relatively lower and more intense u_{max} compared to the eastern site at 0600 UTC (Fig 5.13a,b). These differences in the westerly NLLJ occurred at heights of 1.4-2.7 km MSL at the western site versus 2-2.2 km MSL at the eastern site with u_{max} values of $\sim$7 m s^{-1} at the western site versus $\sim$5 m s^{-1} at the eastern site (Fig 5.13a,b). A correlation in heights of the u_{max} and cooling should be evident in the northern and southern sites if convergence associated with the westerly NLLJ is contributing to ascent, this was indeed the case (Figs 5.14c,d and 5.13c,d). The northern site had the lowest u_{max} compared to the other sites at 0600 UTC, with a height of $\sim$1 km (Fig. 5.13c),

directly above was a ∼500 m deep layer of cooling by 2-4 K (Fig. 5.14c). In contrast, the southern site had the most elevated u_{max} at 0600 UTC (Fig. 5.13d), which also coincided with a layer of cooling directly above (Fig. 5.14d). These north-south variations in cooling are consistent with analysis of meridional cross sections which indicated a more northerly thermal wind enhancement occurred south of 37.5°N from 0600-0900 UTC, this analysis also found that moistening was associated with the advection of moisture over a deep layer, rather than being confined to heights near the v_{max}. Rawinsonde derived profiles of moisture advection at the central site confirms that indicates moisture advection of ∼0.5 g kg^{-1} was occurring at heights of 2-3 km. This moisture advection was similar in magnitude to that occurring at the height of the v_{max}, except over a 1 km deep layer compared to a <100 m deep layer for the v_{max} (Fig. 5.18c). These results suggest that enhancements to v occurring above the v_{max} should be considered when examining moisture transport by the southerly NLLJ. Convergence associated with a heterogeneous u_{max} may offer an explanation for some characteristics of the southerly NLLJ through its impacts on θ_v gradients. However, this raises the question of what process(es) are driving this heterogeneous u_{max}. One suggestion offered earlier was the combined thermal wind reversal and IO mechanism from the Shapiro et al. (2016) analytical study. Previous analysis of meridional cross sections found some variations in v_g were consistent with being associated with a barotropic pressure perturbation, this observation may point to an alternative explanation for the heterogeneous behaviour of the u_{max}. Vertical profiles of the PGF constructed from rawinsonde data at the ARM sites indicates that pressure perturbations did indeed occur when calculated over half the domain (∼150 km) (Fig. 5.17a,c), however these variations are smoothed out when the full domain is used to calculate the gradients (Fig. 5.17a,c). Westerly acceleration resulting from this enhancement to the PGF can be calculated using the PGF term in the momentum equation:

$$\frac{\partial u}{\partial t}_{PGF} = \frac{-1}{\rho}\frac{\partial P}{\partial x} \tag{5.1}$$

where ρ is the density of air and $\frac{\partial P}{\partial x}$ is the x component of the PGF. A rough calculation is performed to determine the order of magnitude of acceleration produced by changes in the PGF between the western and central sites at heights of $\sim$2 km MSL from 0000-0600 UTC. This calculation estimates ρ as 1 kg m^{-3} and $\frac{\partial P}{\partial x}$ as 5x10^{-4} Pa m^{-1}. Using these values the calculation yields an acceleration with magnitudes of 5x10^{-4} m s^{-2}. Over a 6 h period this would result in a enhancement with magnitudes of $\sim$11 m s^{-1}. Although other terms in the momentum equation would also be acting on the winds, this acceleration the order of magnitude needed to account for evolution of the westerly flow associated with convergence (Fig. 5.13a,e). Meanwhile between the central and eastern sites the opposite change in the PGF occurred, where it decreased by $\sim$5 hPa (1000 km)$^{-1}$. These spatial variations in the PGF are consistent with producing convergence at heights of the u_{max} over the central site. One possible explanation for this spatial variation in the PGF could be divergence associated with low-level upslope flow that develops as mixing ceases in the deeper PBL to the west and an IO acts on the low-level v_g to the east, as was proposed earlier as a possible mechanism for explaining a similar pressure perturbation on 7 June.

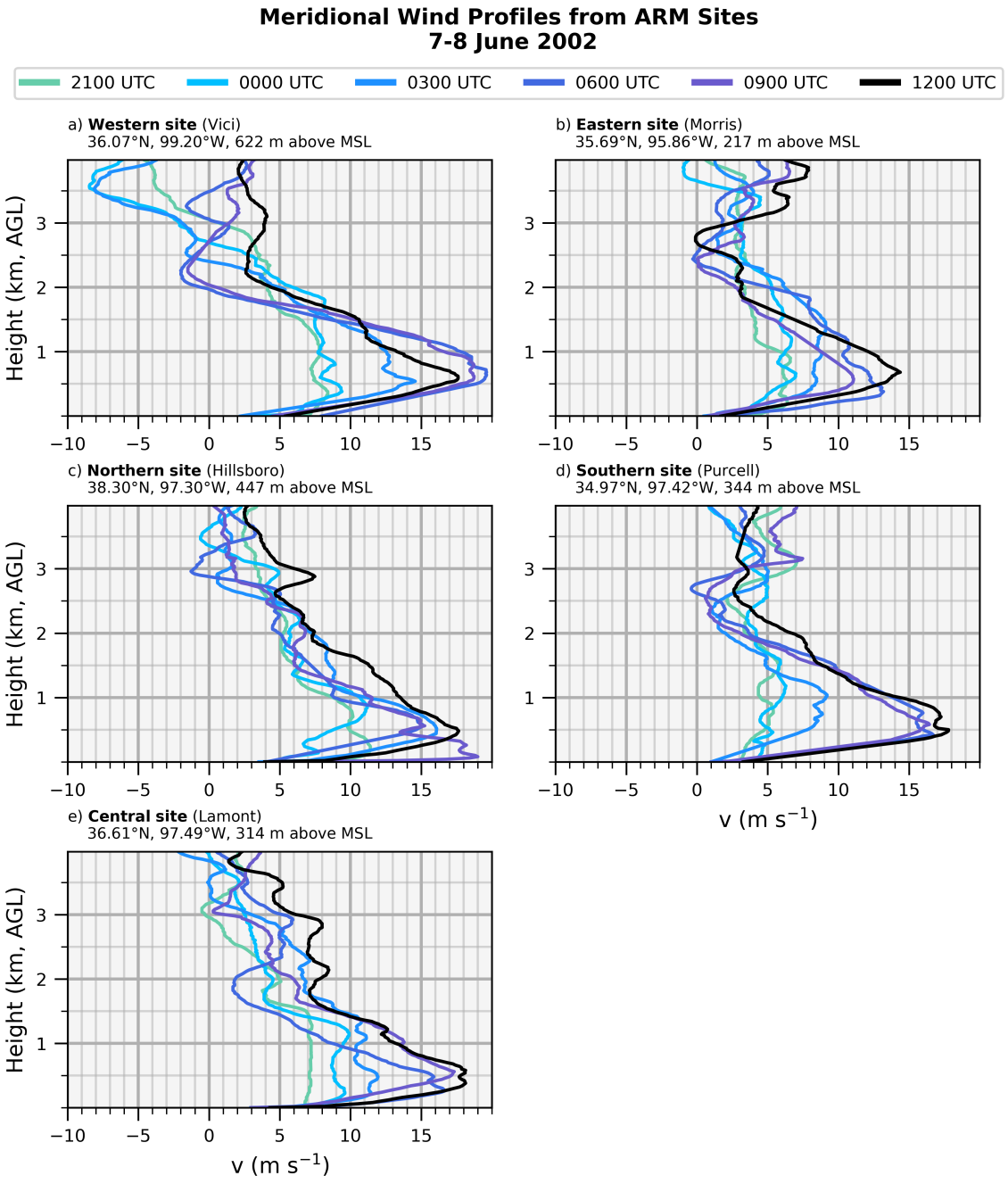

Figure 5.12: As in Fig. 4.6 except for 7-8 June 2002.

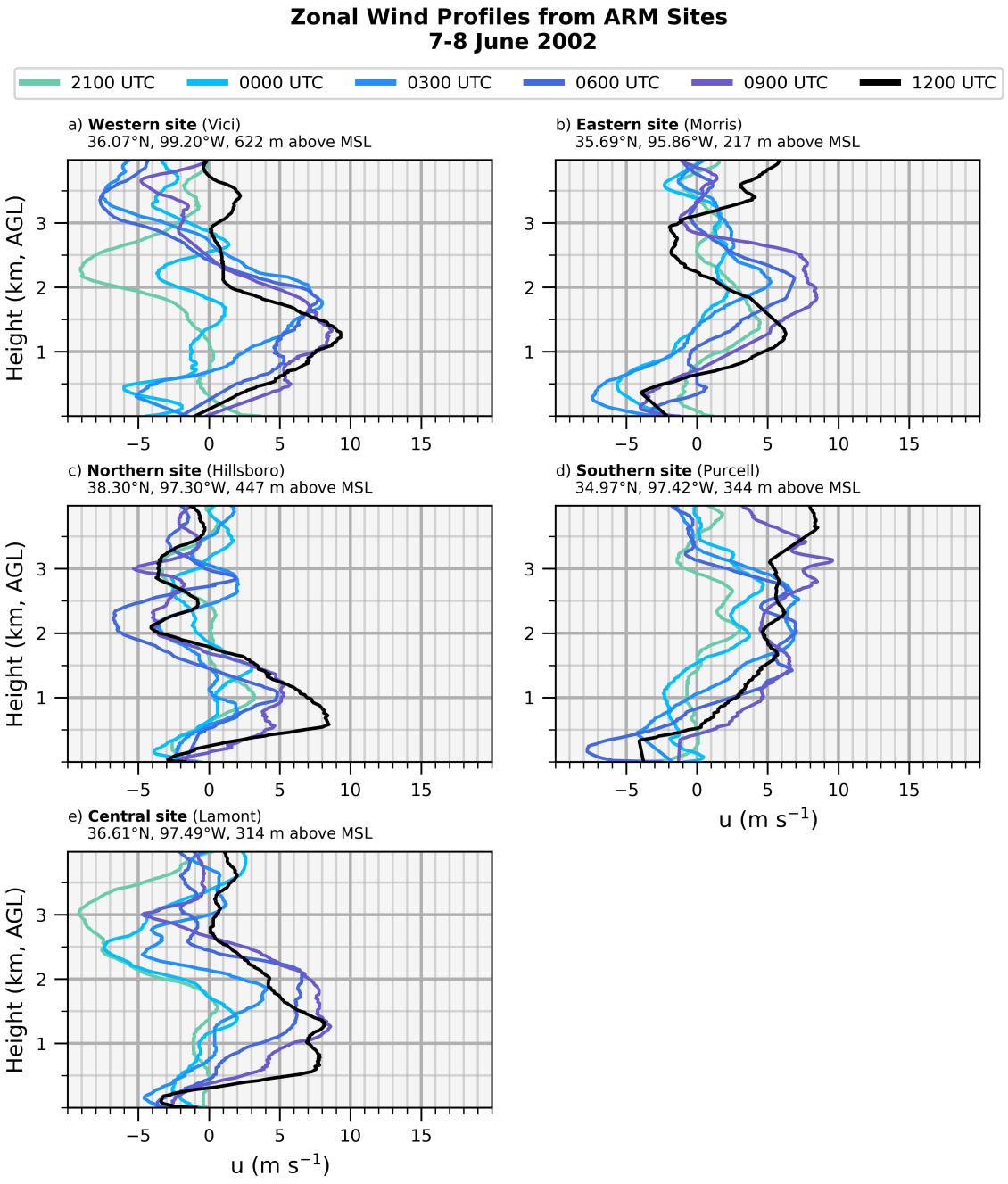

Figure 5.13: As in Fig. 4.9 except for 7-8 June 2002.

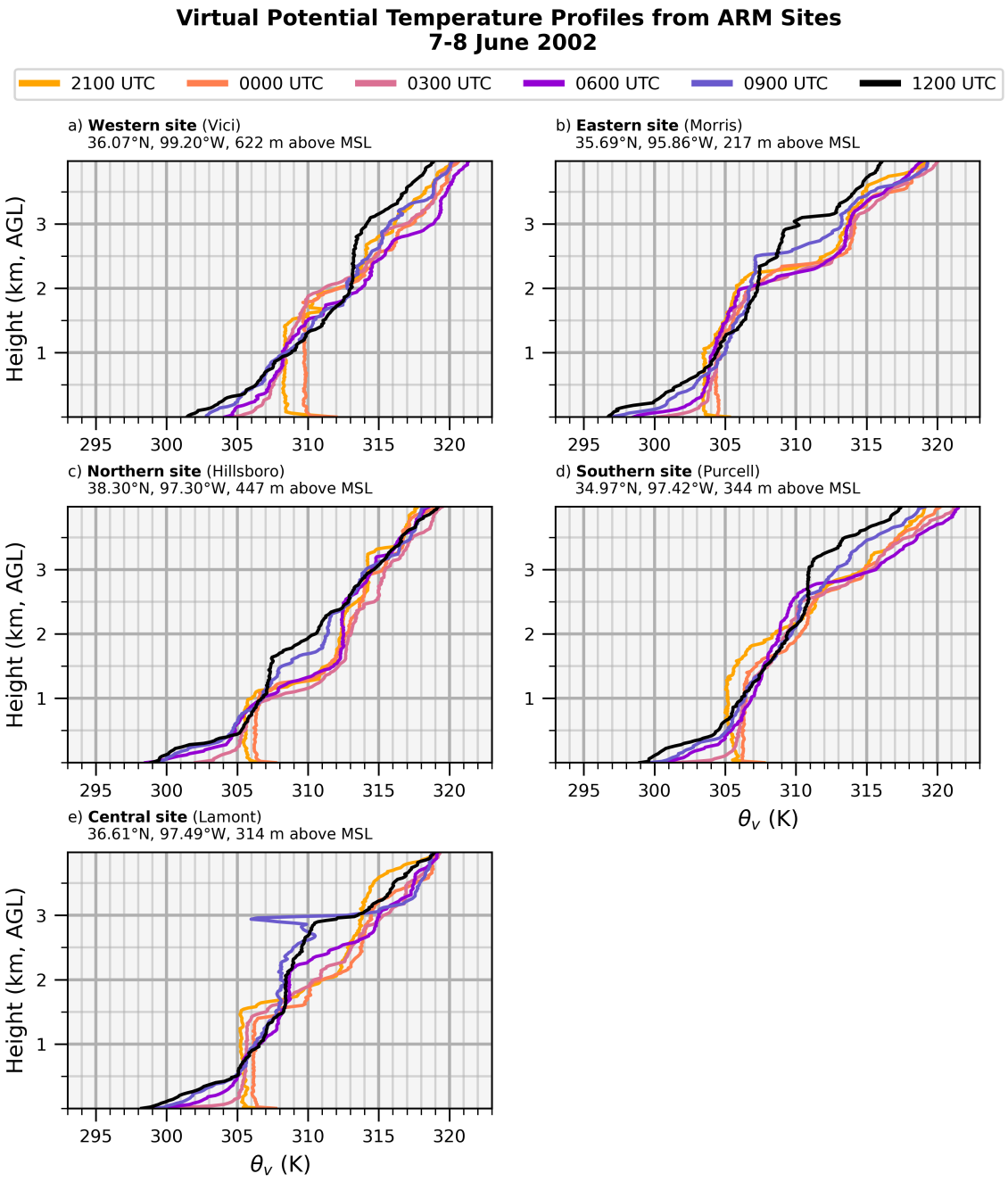

Figure 5.14: As in Fig. 4.10 except for 7-8 June 2002.

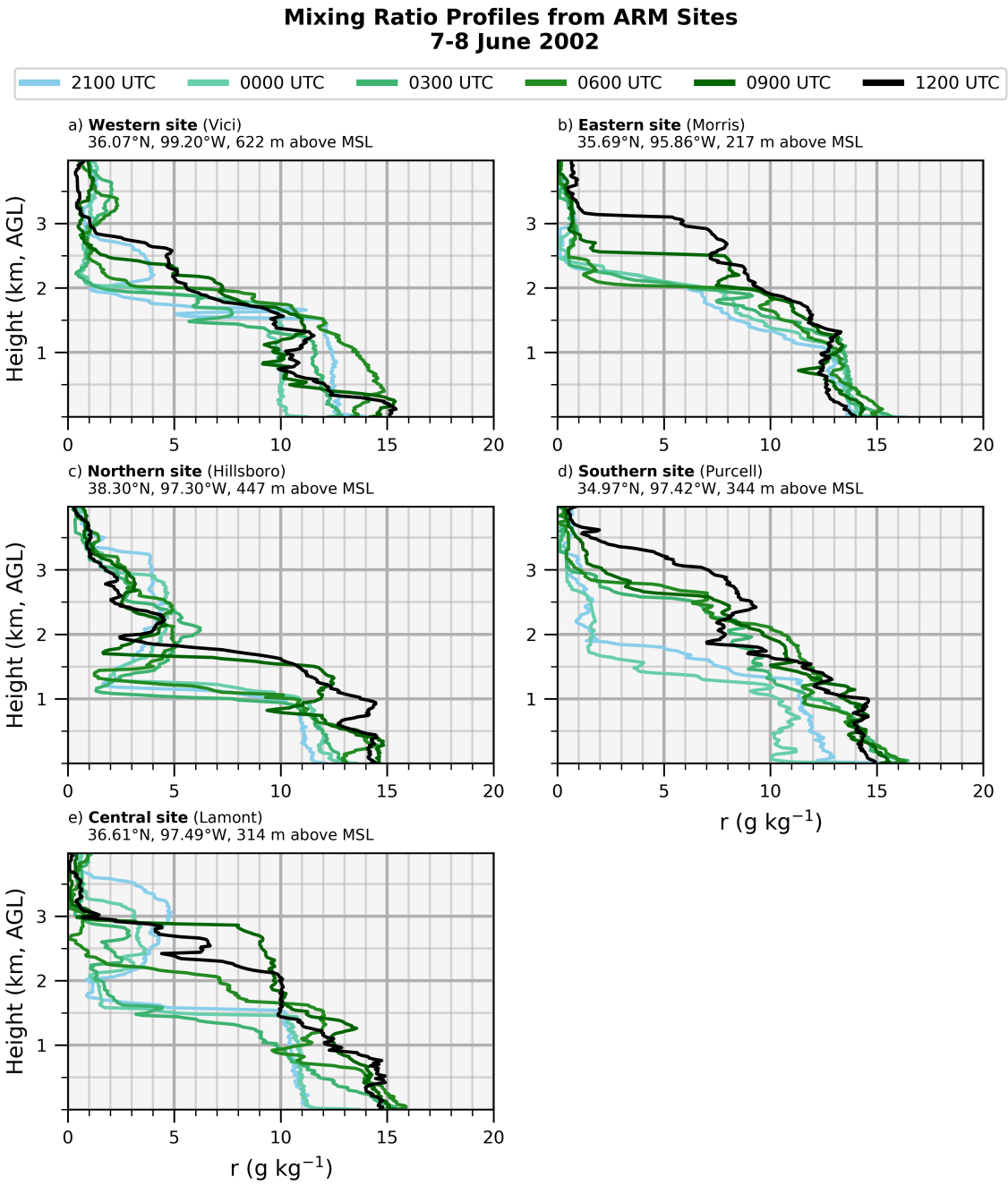

Figure 5.15: As in Fig. 4.7 except for 7-8 June 2002.

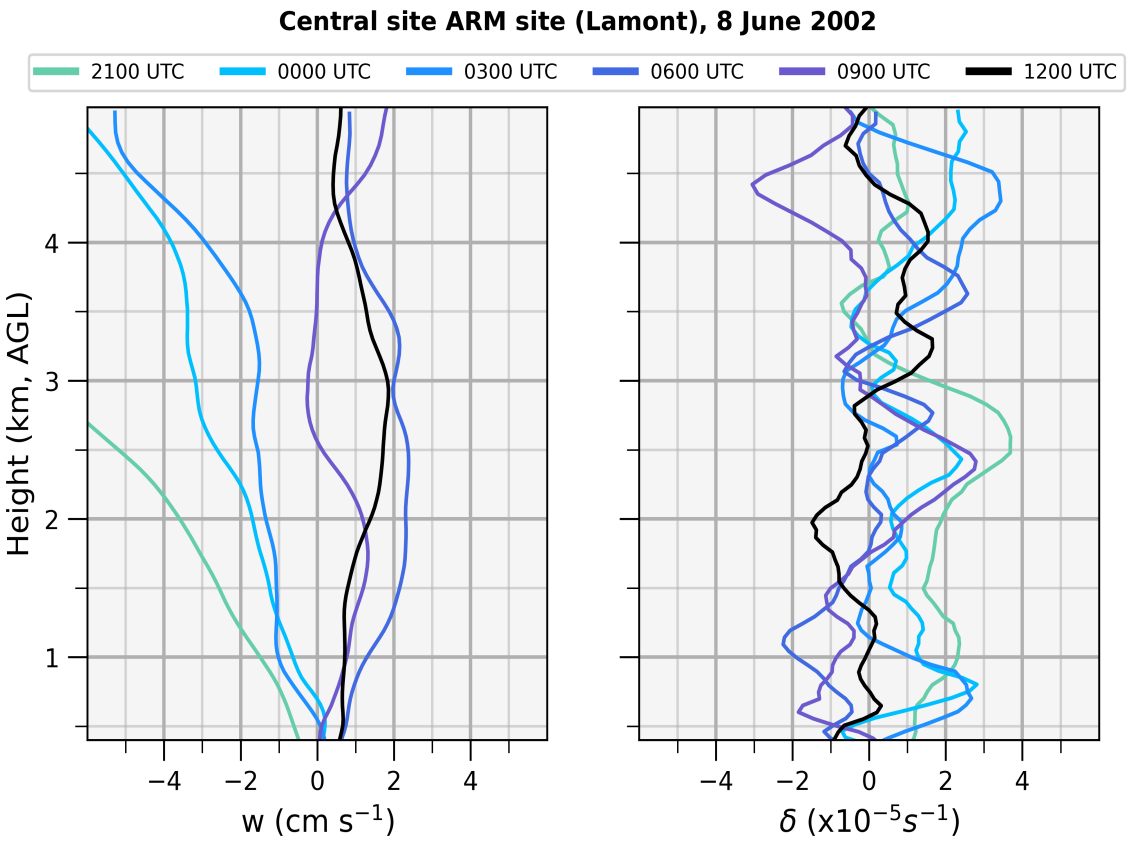

Figure 5.16: As in Fig. 4.12 except for 7-8 June 2002.

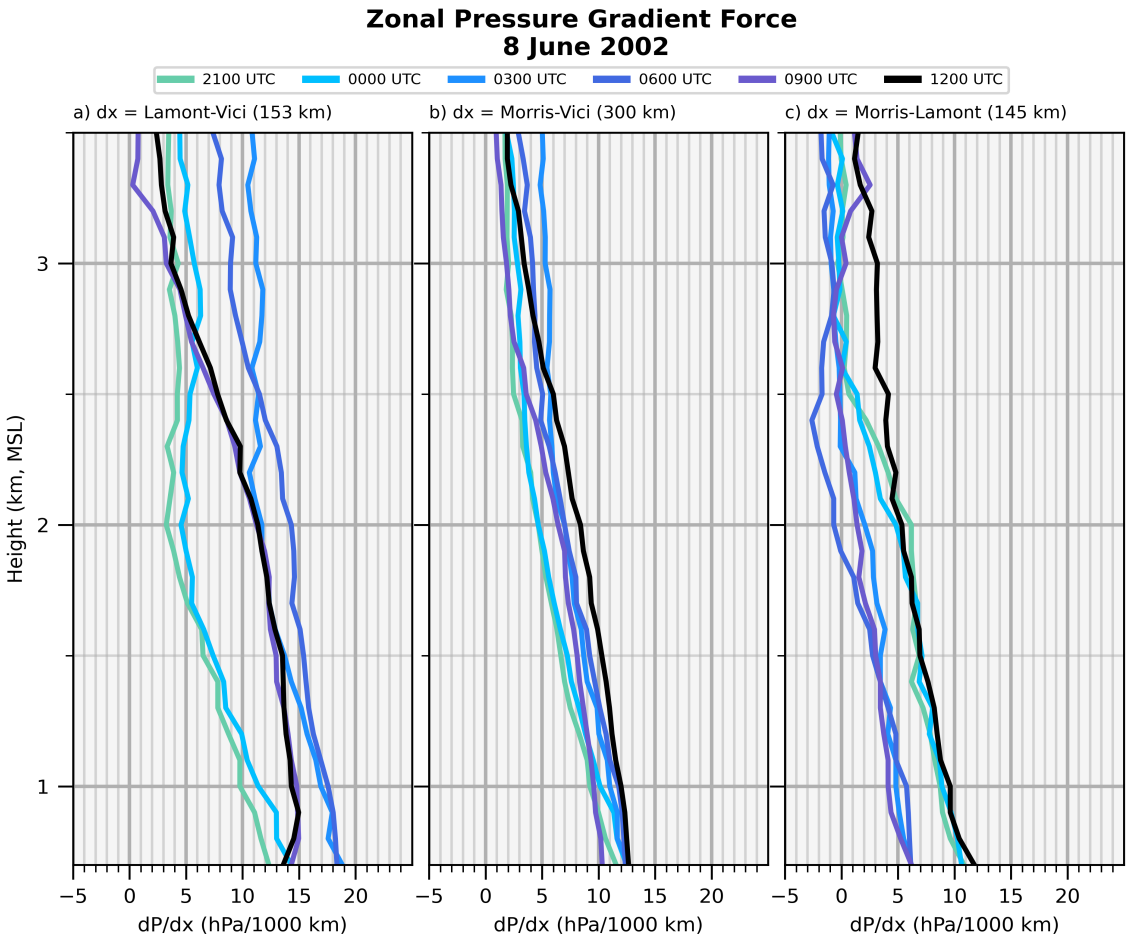

Figure 5.17: As in Fig. 4.11 except for 2100-1200 UTC 7-8 June 2002.

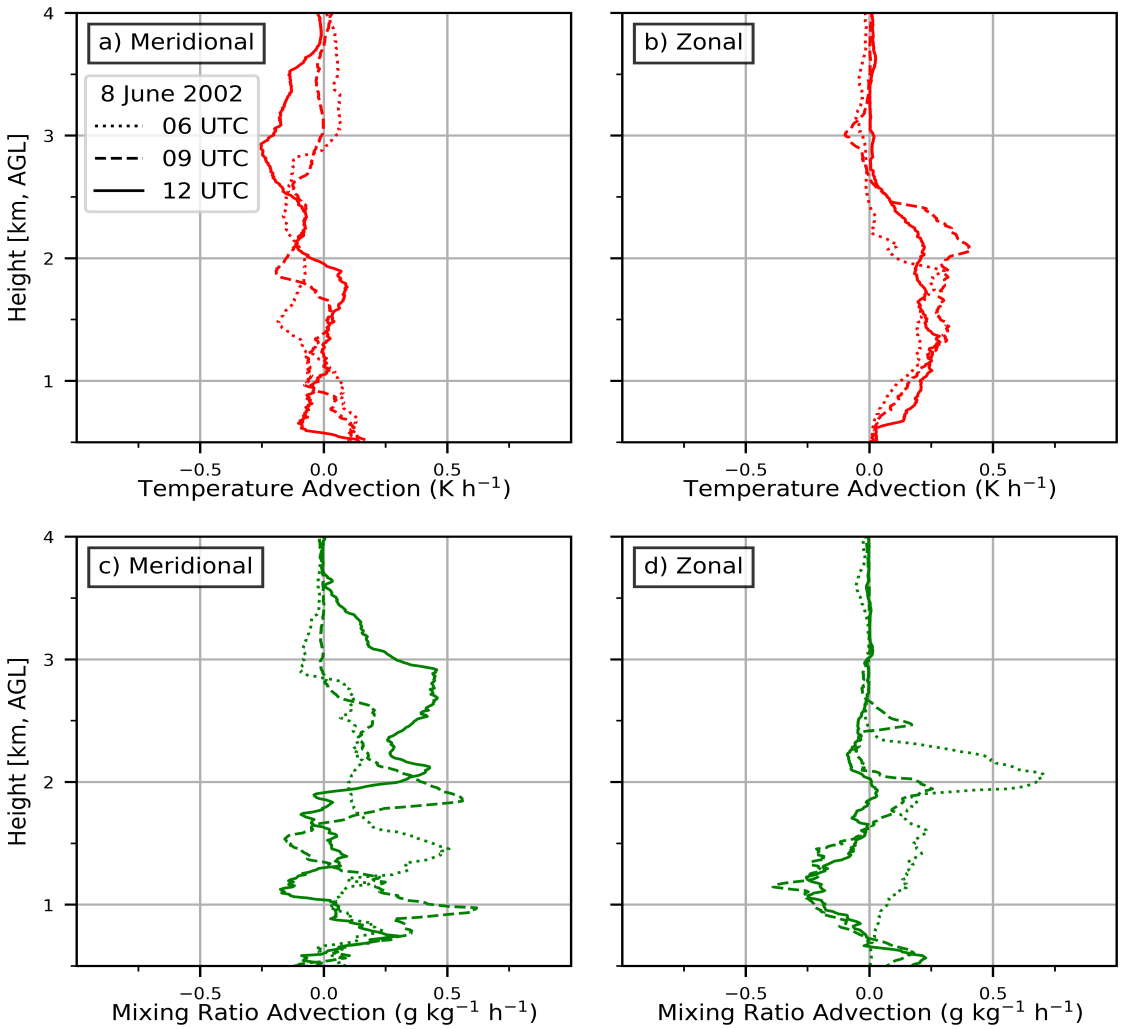

Figure 5.18: Vertical profiles at the central site of a) meridional temperature advection, b) zonal temperature advection, c) meridional moisture advection and c) zonal moisture advection for 8 June 2002 at times: 0600 UTC (dotted line), 0900 UTC (dashed line) and 1200 UTC (solid line). Gradients were calculated using rawinsonde data.

5.5 Evolution of Convective Destabilization

Profiles of CAPE and CIN during the overnight hours at the ARM sites reveal conditions became more favorable for convection at night than during the daytime, with a north-eastward spatial-temporal trend (Figs. 5.19, 5.20). At the western site at heights of 0.5-1 km, CAPE increased by $\sim$2000 J kg^{-1} from 0000-0600 UTC (Fig. 5.19a), skew-T diagrams reveal that this enhancement was the result of low-level moisture (Fig. 5.21a). Enhancements to CAPE at the western site vanished 3 h later at heights of $\sim$0.5-1.2 km (Fig. 5.19a), in association with a decrease in moisture at heights were moistening took place from earlier (Fig. 5.22a). While to the east, CAPE increased by up to $\sim$2000 J kg^{-1} from 0600-1200 UTC at heights of 0.5-1 km (Fig. 5.19c,e), owing to increases in magnitude and depth of moisture below 800 hPa, along with cooling from 800-700 hPa (Fig. 5.22a,b,d). This eastward trend in destabilization suggests moisture was being advected east by the westerly NLLJ, resulting in moistening to the east and drying to the west, this is supported by profiles of rawinsonde derived mixing ratio advection which indicates a spike in zonal advection characterized by $\sim$0.6 g kg $^{-1}$ near a height of 2 km, followed by a spike of negative advection near heights of 1 km in the subsequent hours (Fig. 5.18d).

Evolution of CAPE and CIN at the ARM sites on 8 June was closely associated to low-level moisture (Figs. 5.19, 5.20). Mixing ratio profiles constructed from rawinsonde data from the ARM sites reveal spatial and temporal variations occurred overnight on 8 June. Moistening occurred at two levels at the ARM sites, the lower level moistening took place at heights below 1 km, while as previously mentioned, moistening occurred at levels where ascent took place. Variations in mixing ratio at the ARM sites was characterized by moisture at the western site increasing at heights below 1 km by $\sim$3-4 g kg^{-1} in the first 6 h after sunset (0000-0600 UTC), followed by a decrease of similar magnitude in subsequent hours (Fig. 5.15a). Although moistening took place at the two sites, the evolution of low-level moisture differed, with the southern site moistening over a deeper layer, while at the western site the depth of low-level moisture did not increase but rather moistening only

took place at low-levels. More specifically, at the southern site, dewpoints increased within the moist layer and also 100 hPa above, from ∼800 hPa at 0000 UTC to ∼700 hPa at 0600 UTC (Fig. 5.21a), this deepening of moisture 6 h later was not observed at any of the other ARM sites (Fig. 5.21b,c,d). This finding of deeper moisture occurring at the southern site first is consistent with analysis of meridional cross sections, which suggest the northward advection of deeper moisture from the south associated with an enhancement to v_g (Section 5.6). While examination of skew-T's from the western site reveals the depth of low-level moisture did not change from 0000 to 0600 UTC, dewpoints increased by 2-4°C within heights of the daytime PBL, suggesting that low-level moistening was the primary driver of destabilization here (Fig. 5.21c).

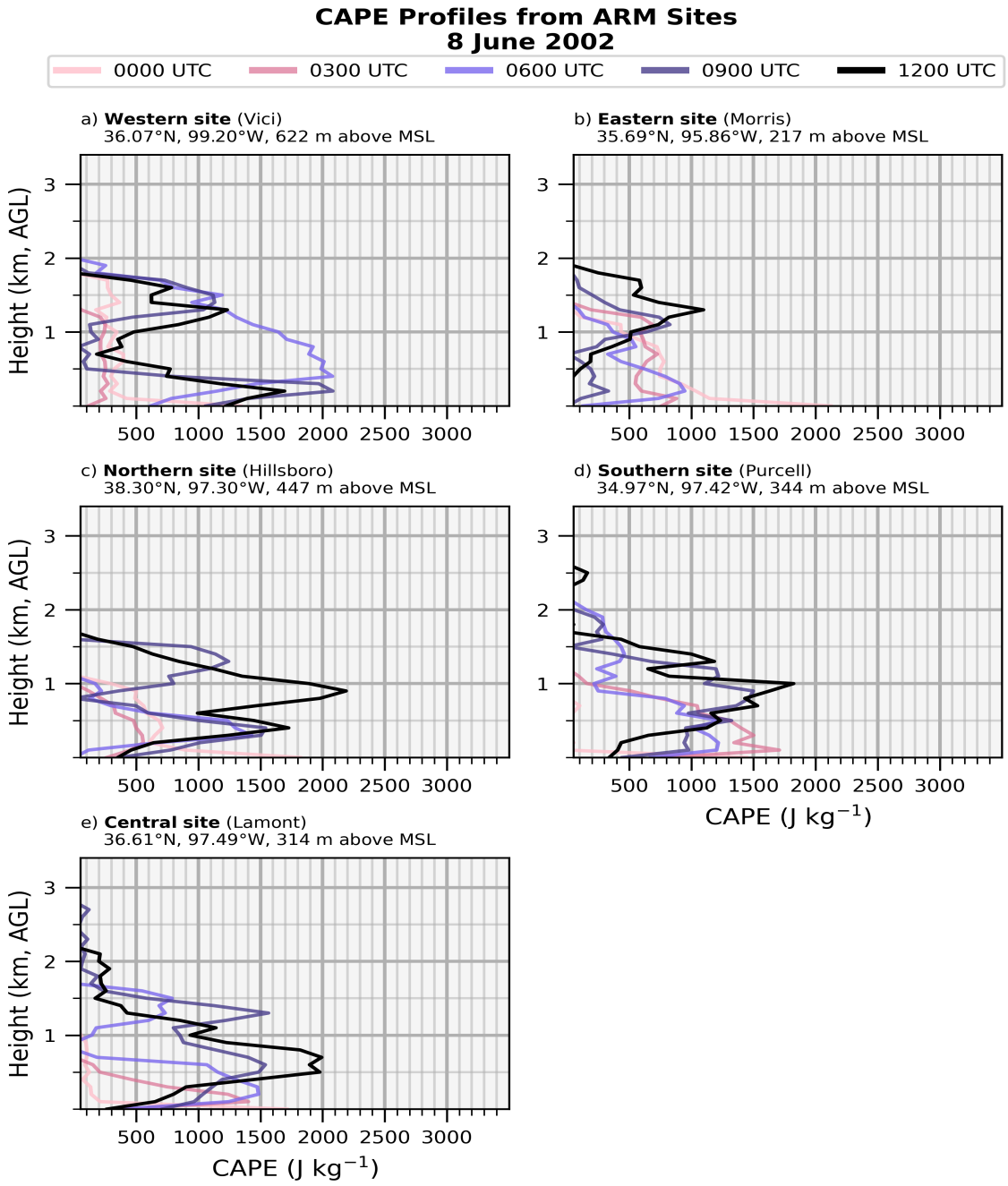

Figure 5.19: Profiles of CAPE as a function of height from 0000-1200 UTC 8 June 2002 taken from sounding data collected from the 5 ARM sounding sites: a) western site (Vici), b) eastern site (Morris), c) northern site (Hillsboro), d) southern site (Purcell), and e) central site (Lamont).

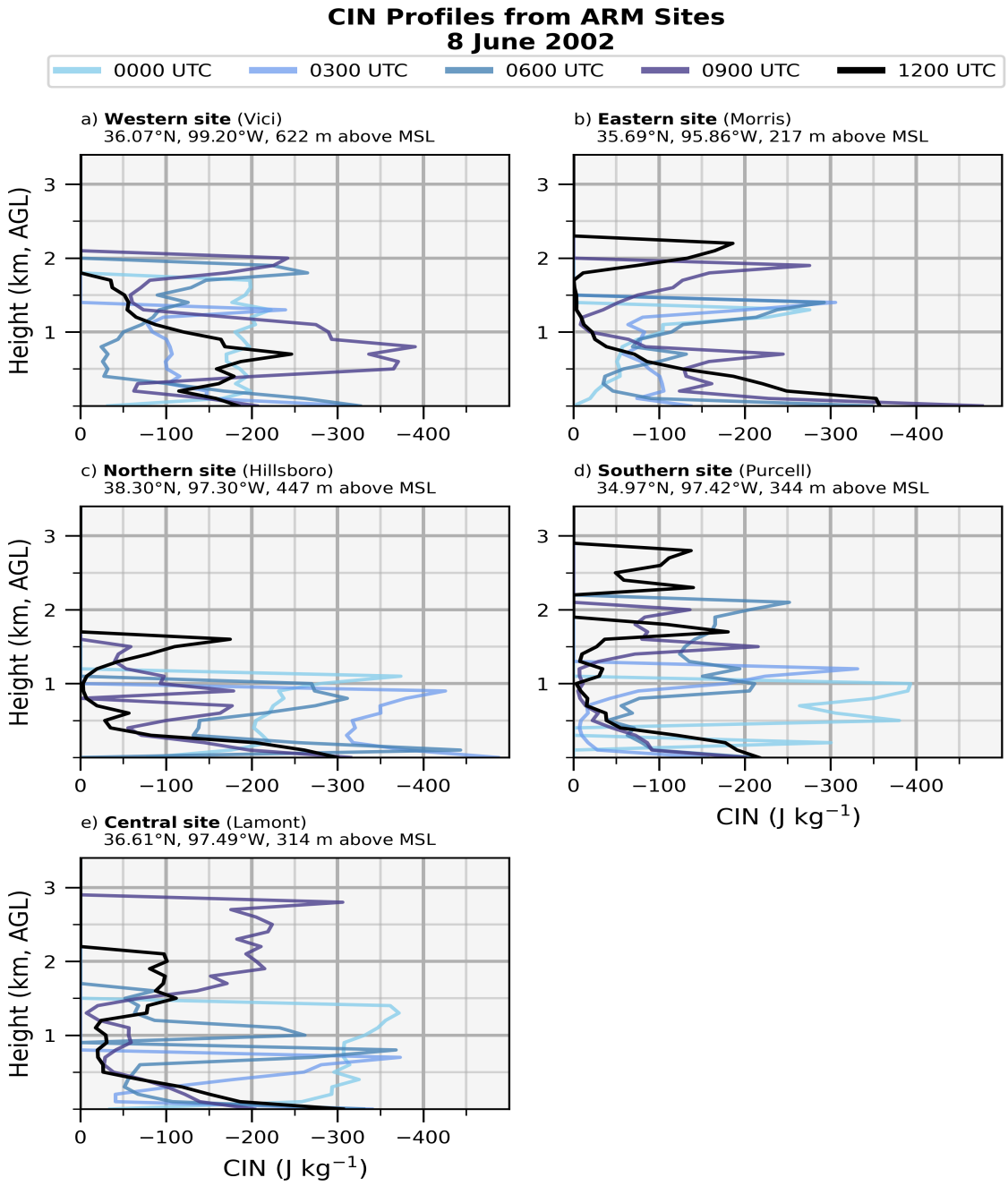

Figure 5.20: Profiles of CIN as a function of height from 0000-1200 UTC 8 June 2002 taken from sounding data collected from the 5 ARM sounding sites: a) western site (Vici), b) eastern site (Morris), c) northern site (Hillsboro), d) southern site (Purcell), and e) central site (Lamont).

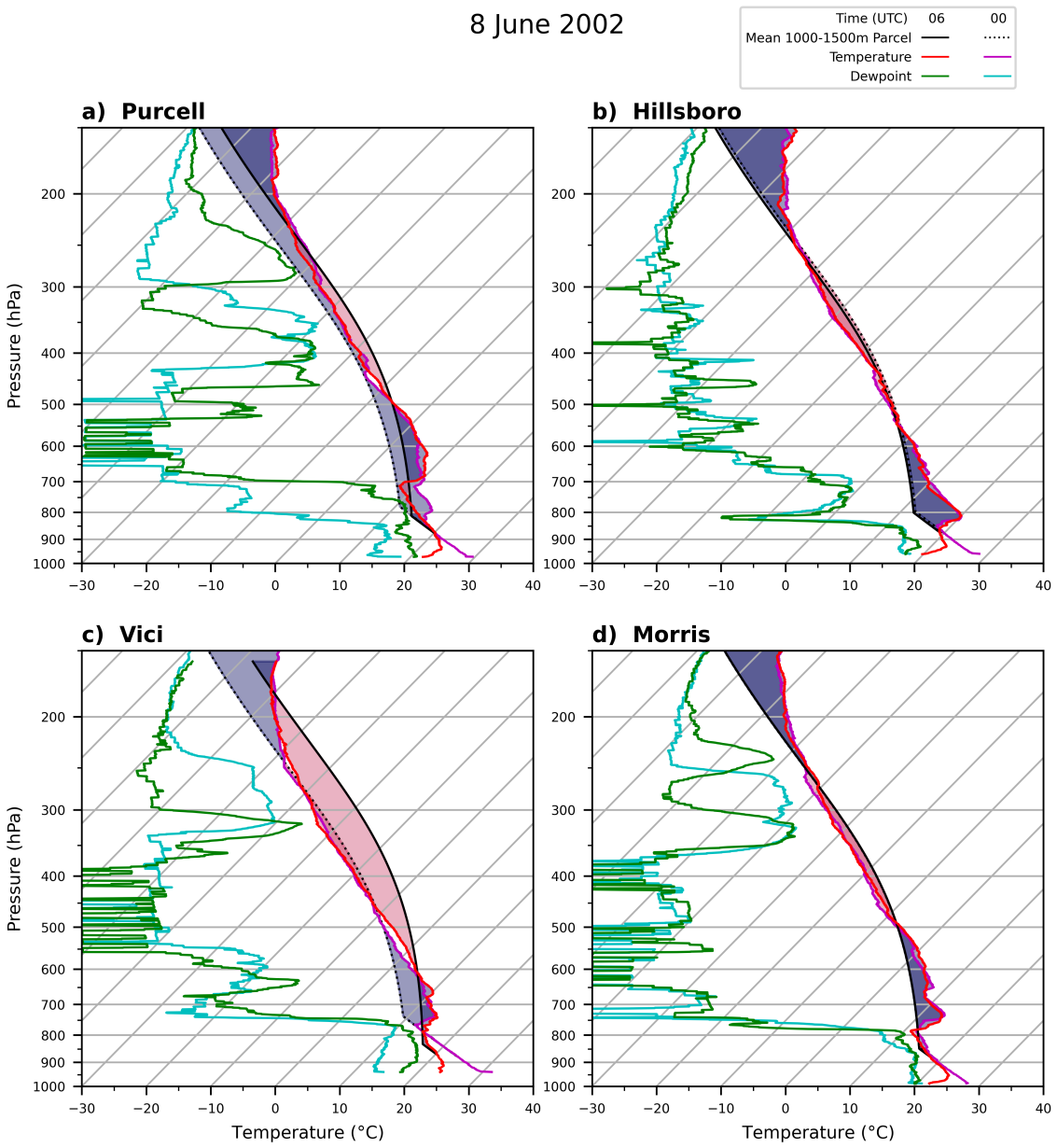

Figure 5.21: Comparison of 0000 and 0600 UTC skew-T profiles on 8 June 2002 constructed from sounding data taken from ARM sites: a) Purcell, b) Hillsboro, c) Vici, d) Morris.

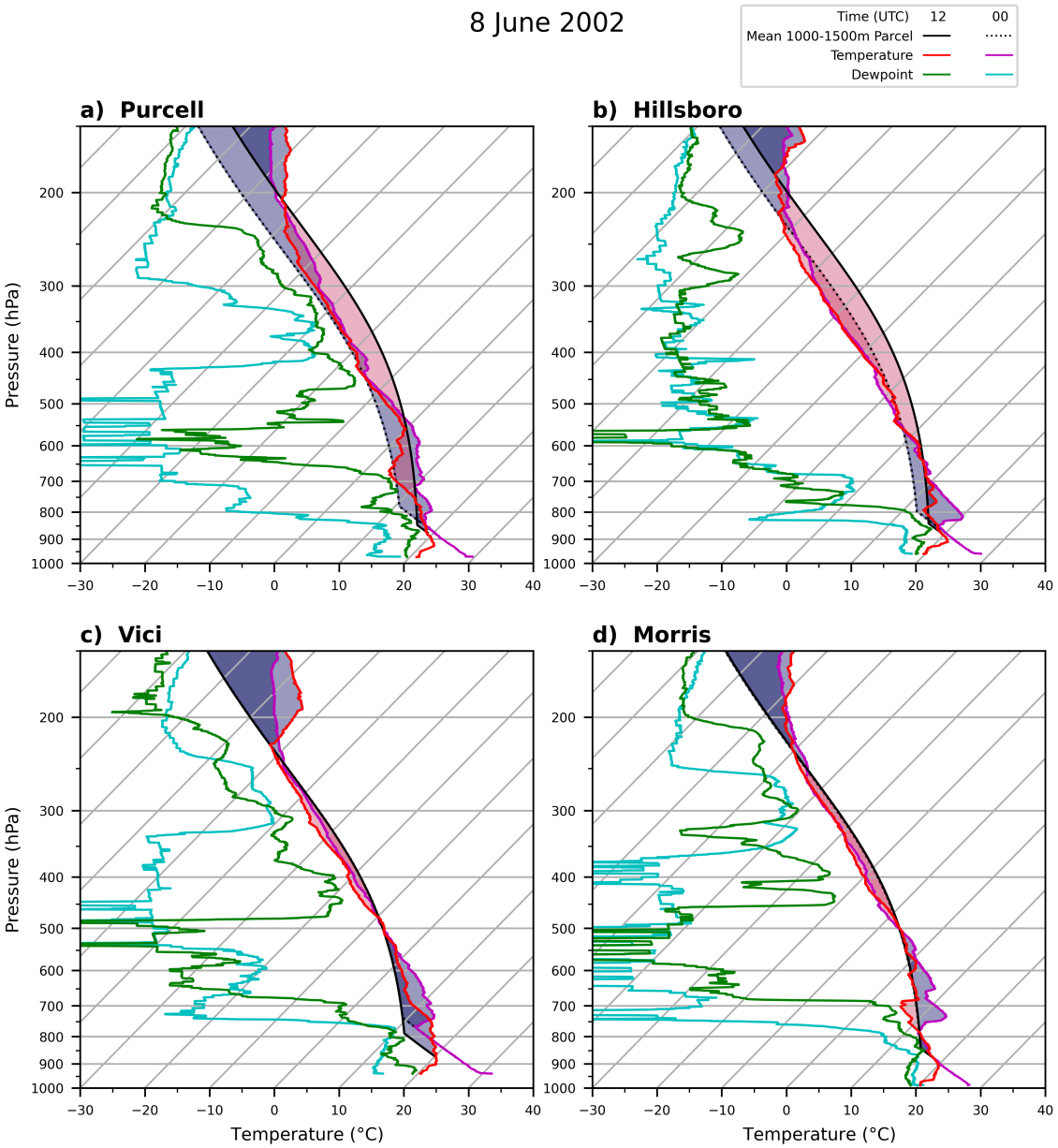

Figure 5.22: As in Figure 5.21 except comparing times 0000 and 1200 UTC.

5.6 Discussion

The southerly NLLJ that developed on 8 June occurred with maximum intensity near a surface low located in eastern Colorado. This surface low was associated with a baroclinic zone and gradient in PBL heights along the slope. Parish (2016) proposed that such an environment is favorable for the development of strong southerly NLLJs owing to an IO acting on the daytime v_g associated with the baroclinic zone. Some aspects of NLLJ evolution resembled NLLJs produced by the Shapiro et al. (2016) analytical model, including a westerly u_{max} that descended with time. However, these mechanisms could not offer a complete explanation for certain aspects of the evolution of the southerly NLLJ. Analysis of vertical cross sections found that a deep southerly enhancement with magnitudes of $\sim$5 m s^{-1} appeared to be geostrophic. Variations in the zonal PGF from the ARM sites were consistent with changes to v_g observed in cross sections, occurring on scales of $\sim$150 km. As expected, the southerly NLLJ was found to play an important role in returning moisture to the region after the frontal passage on 5 June. The most intense period of moisture convergence during the second recovery period occurred on 8 June. This finding suggests that processes driving NLLJ evolution are vital for moisture transport into the continental United States. Moisture transport associated with this jet was found to occur over a deep layer and was not confined to the narrow layer of the v_{max}.

Variations of $v_g(z)$ were tied to changes in θ_v gradients aloft and heterogeneous PBL depths, similar to previous studies by Gebauer et al. (2018) and Smith et al. (2019). However, in this case perturbations in the PGF that appear to be driving this evolution. These variations in the PGF appeared to be barotropic in nature as changes were relatively uniform with height. This finding has not been documented in previous work and suggests a more complex relation between heterogeneous PBLs and NLLJ evolution than proposed by past studies. It was found these variations also contributed to a heterogeneous u_{max} resulting convergence and ascent as it propagated east. Therefore impacts of ascent to the

θ_v gradient on NLLJ evolution were secondary effects of this pressure perturbation, as the primary effects were the uniform intensification of southerly flow.

Results presented in this chapter suggest that gradients in PBL characteristics played a dominant role in evolution of low-level flow and creating a more favorable environment for convection. Analysis of the prior date indicated that similar PBL gradients produced similar variations in the PGF when decoupling resulted in differences in evolution of the flow between the two PBLs. Given similarities in evolution of the southerly NLLJ between the two dates, it is speculated that a similar process occurred on this date.

Chapter 6

Post-Moisture Return

This chapter examines NLLJ evolution on 10 June 2002, which took place in a more active synoptic environment than the previous two cases. This chapter will examine how the NLLJ may have contributed to creating an environment more favorable for convection. Examining destabilization on 10 June may provide additional insight into how the NLLJ facilitates convection since it was noted earlier that moisture flux into the region following the 5 June frontal passage has diminished by this time. This chapter will follow a similar organization to Chapter 5.

6.1 Synoptic Conditions

A 500 hPa trough was located west of Colorado on 10 June at 2100 UTC (Fig. 6.1). At this time the strongest 500 hPa flow (> 35 m s^{-1}) was located over Utah, Wyoming and southern Montana. This synoptic pattern differs to that which occurred for heterogeneous NLLJs during PECAN which was characterized by a ridge over the Rocky Mountains and a trough over the eastern US (Gebauer et al. 2018). The trough located west of the Rockies is in a similar location to so-called coupled low-level jets documented by Uccellini (1980). Although mid-level flow is weak in the vicinity of the ARM sites, since the trough is located downstream this is typically described as an active synoptic environment by previous studies (Walters 2001; Wang and Chen 2009; Burrows et al. 2020).

Examining surface ERA5 reanalysis data reveals an area of intense surface moisture and θ_v gradients indicative of a dryline was located along the Kansas-Colorado border and extended south into the Texas Panhandle during the daytime hours (Fig. 6.2). Consistent with a dryline, confluent winds straddled the baroclinic zone created by the thermal gradients, surface winds were characterized by values of $\sim$10 m s^{-1} over this region. This

wind field appears to be contributing to a large moisture gradient characterized by surface mixing ratios going from $\sim$16 g kg^{-1} in the central Texas Panhandle decreasing to 6 g kg^{-1} along the Texas/New Mexico border. Such a moisture gradient is sufficient to meet dryline criteria (Schaefer 1974b). Isobars indicate that a surface low was located in northeastern Colorado, in a similar location to the two previous cases analyzed. One difference compared to the two prior dates is a more meridional orientation and tighter spacing of isobars, the more intense PGF is particularly evident in the Oklahoma/Texas Panhandle. ERA5 PBL heights indicate that a sharp gradient is associated with the dryline, where the depth of the boundary layer goes from $\sim$2000 m in the central Oklahoma/Texas Panhandle to $\sim$4000 m near the New Mexico border (Fig. 6.3). This gradient in PBL heights is shifted closer to the ARM sites compared to 7 and 8 June, where it was located in central Colorado.

The v_{max} from ERA5 data indicates that an intense southerly NLLJ developed, with speeds in excess of $\sim$30 m s^{-1} at heights of 800-1000 m (Fig. 6.4). The core of the southerly NLLJ was located in eastern Colorado and western Kansas from 0300-0600 UTC (Fig. 6.4a,b), then shifted east by $\sim$1-2° of longitude from 0900-1200 UTC (Fig. 6.4,c,d). Wind vectors exhibited veering with time, similar to the previous dates and generally expected from the effects of an IO. Another similarity with the previous dates is some heterogeneous characteristics are evident with the veering of the v_{max}, except less pronounced than was seen on 8 June. For example, at 0300 UTC the v_{max} in south eastern Oklahoma has a noticeable easterly component while it is much more southerly closer to the jet core (Fig. 6.4a). Similar heterogeneous characteristics on 8 June were found to be associated with low-level easterly upslope flow. Examination of the u_{max} does indeed suggest a similar pattern as 8 June, with a shallow easterly u_{max} over eastern Kansas and Oklahoma at 0300 UTC (Fig. 6.5a). At this time an elevated westerly u_{max} is located in western Oklahoma and the Panhandle, characterized by speeds of $\sim$5-15 m s^{-1} at heights of 1800-2000 m (Fig. 6.5a). Over the following 3 h, a similar u_{max} developed over central Kansas and Oklahoma (Fig. 6.5b). In subsequent hours the u_{max} followed a similar evolution to 8 June,

characterized by becoming more uniform over the domain along with a lowering to heights of 1000-1400 m and intensification to 20-25 m s^{-1} from 0900-1200 UTC (Fig. 6.5c,d).

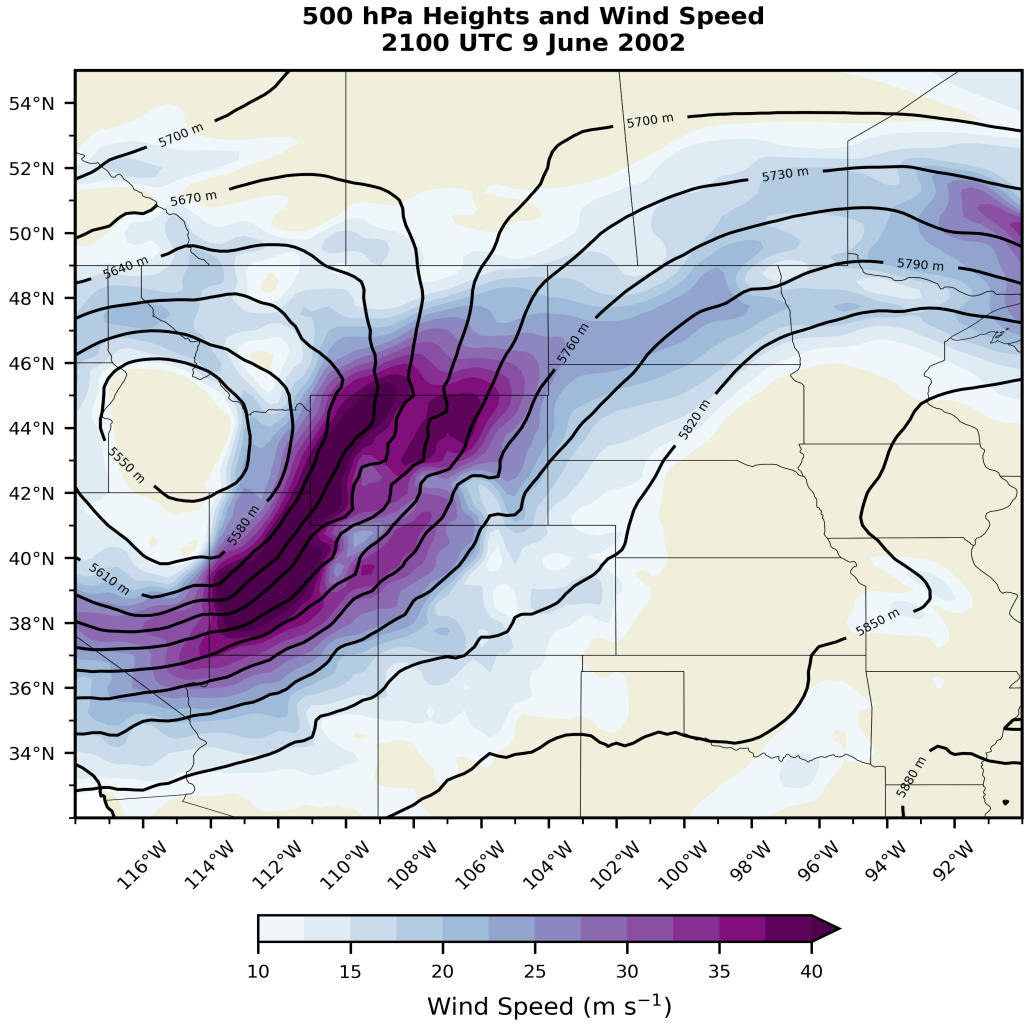

Figure 6.1: As in Figure 4.1 except for 2100 UTC 9 June 2002.

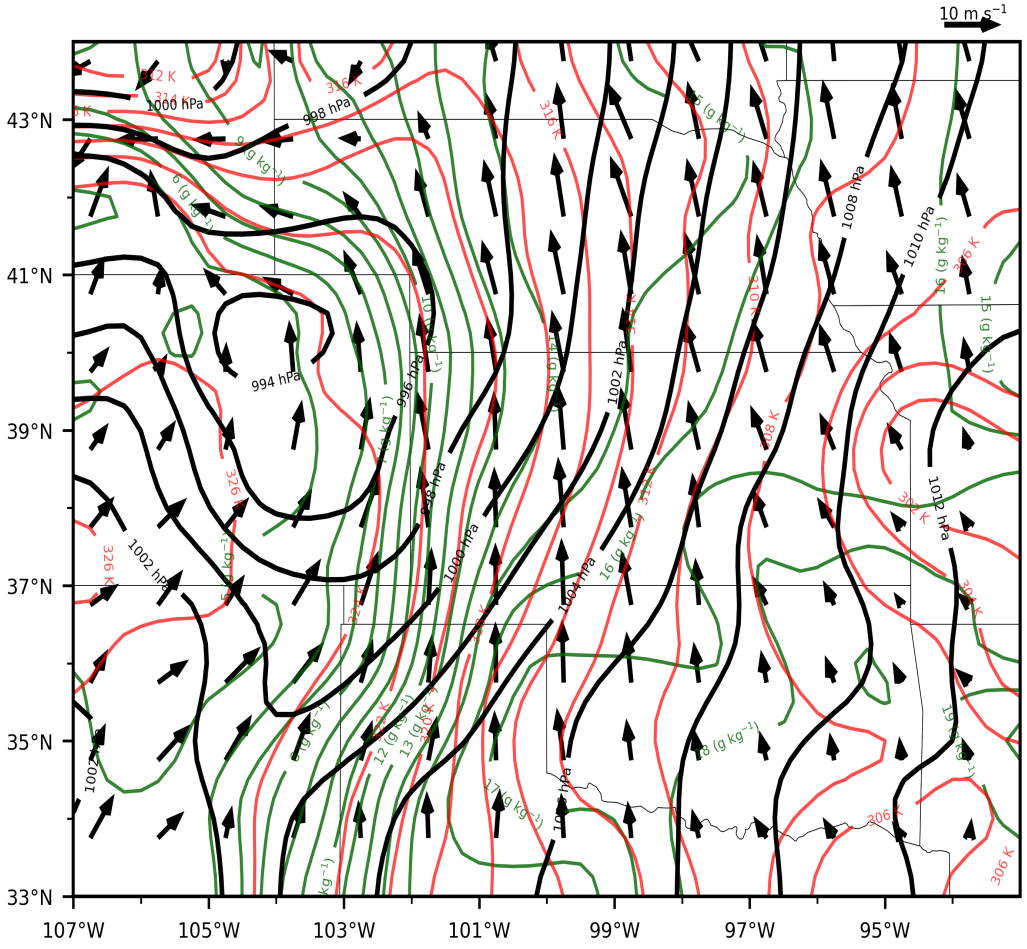

Figure 6.2: As in Figure 5.2 except for 2100 UTC 9 June 2002.

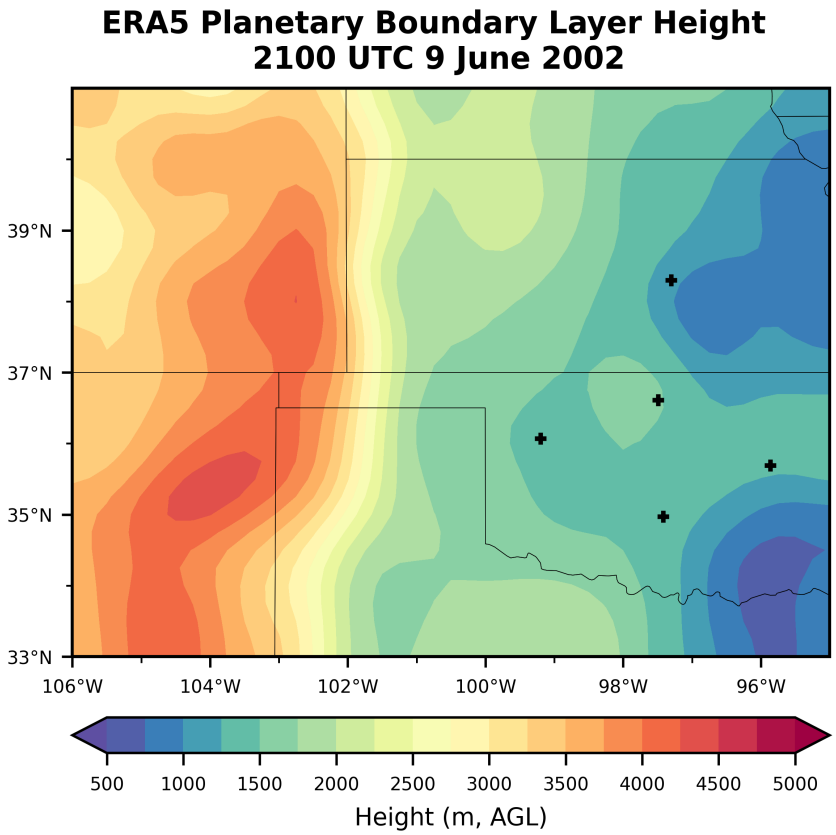

Figure 6.3: As in Figure 4.3 except for 2100 UTC 9 June 2002.

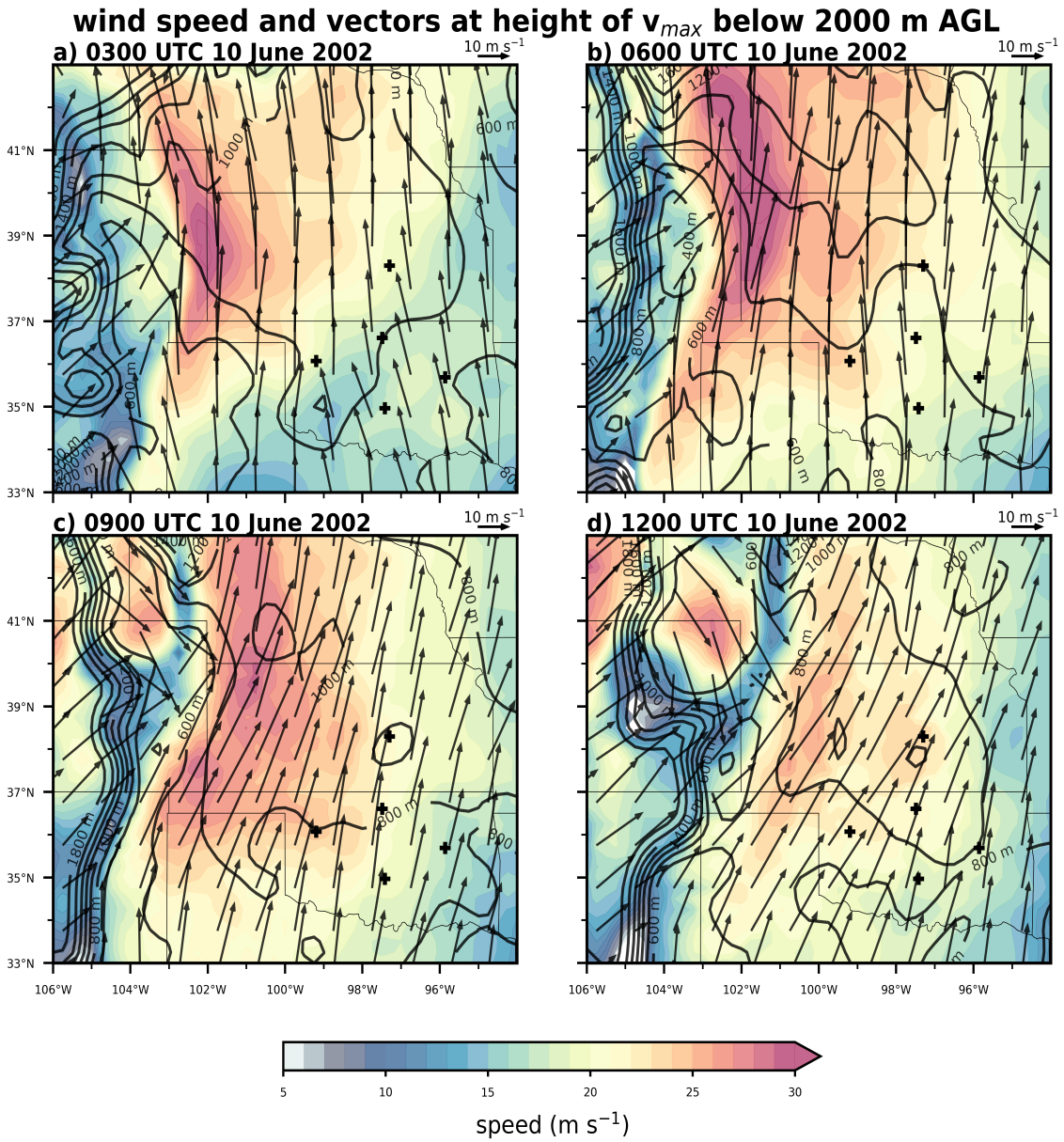

Figure 6.4: As in Figure 4.4 except for 10 June 2002 at times: a) 0300 UTC, b) 0600 UTC, c) 0900 UTC and d) 1200 UTC.

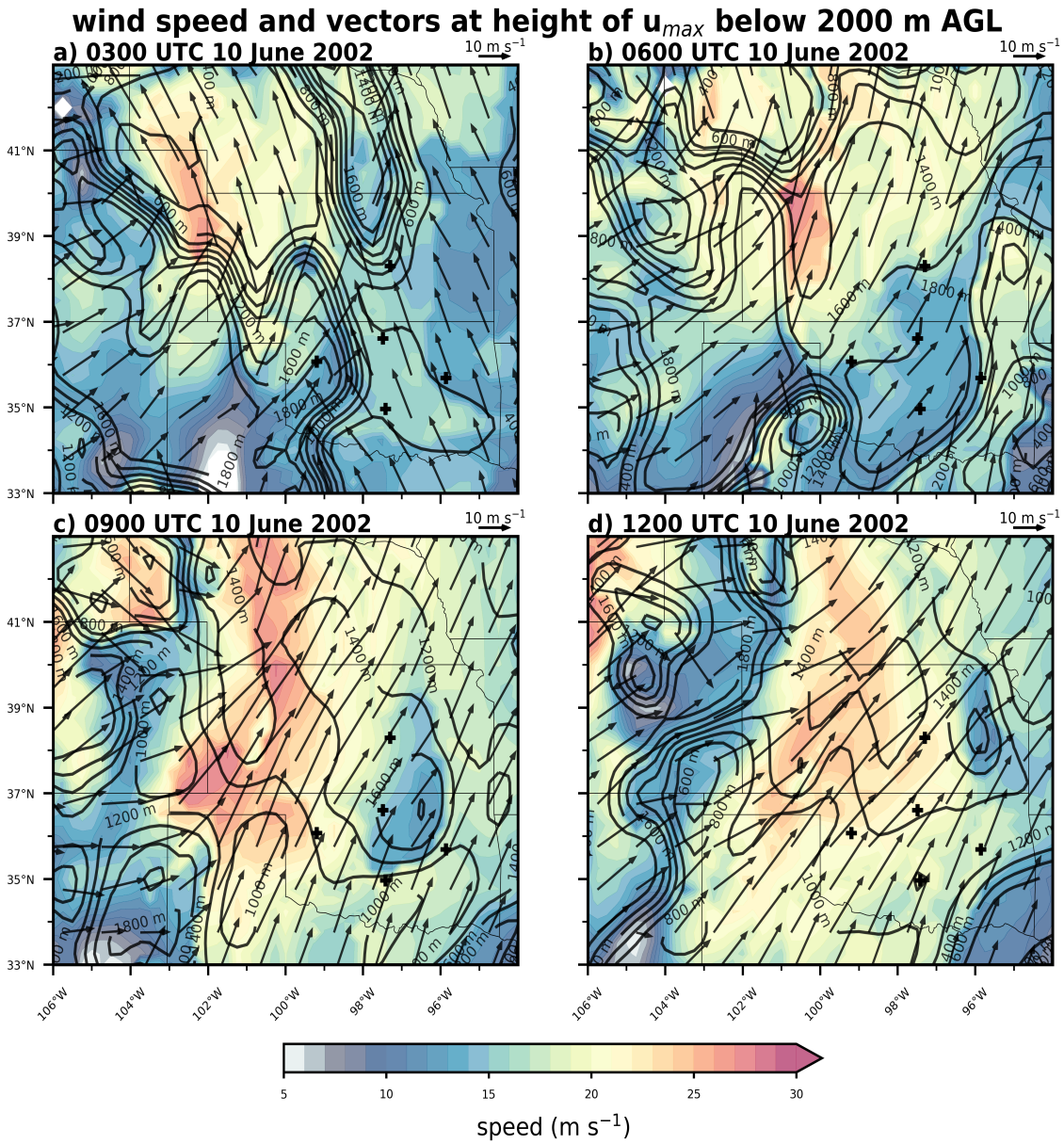

Figure 6.5: As in Figure 4.8 except for 10 June 2002 at times: a) 0300 UTC, b) 0600 UTC, c) 0900 UTC and d) 1200 UTC.

6.2 Analysis of Meridional Cross Sections

North-south cross sections were constructed from ERA5 reanalysis data over the central ARM site for 10 June to help provide insight into evolution of the southerly NLLJ. These cross sections reveal a more noticeable v_a component compared to the previous two cases, this was characterized by values of $\sim$5 m s^{-1} occurring with greatest intensity from 40-41°N at 0600 UTC (Fig. 6.6b). However, ageostrophic enhancements are dwarfed by changes to the geostrophic component, with magnitudes of $\sim$5-10 m s^{-1} occurring over the 3 h windows in Figure 6.6. One similarity to 7 and 8 June is a decrease in v_g occurring from 0600-0900 UTC over certain locations. This decrease in v_g is evident from 36-39°N, where v_g goes from $\sim$20 m s^{-1} to $\sim$10-15 m s^{-1} at heights below 2 km MSL (Fig. 6.6b,c). Over the same time an enhancement to v_a occurred, suggesting that this enhancement may be resulting from the actual wind not yet adjusting to its geostrophic value. One of the largest enhancements to v occurs from 0900-1200 UTC when v_g increases by $\sim$5-10 m s^{-1} at heights below $\sim$3 km MSL over locations 36-41°N (Fig. 6.6c,d). As stated earlier, such large variations in v_g make it difficult to determine the magnitude of southerly enhancement by the IO mechanism.

A northward advance of higher mixing ratio values is evident in Figure 6.6, despite previous analysis suggesting otherwise. Strength of the southerly flow does appear to be correlated with the northward advance of moisture in the 3 h windows in Figure 6.6. ERA5 cross sections suggest a stronger southerly flow was occurring over 0300-0600 UTC and 0900-1200 UTC compared to 0600-1200 UTC, moisture appears to advance $\sim$2° of latitude over periods with stronger flow (Figs. 5.2a,b and Fig. 5.2c,d) compared to $\sim$1° over the 3 h period with weaker flow (Fig. 5.2b,c).

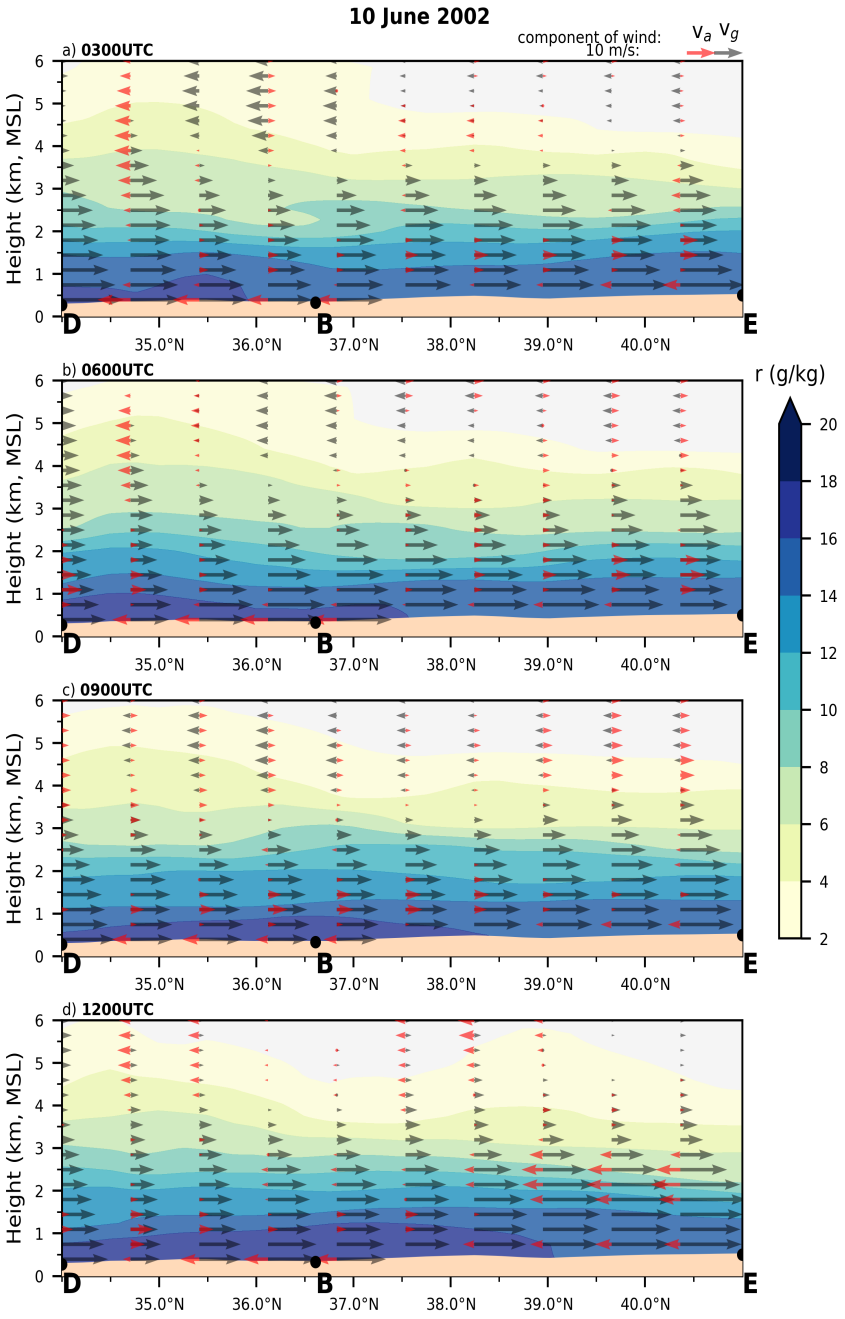

Figure 6.6: As in Fig. 4.5 except for 10 June 2002.

6.3 Analysis of Zonal Cross Sections

A sharper gradient in boundary layer characteristics compared to the previous dates (7 and 8 June) was evident along western portions of the slope at 0000 UTC. The most intense gradient was located from 101-102°W (Fig. 6.8). A deep, dry and relatively warmer boundary layer was located west of ∼102°W with a boundary layer depth of ∼4 km (Fig. 6.8a), θ_v values of ∼322 K (Fig. 6.8a) and mixing ratio values of 2-4 g kg^{-1} (Fig. 6.8b). In contrast, the boundary layer to the east of 101°W, was characterized by a boundary layer depth of ∼1.5 km (Fig. 6.8a), θ_v values of ∼310 to 315 K (Fig. 6.8a) and mixing ratio values of 12-16 g kg^{-1} (Fig. 6.8b). The most intense low-level southerly flow was located on the moist side of the interface between the two boundary layers where v was ∼20 m s^{-1} at heights of ∼1-1.5 km (Fig. 6.8b). The intensity of v_g near the surface over this area (Fig. 6.8a) is consistent with the southerly flow being generated by the baroclinic effects from the sharp thermal gradient. The moisture, thermal gradient, difference in boundary layer heights and southerly flow resemble a dryline.

From 0000-0300 UTC, the dryline advanced upslope, from 102°W to ∼103°W. Low-level v intensified over areas where the dryline retrogressed. This change is evident at 102°W; v increased by ∼10-20 m s^{-1} between 0000-0300 UTC (Figures 6.8b, 6.9b). Previous studies have documented southerly low-level jets forming east of a retrogressing dryline (Parsons et al. 1991; Ziegler and Hane 1993; Parsons et al. 2000).

Certain aspects of NLLJ evolution from 0000-0600 UTC within the moist airmass to the east are consistent with being produced by the IO mechanism. A southerly v reaching a maximum intensity at 0600 UTC is in agreement with being enhanced by the IO mechanism, given the strong v_g ($>$ 20 m s^{-1}) at 0000 UTC (Parish 2017). However, there is a lack of an enhancement to the southerly ageostrophic component east of 98°W (Fig. 6.10b). Two possible explanations are: 1) v intensified as a result of a non-IO mechanism or 2) the ageostrophic enhancement was masked by changes to the geostrophic component occurring between 0000-0600 UTC. Another aspect of NLLJ evolution that is difficult to

explain with the IO mechanism is the formation of a southerly NLLJ to the west of the dryline position at 0000 UTC as areas lacking a strong v_g during the daytime still developed a strong southerly NLLJ. For example, at 103°W, an intense southerly NLLJ ($>$ 20 m s^{-1}) formed by 0600 UTC (Fig. 6.10b) despite the lack of a southerly v_g component at 0000 UTC (Fig. 6.8a). Intensification at this location was associated with the passage of the retrogressing dryline from 0300 to 0600 UTC.

A local maximum of horizontal convergence with values of $16x10^5 s^{-1}$ was occurring at the leading edge of the dryline at 0300 UTC as it retreated upslope, of course the spatial resolution of the ERA5 is likely to poor to resolve the full magnitudes associated with this feature. One explanation for this rapidly developing southerly NLLJ was offered by Sun and Wu (1992), they suggested that this occurred when Coriolis force acted on the easterly u component associated with the dryline retrogressing. As the dryline retrogressed upslope it resembled a density current, characterized by negative θ_v advection of -2 k h^{-1} and ascent $>$ 14 cm s^{-1} (Fig. 6.9a,b). Density current characteristics are a well documented aspect of dryline evolution (Parsons et al. 1991, 2000; Geerts 2008).

The pressure field inferred from the geostrophic winds suggest a negative pressure perturbation followed the retrogressing dryline as it moved upslope. This pressure perturbation was located at heights of 3-6 km MSL being most intense within 1° of longitude of the dryline. Impacts of this pressure perturbation on the geostrophic winds are evident at 0000 UTC, a local maximum in southerly v_g is occurring at heights of 4-5 km at 101°W, along with a local maximum of northerly v_g at similar heights occurring at 102°W.This elevated area of low pressure agrees with finer scale observations of nocturnal dryline evolution (Parsons et al. 1991; Ziegler and Hane 1993; Atkins et al. 1998). For example, Parsons et al. (1991) observed a perturbation of -0.5 mb at heights of 3-5 km occurring east of a retrogressing dryline (see their Figure 7). Further work by Ziegler and Hane (1993) found this pressure perturbation could be significant in influencing horizontal accelerations to the

east of the dryline, this may explain the evolution of the area of mid-level convergence located in the Texas Panhandle.

The mid-level convergence in the Texas Panhandle resembles convergence found by Atkins et al. (1998) using aircraft and radar observations (see their Figure 13). The area of convergence at heights of 4-6 km on 10 June originated east of the dryline at 0000 UTC with subsidence below (Fig. 6.8a,b). This pattern is consistent with observations of dryline structure within an hour after surface heating ends (Atkins et al. 1998; Demoz et al. 2006). Using observations from a wind profiler, Demoz et al. (2006) documented similar convergence developed 20-25 km east at heights above 1.5 km of the dryline and also found subsidence occurring over the same area at heights of 1-2 km. Figure 6.9a suggests that low-level divergence was occurring east of the retrogressing dryline as a result of the easterly upslope flow. At 0300 UTC a narrow (1 km deep) band of divergence stretches from the retrogressing dryline east to 99-100°W (Fig. 6.9a). At 0600 UTC this divergence vanished (Fig. 6.10a), this occurred over a time when the easterly upslope flow diminished. This change in flow appears to have contributed to the intensification of mid-level ascent over an area near where the dryline was located during the daytime. This ascent was occurring above the mid-level convergence associated with the return flow of the dryline (Fig. 6.10a). Evidence of this ascent is seen in satellite IR imagery which shows a fine line of mid-level cloud cover oriented north-south, beginning to appear at 0532 UTC (Fig. 6.7c) and intensifying by 0645 UTC (Fig. 6.7d). The timing and rapid development of these clouds suggests that the developing ascent was associated with cessation of upslope flow. Intensification of low-level subsidence and mid-level ascent occurred over this area 0900-1200 UTC near 100°W along with convergence increasing from $\sim$2x10$^5 s^{-1}$ to $\sim$8x10$^5 s^{-1}$ at heights near 3 km (Figs. 6.11a 6.12a).

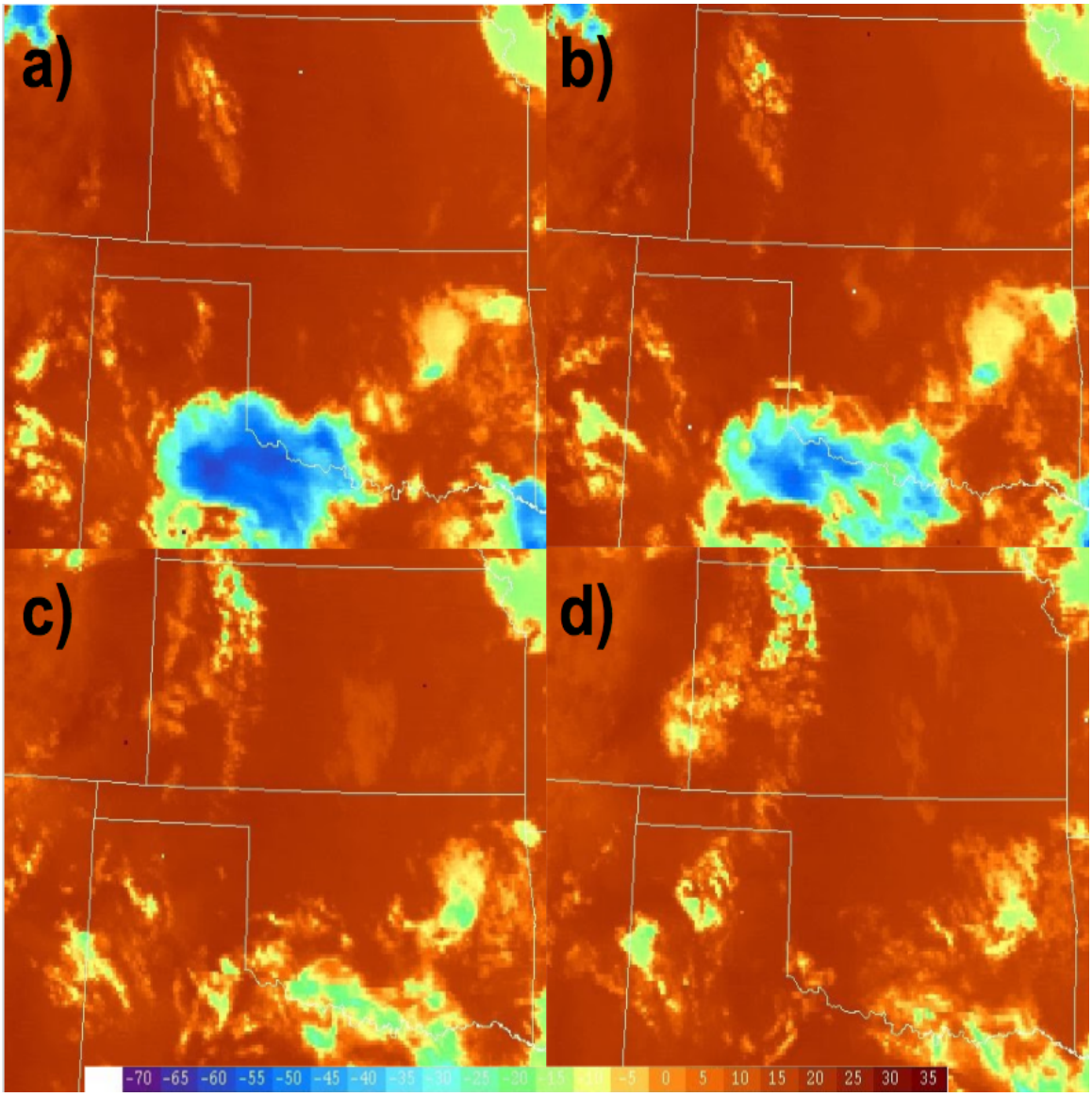

Figure 6.7: Infrared satellite images from the UCAR image archive valid at a) 0315 UTC, b) 0402 UTC, c) 0532 UTC, d) 0645 UTC on 10 June 2002 showing low-level clouds associated with weak ascent enclosed in the black window. The color scale for temperature (°C) is located at the bottom of the image.

These results again reveal that the $v_g(z)$ over some locations on the slope undergo large changes during the night with values of 10 to 15 m s^{-1} in the NLLJ events when a dryline is present. The significant evolution in v_g at these locations implies that the assumption of a constant $v_g(z)$ associated with Blackadar's IO mechanism may need to be evaluated in future studies. The non-uniform variations of these changes in $v_g(z)$ on the slope on 10 June compared to the earlier days discussed also suggests that the NLLJ over the SGP becomes more heterogeneous as the dynamics associated with the θ_v gradients and PBL height gradients become more significant in the presence of a dryline. Thus, this examination of the NLLJ in the synoptic framework suggests that the daytime characteristics on the slope need to be considered in order to understand the variations in the NLLJ and associated areas of ascent.

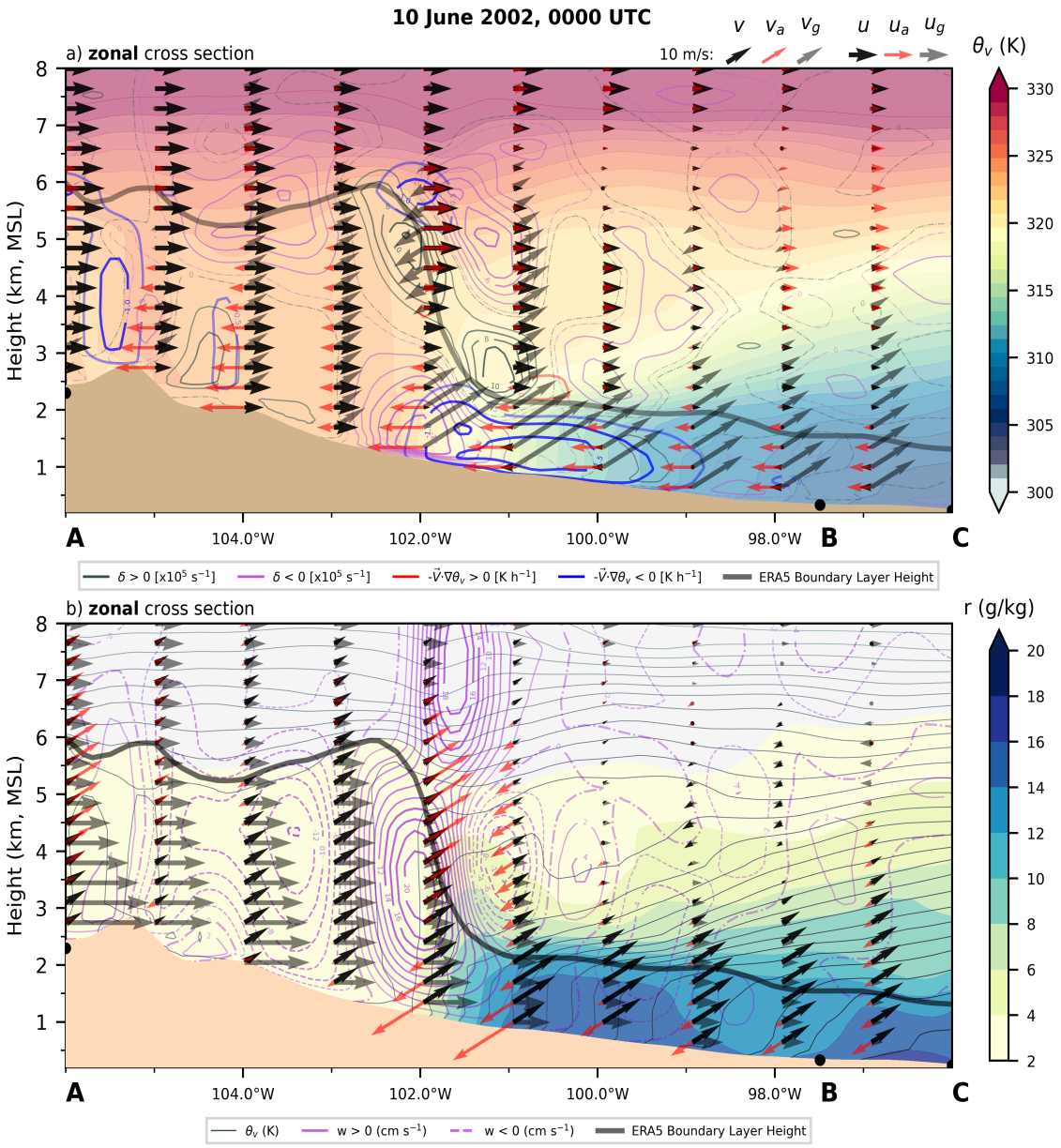

Figure 6.8: 0000 UTC 10 June zonal cross section from 96-106°W at 36.75°N, over the central site (B). Constructed from ERA5 reanalysis data containing geostrophic winds (black arrows), ERA5 boundary layer height ageostrophic zonal winds (red arrows) and for the top panel (a): θ_v color-fill, divergence (dark green contours), convergence (purple contours) and bottom panel (b): mixing ratio (color fill), θ_v (black contoured every degree K), w (purple contours).

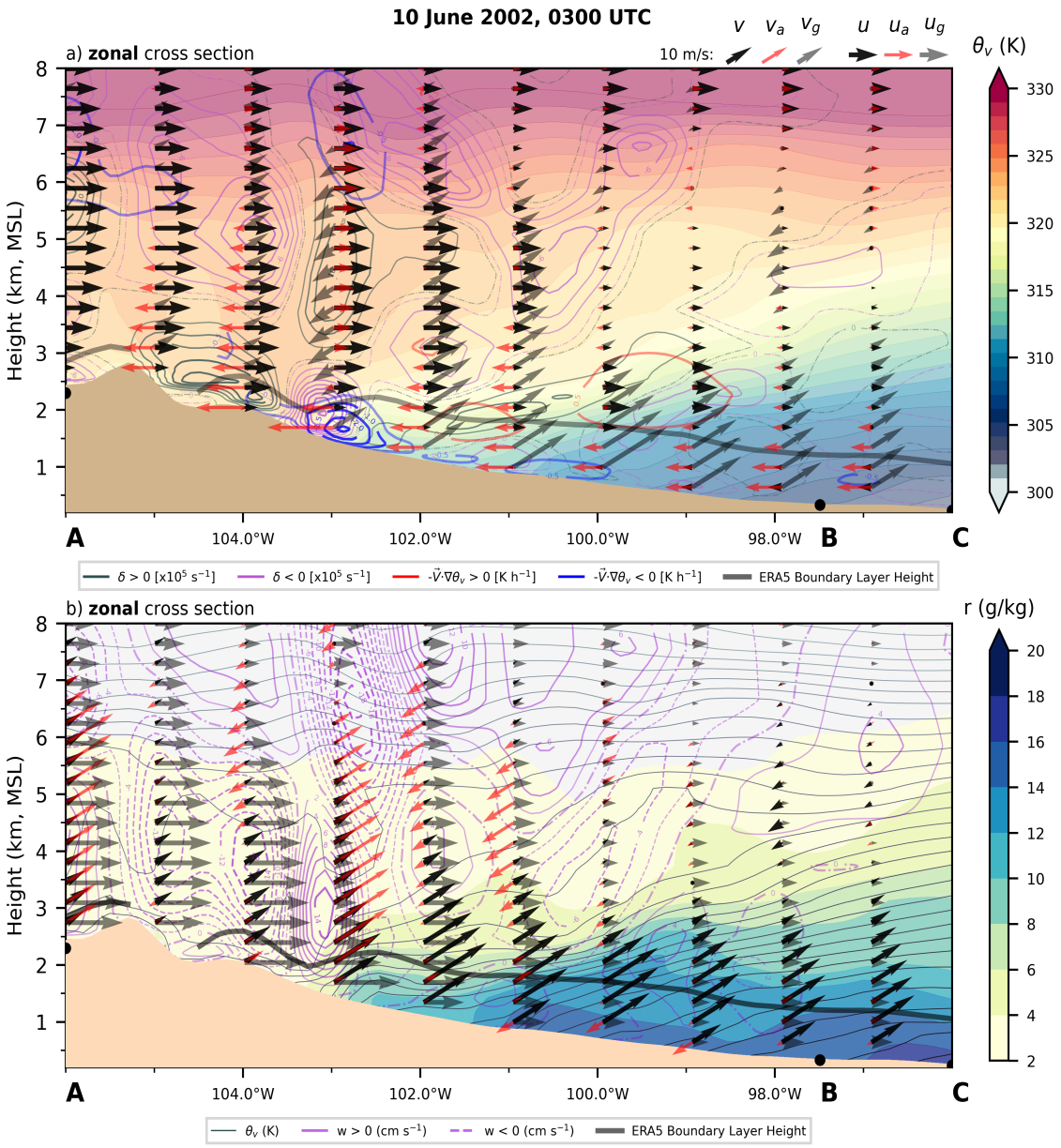

Figure 6.9: As in Fig. 6.8 except for 0300 UTC on 10 June.

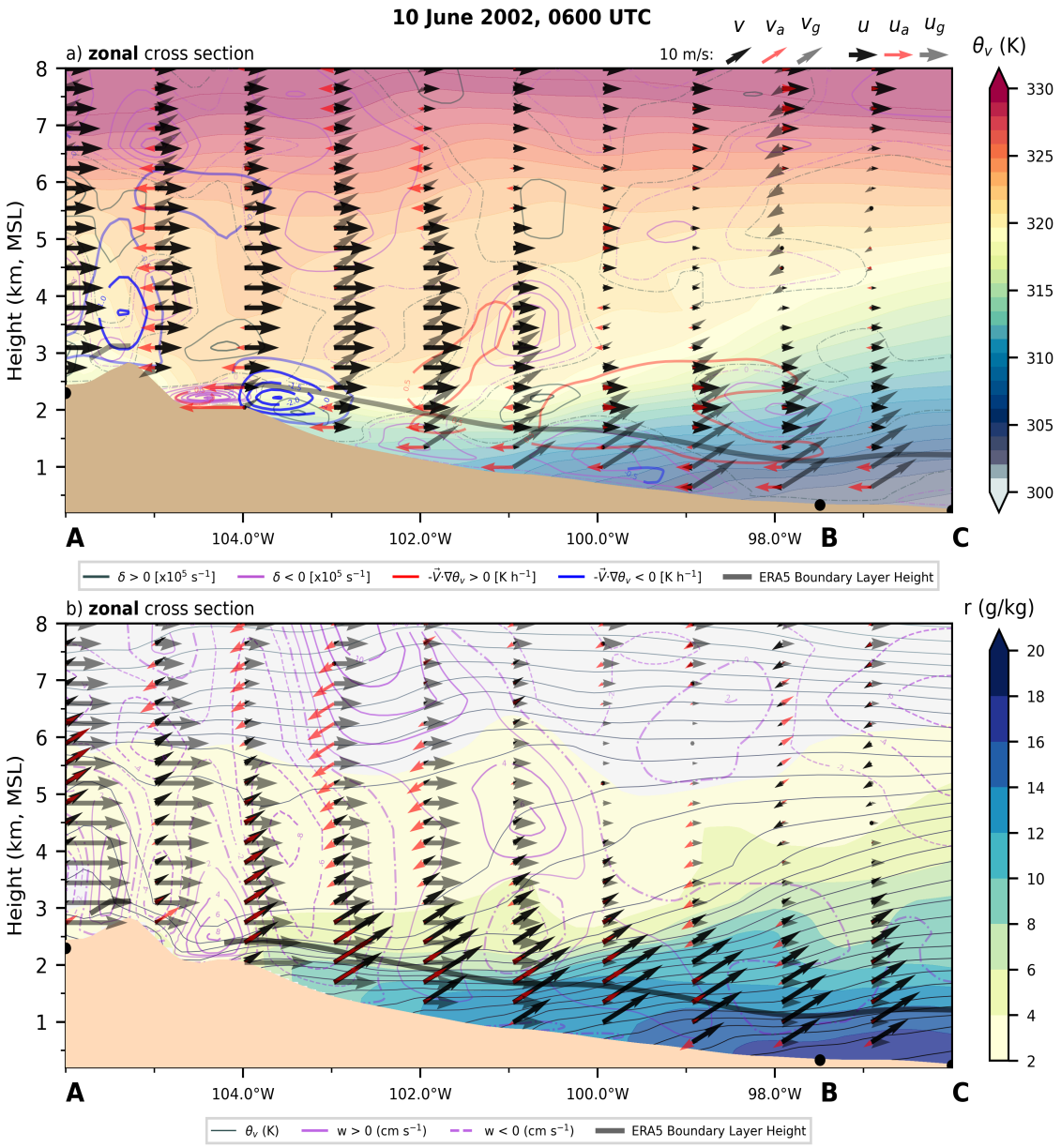

Figure 6.10: As in Fig. 6.8 except for 0600 UTC on 10 June.

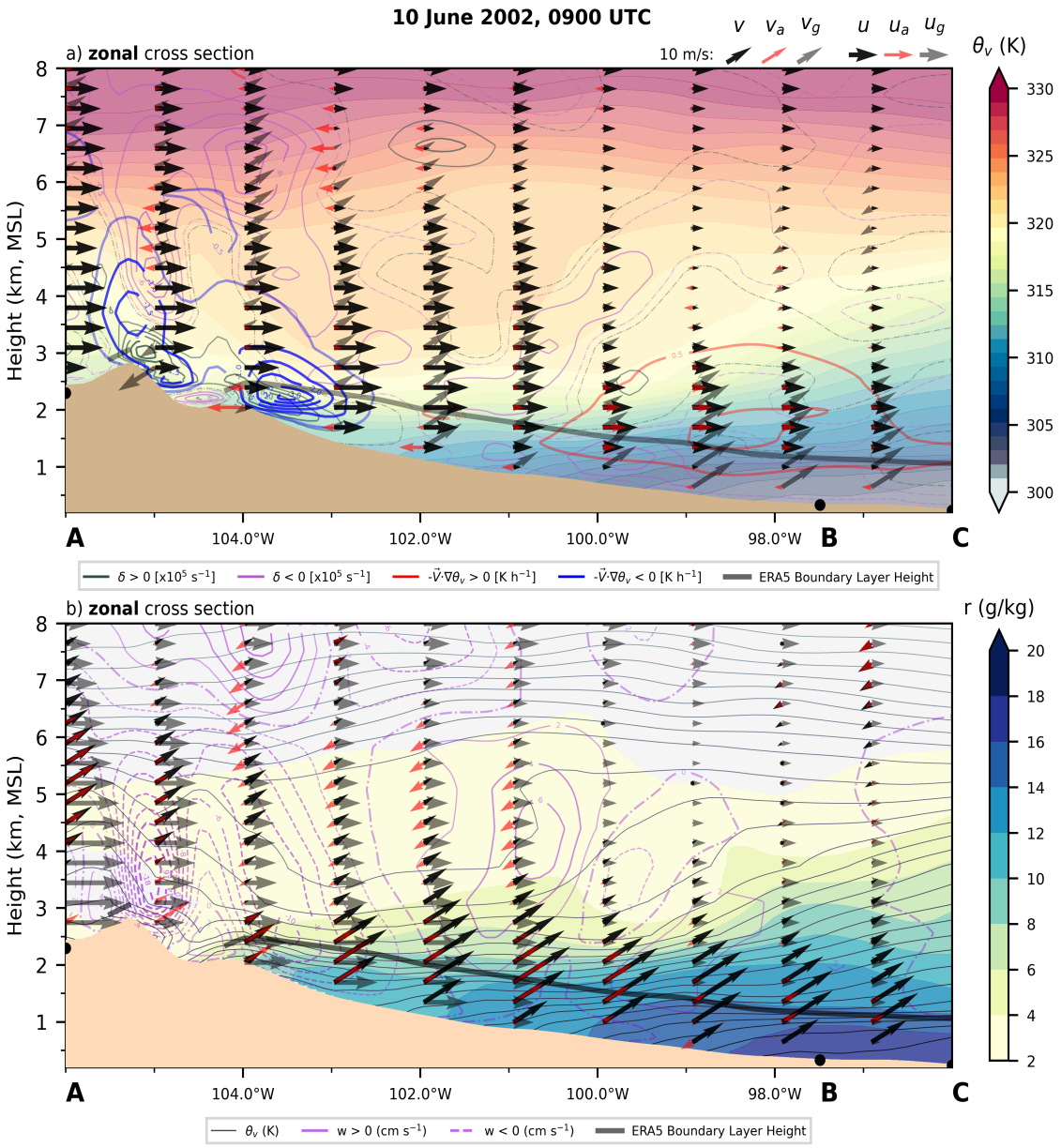

Figure 6.11: As in Fig. 6.8 except for 0900 UTC on 10 June.

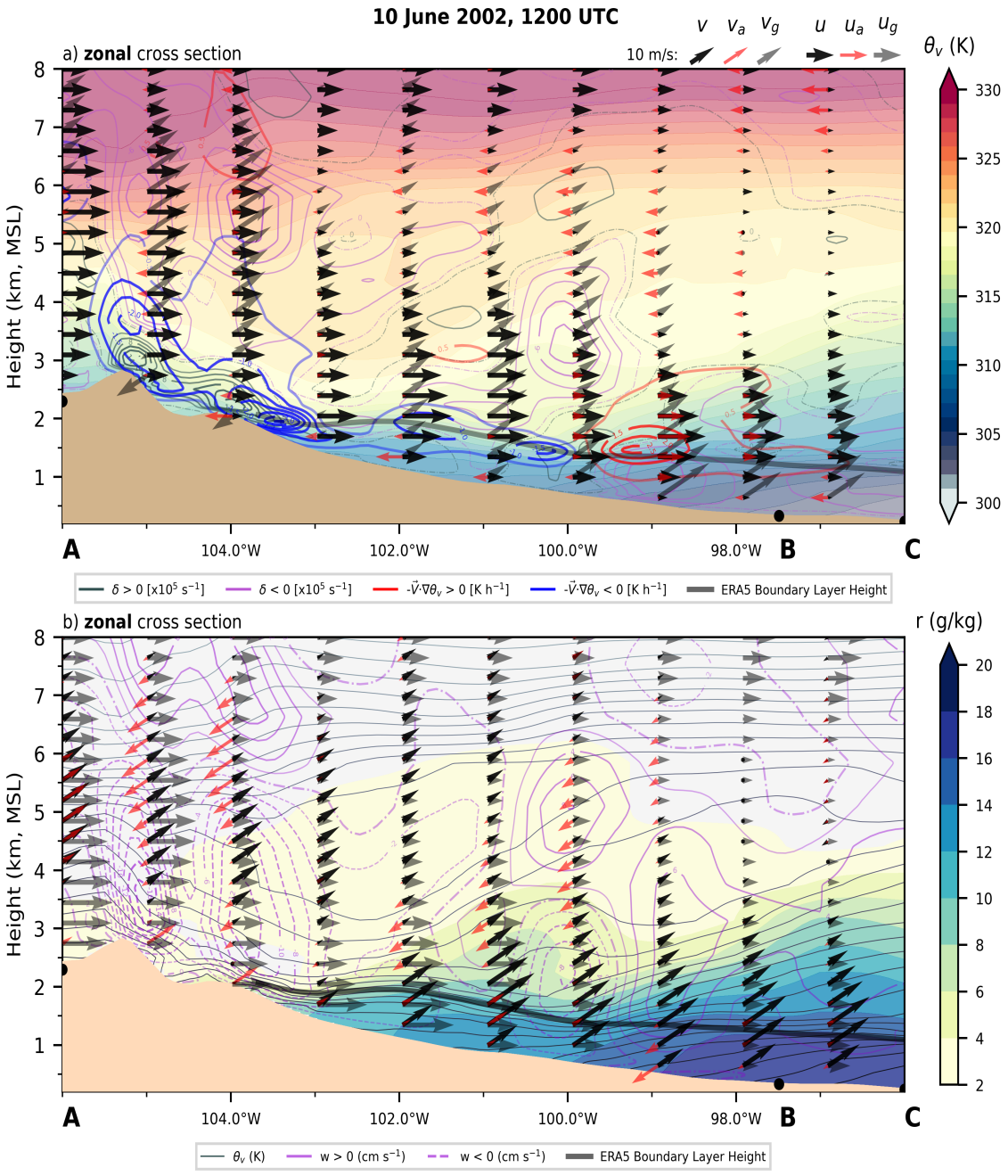

Figure 6.12: As in Fig. 6.8 except for 1200 UTC on 10 June.

6.4 Evolution of the NLLJ

Vertical profiles of θ_v indicate the ARM sites had a relatively uniform PBL with more similar θ_v and depths compared to the previous two dates. Boundary layers at the ARM sites were characterized by depths of 1.8 to 2.2 km with θ_v values of 307-312 K (Fig. 6.16). Although PBLs at the ARM sites were more similar than the previous two dates, some spatial variations were evident. These spatial variations were characterized by a warmer boundary layer at the western site with θ_v values of $\sim$312 K compared to $\sim$307 K at the eastern site (Fig. 6.16).

Similar spatial are evident in evolution of the wind profiles at the ARM sites. These variations were characterized by the most intense southerly NLLJ occurring at the western site and the weakest occurring at the eastern site. Both the western and northern sites had a v_{max} of $\sim$24 m s^{-1} (Fig. 6.13a,c), while the eastern site had a v_{max} of $\sim$20 m s^{-1} (Fig. 6.13b). In contrast to 7 and 8 June, the height of the v_{max} was relatively similar at the ARM sites, occurring at heights of 0.5-1 km, again suggesting the importance of daytime thermal gradients on the slope. This height similarity was interrupted at 1200 UTC by a relatively large change to v at the western site (Fig. 6.13a). This change was characterized by v decreasing by $\sim$5 m s^{-1} at heights of 500 to 1000 m, and an increase in intensity above 2 km (Fig. 6.13a). The southerly enhancement at heights of 2-3 km from 0600 to 1200 UTC is consistent with intensification of v_g by 5-10 m s^{-1} at these heights noted in analysis of meridional cross sections.

A similar enhancement to v was observed at the central, northern and southern sites (Fig. 6.13c,d,e), suggesting that this geostrophic enhancement was impacting the structure of the southerly NLLJ. This intensification of v aloft was also observed on the two previous dates. It was suggested that this enhancement was associated with a mesoscale pressure perturbation since these changes followed changes in v_g. Vertical profiles of the zonal PGF on 10 June indicates an increase of $\sim$5 hPa (1000 km)$^{-1}$ occurred between the western and central sites at heights of 1500-3000 m from 0900 to 1200 UTC. This intensification of the

PGF is of the order of magnitude needed to account for changes in v_g, thus providing further support that mesoscale pressure perturbations are impacting the structure of the southerly NLLJ.

A westerly NLLJ developed at the ARM sites in the overnight hours on 10 June (Fig. 6.14). Evolution of the westerly NLLJ exhibited some similarities that expected from the Shapiro et al. (2016) mechanism, such as a westerly enhancement occurring over a broad layer above the v_{max} and descending with time. The westerly NLLJ that developed at the ARM sites was characterized by a u_{max} of 5-15 m s^{-1} at heights of 1500-2000 m. One exception to this evolution took place at the western site from 0900-1200 UTC, a dramatic change in u occurred at the western site, over which time the u_{max} intensified by 5 m s^{-1} and became confined to a shallow $\sim$200 m deep layer at heights near 1000 m (Fig. 6.14a). One possible explanation for this deviation in evolution of the u_{max} at the western site may be that this is an acceleration associated with the variations in the mesoscale PGF. Variations in the PGF are evident by changes in v_g noted earlier in analysis of meridional and zonal cross sections. Zonal cross sections suggested that the western site was located near the western extent of large gradient in v_g, decreasing by $\sim$20 m s^{-1} from 99 to 100°W. The uniform changes in $v_g(z)$ are consistent with resulting from temporal variations upslope mass flux associated with the retrogressing dryline.

Vertical profiles of u from the ARM sites reveal low-level easterly upslope flow developed at the ARM sites, reaching peak intensity at 0600 UTC. This upslope flow was characterized by an easterly intensification of $\sim$5 m s^{-1} from its daytime value occurring over a 500-1000 m deep layer near the surface (Fig. 6.14). Analysis from previous dates found subsidence occurred with divergence associated with upslope flow with a tendency to be most pronounced in upper portions of the boundary layer. Such warming is evident at the western site from 0000-0600 UTC where θ_v increased by 2-3 K over this time. This easterly upslope flow may also offer an explanation for θ_v profiles resembling mixing near the surface, the rapid cooling which took place from 0000 to 0600 UTC could have been

from advection of cooler boundary layer air from the east, the tendency for this cooling to cease in later hours is also consistent with this.

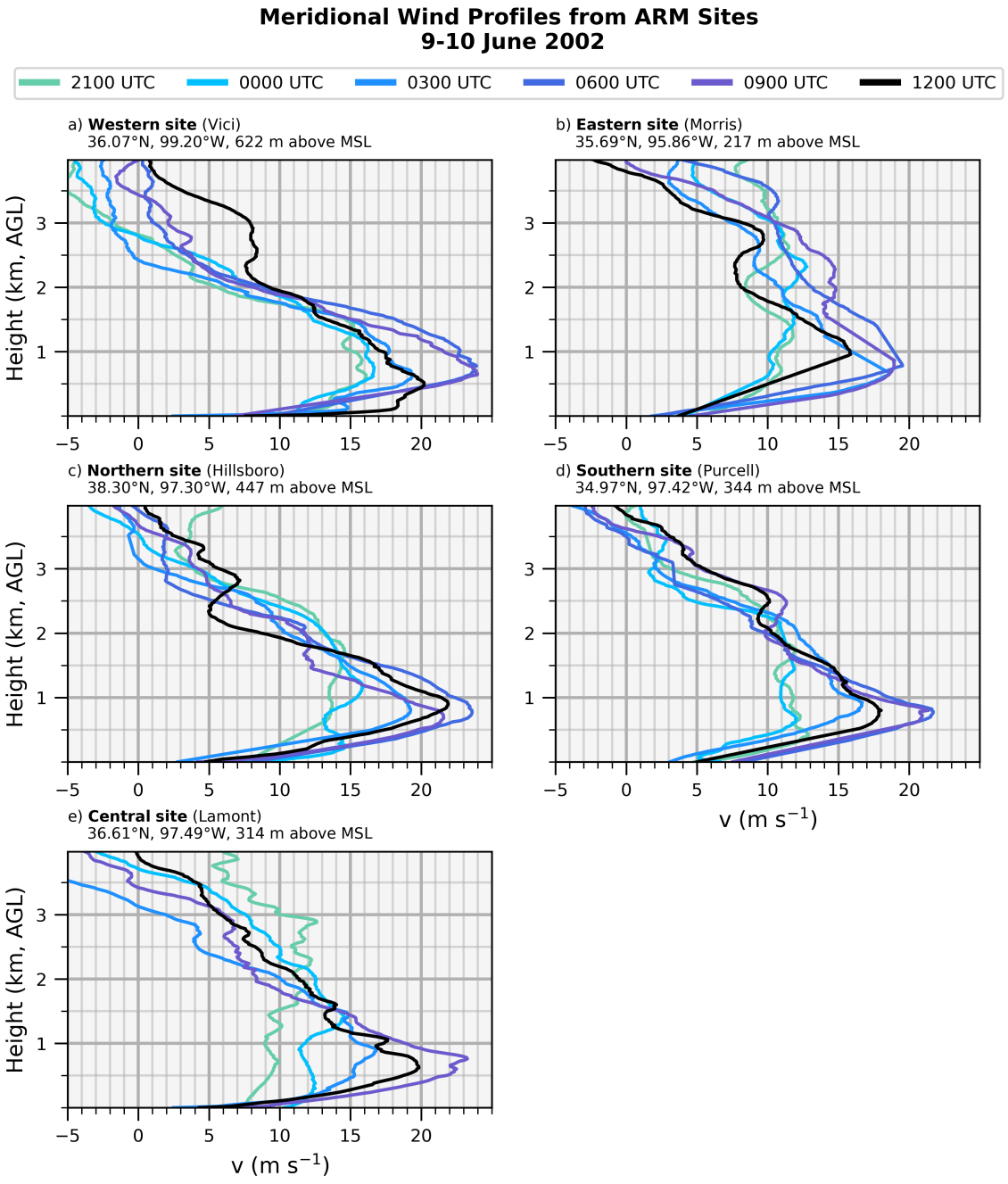

Figure 6.13: As in Fig. 4.6 except for 9-10 June 2002.

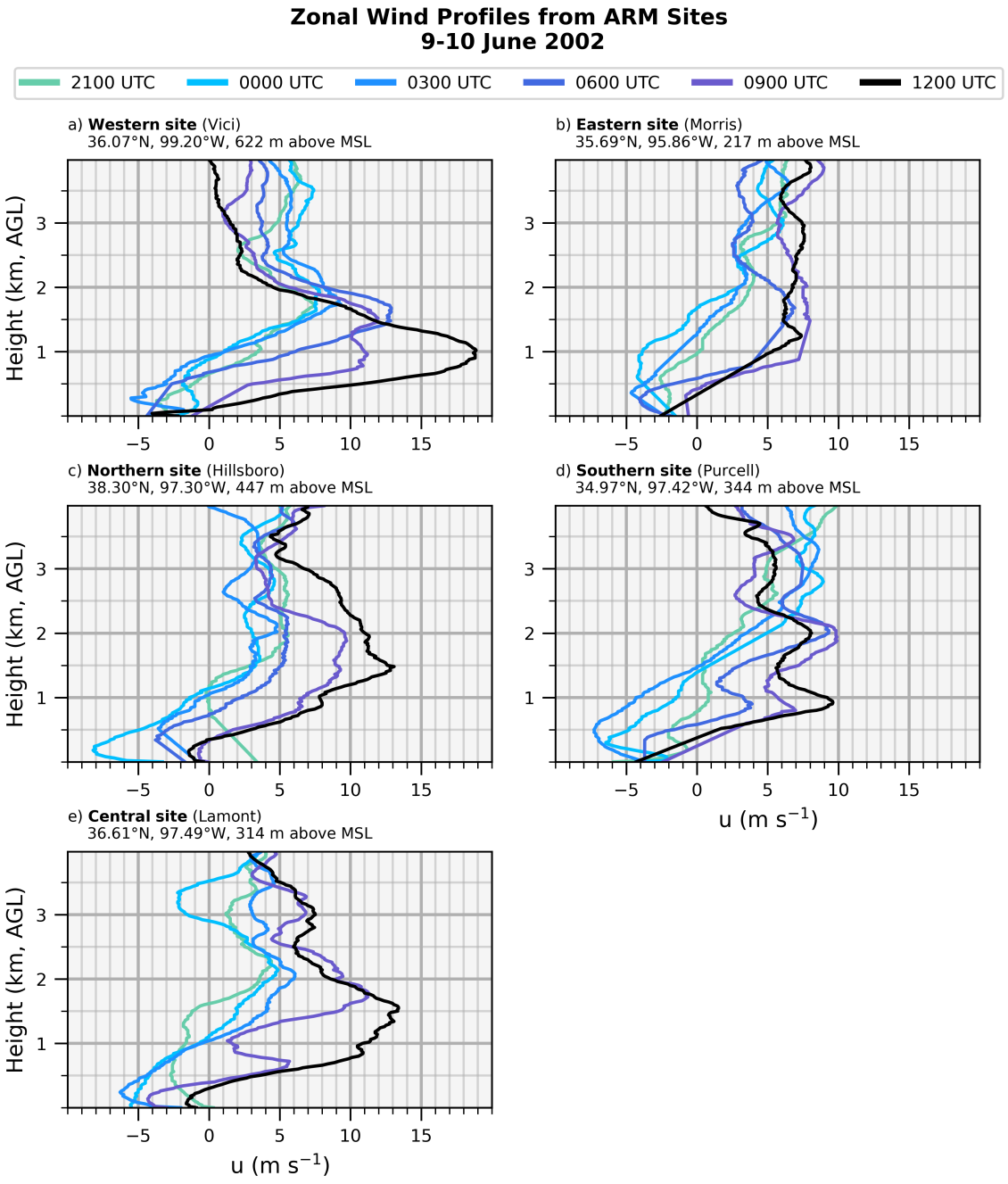

Figure 6.14: As in Fig. 4.9 except for 9-10 June 2002.

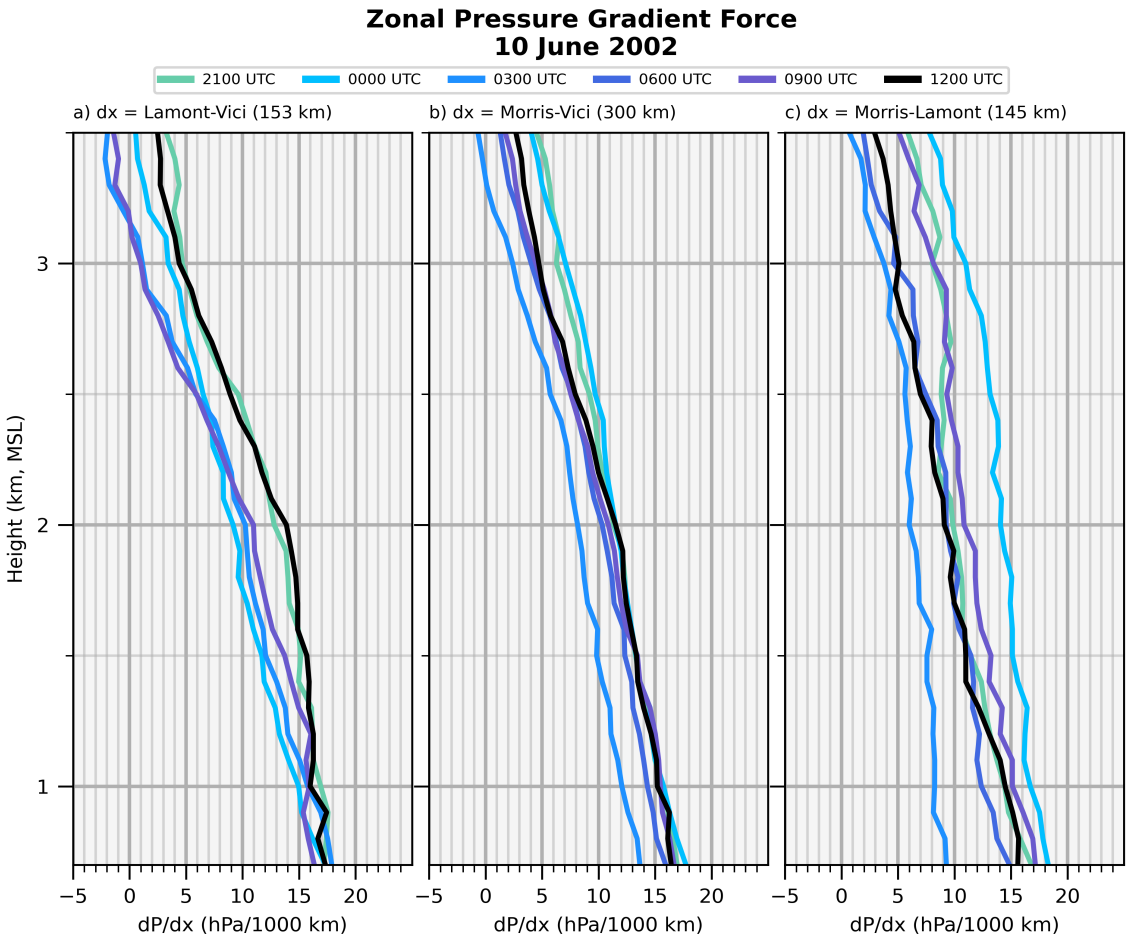

Figure 6.15: As in Fig. 4.11 except for 2100-1200 UTC 9-10 June 2002.

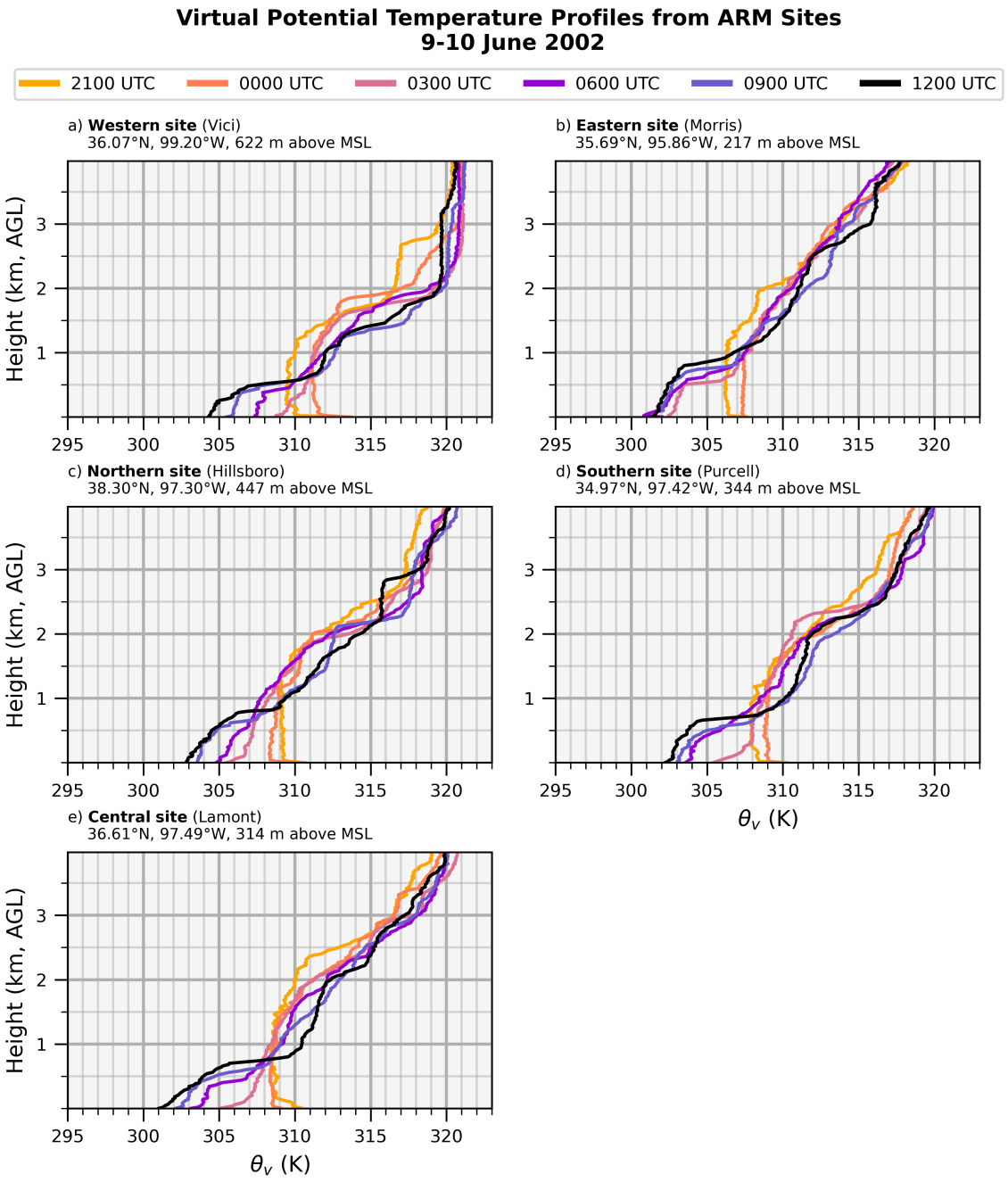

Figure 6.16: As in Fig. 4.10 except for 9-10 June 2002.

6.5 Evolution of Convective Destabilization

Significant destabilization of the environment to deep convection took place overnight on 10 June. This was characterized by CAPE increasing by 1000-1500 J kg^{-1} in layers aloft at all ARM sites except the southern site (Fig. 6.17). A west to east trend in destabilization took place, peaking at the western site at 0600 UTC (Fig. 6.17a). At this time a spike in CAPE occurred in two layers, at heights of 0.5-1 km and 1.5-2 km (Fig. 6.17a). The lower-level enhancement of CAPE appears to be associated with moistening that occurred from 0000-0300 UTC (Fig. 6.18a). Height and timing of this moistening are consistent with advection associated with the easterly upslope flow mentioned in the previous section. After 0600 UTC CAPE decreased by $\sim$1000 J kg^{-1} (Fig. 6.17a). This decrease appears to be from a combination of subsidence mentioned earlier and cooling near the surface associated with upslope advection of cooler boundary layer air (Fig. 6.16a). Mixing ratio values appear to have been capped around 17 g kg^{-1}, as this was near the maximum values of mixing ratios to the east. Since the western site reached this cap at 0600 UTC, the easterly advection no longer helped to destabilize after this time.

The remaining sites had moistening of $\sim$2 g kg^{-1} take place at over the two layers that destabilized and retained this moisture throughout the night (Fig. 6.18). This zonal variation in moisture is indicative of the movement of moisture away from the former location of the dryline by the enhanced westerly flow. This is further supported by examination of moisture advection at later times moisture becomes even more pronounced when the dramatic intensification to the u_{max} at 1200 UTC, this resulted in zonal moisture advection going from $\sim$0 to 0.5 g kg^{-1} h^{-1} at a height of $\sim$800 m (Fig. 6.20d). As noted earlier, this intensification of the u_{max} was associated with a mesoscale pressure perturbation occurring near the former location of the dryline.

Another feature that developed near the former location of the dryline was an area of elevated convergence, earlier results found that this was likely resulting in reduced static

stability at mid-levels. Impacts of this convergence are evident in analysis of Skew-T diagrams at the ARM sites. These profiles indicate static stability decreased at heights of 600-300 hPa and did indeed contribute to enhancements in CAPE (Fig. 6.21). Changes in the temperature profile were more pronounced in times after 0600 UTC (Fig. 6.21), consistent with analysis of zonal cross sections. These changes in temperatures aloft were characterized by warming of 1-3 K at heights below 600 hPa and similar magnitudes of cooling above taking place from 0000-1200 UTC. Previous studies have also documented reduced static stability aloft occurring in an environment with a NLLJ (Trier et al. 2017; Parish et al. 2020). In a case documented by Parish et al. (2020) from the PECAN field campaign, a similar evolution to the temperature profile was observed, it was suggested that this may have been associated with quasi-geostrophic ascent from warm air advection. Since previous analysis found that the u_{max} was largely ageostrophic, being an order of magnitude larger than that assumed for quasi-geostrophic theory (Bluestein 1992), this does not offer a plausible explanation for the reduced static stability on 10 June. Analysis of zonal cross sections indicated that this layer of reduced static stability was associated with mid-level convergence rather than advection of the remnants of the deep and dry boundary layer from the west, as horizontal advection depicted in zonal cross sections was minimal at these heights.

Previous analysis of IR satellite imagery found that mid-level convergence was associated with the development of clouds that resembled shallow convection, this suggests the area of elevated convergence associated with the dryline may act as a source of lift for CI. This is supported by examination of NEXRAD radar composites. At 0600 UTC these composites reveal isolated areas of shallow convection ($<$ 35 dBz) located in northwestern Kansas and the central Texas Panhandle (Fig. 6.22a). The area containing shallow convection in the Texas Panhandle is likely associated with cloud cover that developed over an area of elevated convergence noted earlier. An intensification and eastward shift of this convection occurred over the following 6 h, developing into a north-south oriented band

located over western Kansas and the eastern Texas/Oklahoma Panhandle. Zonal cross sections indicated that the largest ascent over these longitudes occurred near $\sim$100°W owing to a dramatic westerly intensification of the u_{max}. Calculations of vertical velocities at the ARM sites indicate that intensification of the u_{max} at 1200 UTC at the western site was associated with convergence increasing by $\sim$3 x10^{-5} s^{-1} (Fig. 6.19b). This convergence resulted in ascent of $\sim$2 cm s^{-1} at the central site (Fig. 6.19a). The timing of this CI is similar previous investigations of nocturnal CI without a nearby surface boundary (within 3° of latitude or longitude) (Trier et al. 2017; Reif and Bluestein 2017; Gebauer et al. 2018; Reif and Bluestein 2018). Previous studies have also documented similar elevated convergent layers suspected to be a source of nocturnal CI in an environment with no nearby surface boundary (Banacos and Schultz 2005; Wilson and Roberts 2006; Reif and Bluestein 2018), suggesting that this elevated convergence mechanism for CI taking place on 10 June 2002 may not be a rare or isolate incident.

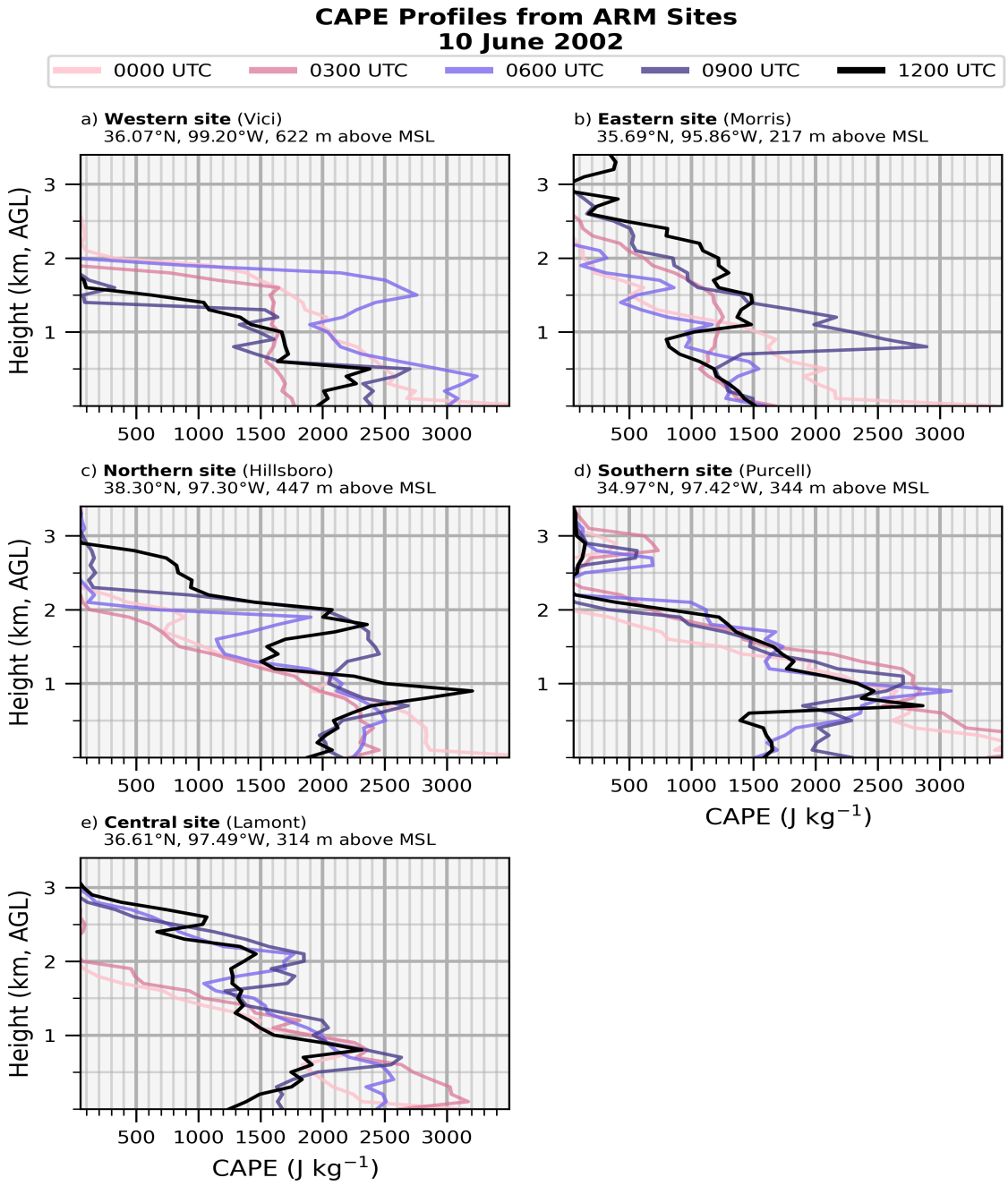

Figure 6.17: Profiles of CAPE as a function of height from 0000-1200 UTC 10 June 2002 taken from sounding data collected from the 5 ARM sounding sites: a) western site (Vici), b) eastern site (Morris), c) northern site (Hillsboro), d) southern site (Purcell), and e) central site (Lamont).

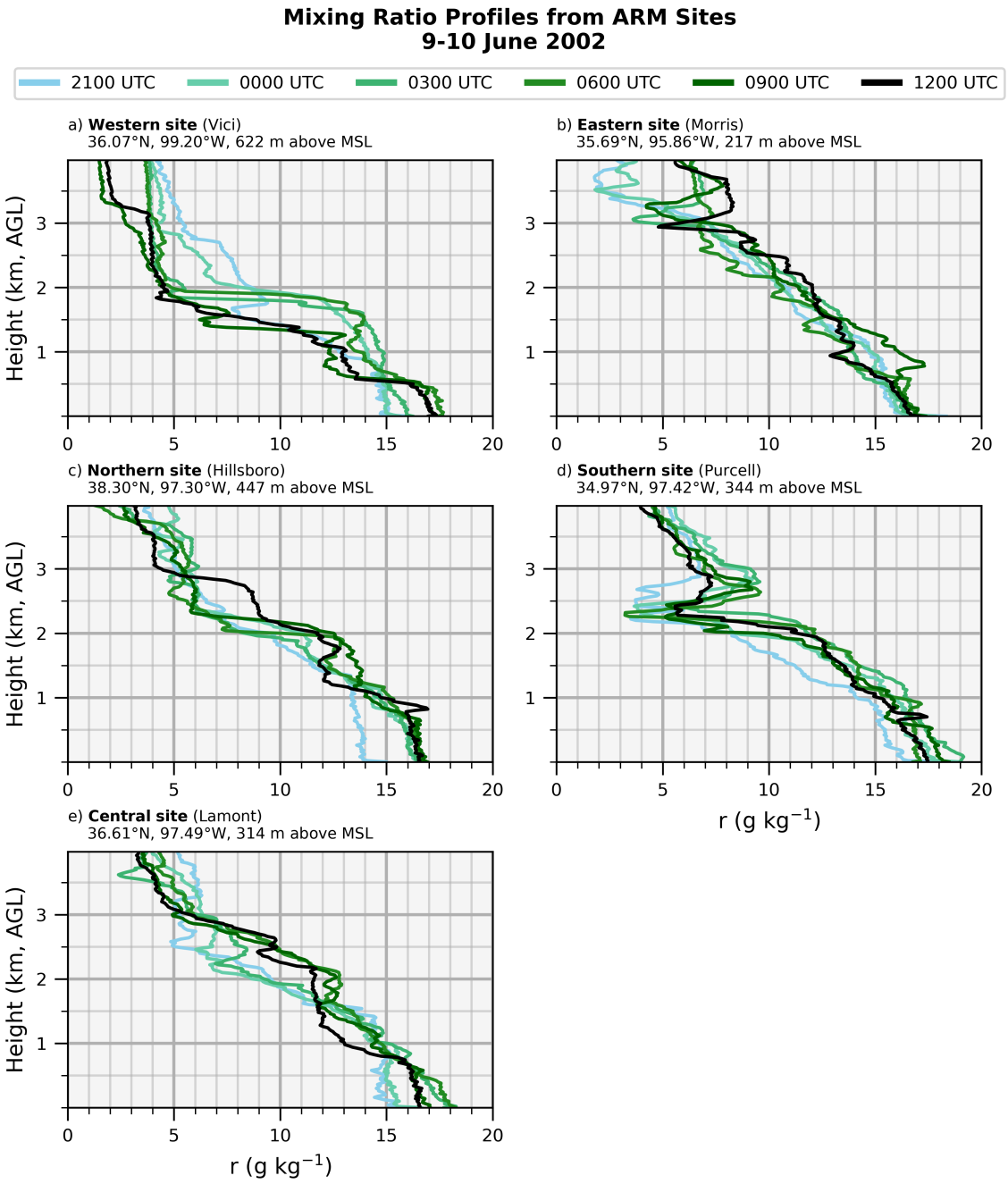

Figure 6.18: Vertical profiles of mixing ratio values (mixing ratio) from 0000-1200 UTC 10 June 2002 taken from sounding data collected from the 5 ARM sounding sites: a) western site (Vici), b) eastern site (Morris), c) northern site (Hillsboro), d) southern site (Purcell), and e) central site (Lamont).

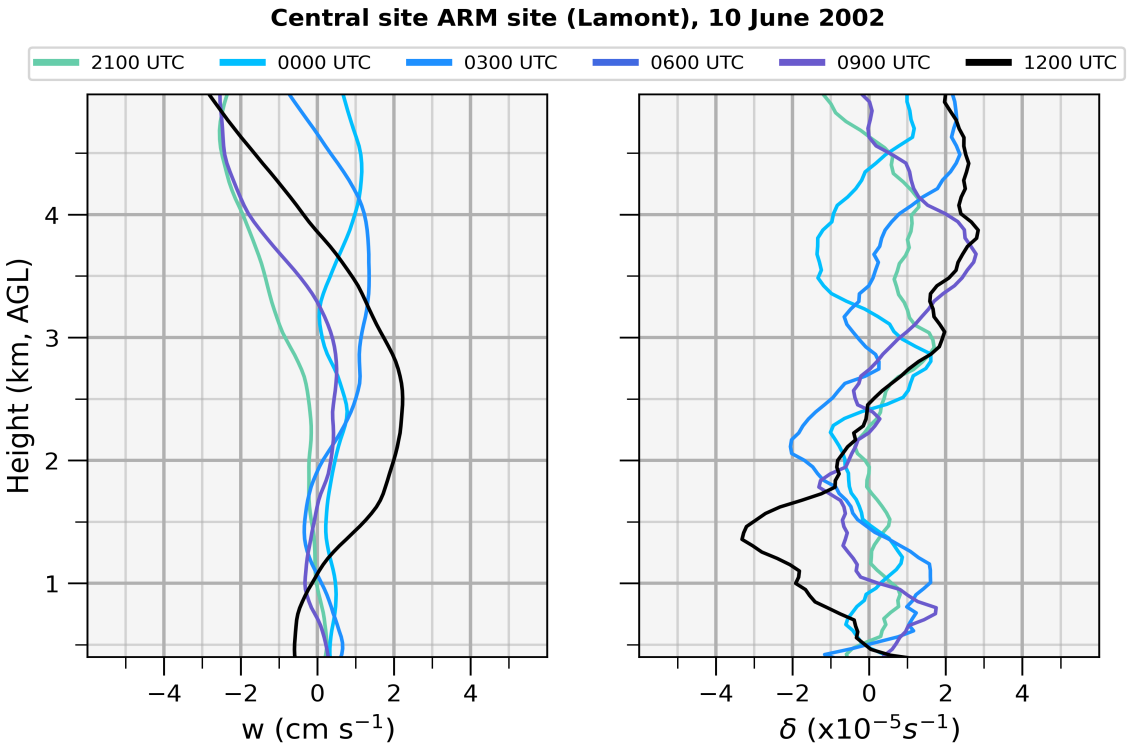

Figure 6.19: As in Fig. 4.12 except for 9-10 June 2002.

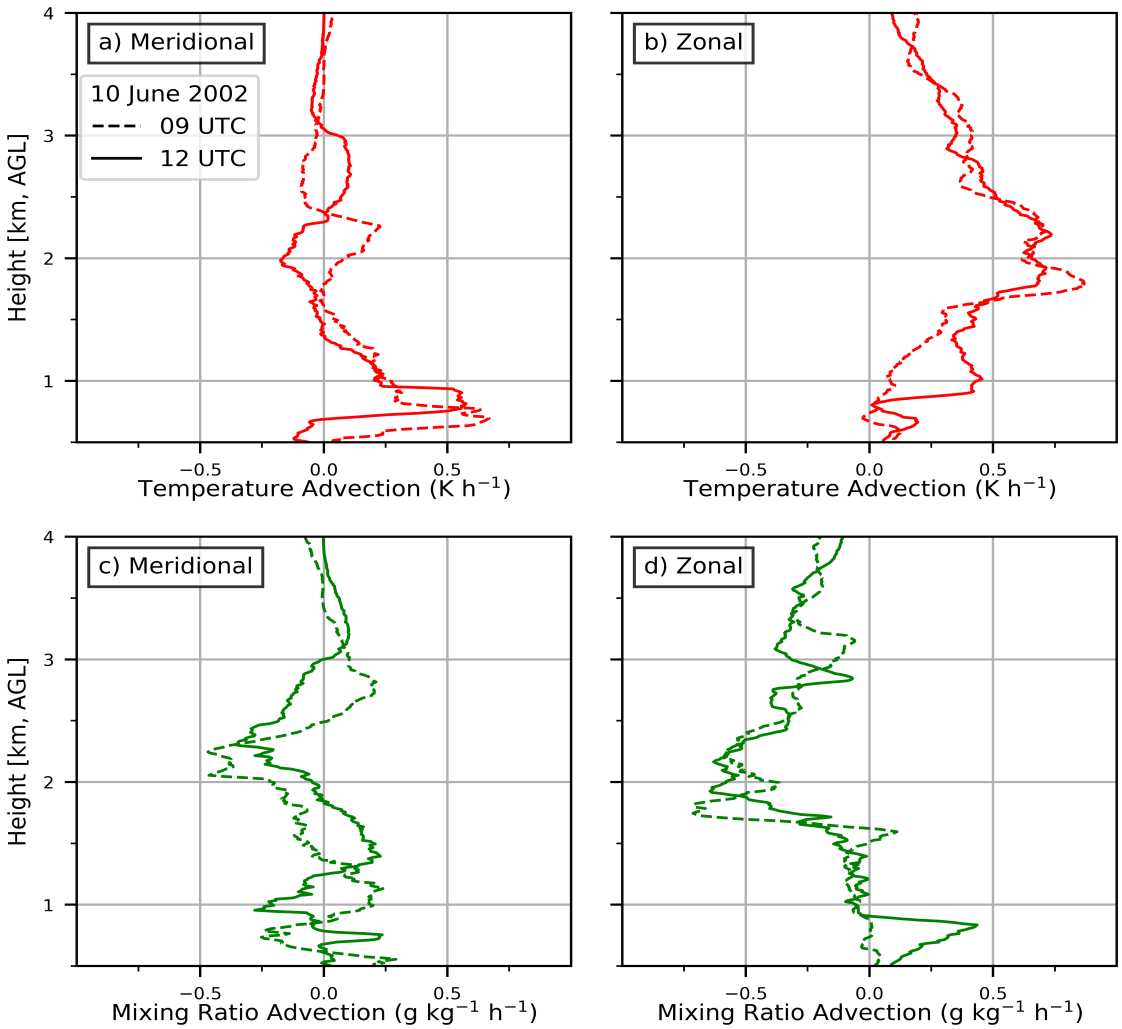

Figure 6.20: As in Fig. 5.18 except for 10 June at times: 0900-1200 UTC (wind data is unavailable for the central ARM site at 0600 UTC).

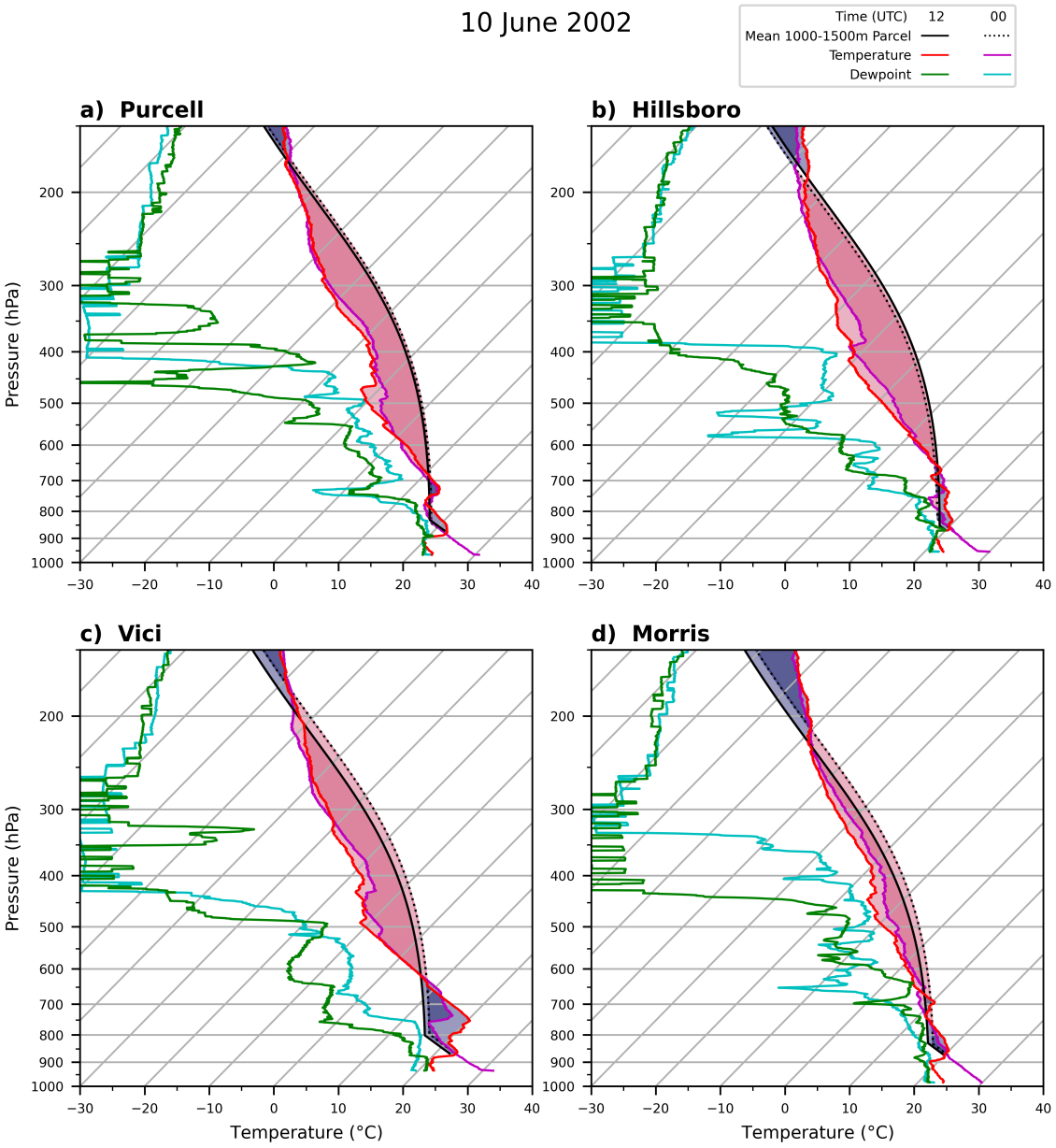

Figure 6.21: As in Fig. 5.22 except for 10 June 2002.

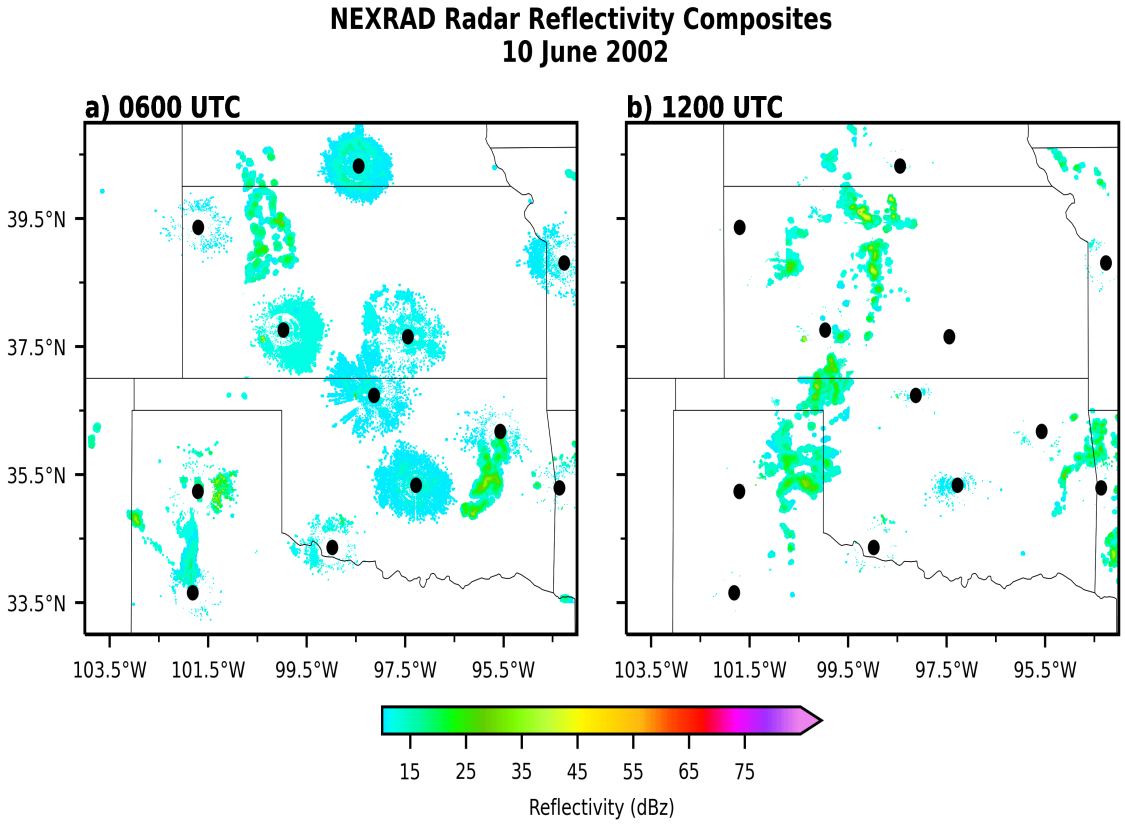

Figure 6.22: Reflectivity (dBz) from National Weather Service NEXRAD level 2 radar composites for 10 June 2002 at a) 0600 UTC and b) 1200 UTC. Black dots indicate location of radar locations.

6.6 Discussion

A more intense southerly NLLJ developed at the ARM sites compared to the previous two dates. Evolution of the southerly NLLJ exhibited some characteristics consistent with being influenced by an IO, such as veering with time and being strongest near locations of the largest daytime PGF. However, this preferred location also overlapped with a sharp gradient in PBL characteristics consistent with a dryline. Evolution of the dryline created a more complex environment, containing regions of ascent and subsidence. In addition, the geostrophic component was found to exhibit much larger diurnal variations than the ageostrophic component at the height of the v_{max} in vertical cross sections, making it difficult to determine magnitudes of ageostrophic enhancements associated with an IO. Furthermore, the vertical structure of the southerly NLLJ exhibited a strong correlation with the geostrophic winds, suggesting winds were adjusting to their geostrophic values.

The southerly NLLJ took place in an active synoptic environment, with a 500 hPa trough located to the west. Previous studies have found that this synoptic pattern is associated with coupled low-level jets (e.g., Uccellini 1980; Burrows et al. 2020). However evolution of the southerly NLLJ was more closely associated with the retrogessing dryline, since it was likely the source of mesoscale pressure perturbations impacting v_g. The enhanced upper-level flow may have had an indirect impact by facilitating the formation of the dryline, since it is known that mixing down of westerly momentum in the dry boundary layer is a key ingredient for the formation of these boundaries (Sun and Wu 1992).

Upslope flow associated with the retrogressing dryline also contributed to spatial differences in destabilization. Advection of moist air from downslope created a more favorable environment for convection along western portions of the slope for the first several hours after boundary layer decoupling. In subsequent hours this destabilization shifted east, as a result of a westerly intensification. This westerly intensification created a more favorable environment to the east by advecting low-level moisture and created areas of convergence leading to ascent. Analysis of NEXRAD radar composites indicated that this convergence

was likely the source of CI for shallow convection that initiated in western Kansas and the eastern Texas/Oklahoma Panhandle. Although intense warm air advection was occurring, the highly ageostrophic nature of the u_{max} means that quasi-geostrophic theory may not be suitable for explaining ascent from warm air advection associated with the u_{max}.

Chapter 7

Conclusion

The two goals of this thesis were: 1) to document the structure and dynamics of the day-to-day evolution of a NLLJ within a synoptic framework and 2) investigate how this evolving flow created a more favorable environment for convection and precipitation. To address these goals, the evolution of the NLLJ was examined after two cold frontal passages over the SGP. Sets of dates occurring in between cold frontal passages were referred to as recovery periods. Analysis of the ARM sounding data for two recovery periods indicated that the observed increase in the southerly NLLJ was largely driven by an increase in V_g during the recovery period with a nightly ageostrophic enhancement. The sounding data also revealed that the NLLJ consistent of a southerly and westerly maximum as found in the analytical study of Shapiro et al. (2016) and other subsequent investigations such as Gebauer et al. (2018), Parsons et al. (2019a), Smith et al. (2019), and Parish et al. (2020). Our analysis of the sounding data also found that the height of the southerly and westerly maximum also tended to increase with time during the recovery periods.

Subsequently, this thesis examined NLLJ evolution in detail for one of the recovery periods that occurred between the cold frontal passages on 5 and 13 June 2002. A case study format examined 3 dates from a period of rapid moistening, with each date occurring at either the onset of moistening, during the moistening or post moistening. Evolution and structure of NLLJ for a given day during the second recovery period depended on the evolution of the return of a baroclinic zone. This zone which was removed by the frontal passage and returned in subsequent days as daytime heating returned thermal gradients to the slope. The importance of thermal gradients along the slope to development of low-level jets has been noted in previous studies. However, a more complex picture emerges

when examining evolution of thermal gradients in subsequent days after the 5 June frontal passage when utilizing this day-to-day, synoptic framework.

After the 5 June cold frontal passage, the development of NLLJs was associated with daytime heating restoring boundary layer mixing and thermal gradients. The continued heating over the following days resulted in a progressively more intense and non-linear baroclinic zone and an associated surface low in eastern Colorado. Parish (2016) proposed that an IO acting on low-level v_g associated with this baroclinic zone may explain Bonner's climatology which found a frequency maximum of low-level jets in western Kansas and western Oklahoma. However, v_g was found to exhibit a nocturnal intensification of 5-10 m s^{-1} occurring over a 3 h period in a 2-3 km deep layer, making it difficult to determine ageostrophic enhancements from an IO. Variations of $v_g(z)$ were tied to changes in θ_v gradients aloft, in agreement with NLLJs documented during the PECAN field campaign (Gebauer et al. 2018; Smith et al. 2019).

Diurnal variations of v_g and associated changes in the zonal PGF in the ERA5 analysis exhibited day-to-day spatial variation and occurred at horizontal scales of $\sim$150 km. These changes were smoothed out when using the east-west extent of the ARM sites ($\sim$300 km). These heterogeneous spatial-temporal properties may explain the lack of geostrophic intensification found in composites from Parish (2016) and Parish and Clark (2017), as such features were likely smoothed out. Interestingly, the case study presented by Parish (2016) of a low-level jet that occurred on 3 June 2015 found a nocturnal enhancement to v_g of $\sim$10 m s^{-1} which occurred from $\sim$0200 to 0500 UTC in data collected from aircraft measurements, an associated increase is v was also evident. This evolution was described as a fundamental departure from their composites that indicated the southerly enhancement associated with the NLLJ over the SGP was primarily ageostrophic. Therefore the assumption of a constant $v_g(z)$ by previous studies may need to be evaluated.

The spatial gradients in the thermal gradients and the differences in the depth of the boundary in the late afternoon and early evening evolved during the recovery period until

the presence of a dryline was noted on 10 June. Our analysis was consistent with the known behavior of the dryline during the night with a retrogression upslope and changes in the thermal gradients on the slope. An important implication of the evolution toward the presence of a dryline is that the gradients on the slope become non-linear in violation of an assumption often made in studies of the NLLJ. Thus, the NLLJ is not only heterogeneous due to horizontal advection by the westerly flow along a sloping terrain, but due to strong differences in space and time in the thermal gradients along the slope.

As expected, the southerly NLLJ was found to play an important role in returning moisture to the region in the seconds recovery period. Moisture transport associated with this southerly NLLJ was found to occur over a deep layer and was not confined to the narrow layer of the v_{max}. This finding suggests that the diurnal variations in the zonal PGF noted earlier were important for contributing to moistening during the second recovery period. The return of moisture to the ARM sites created a more favorable environment for convection, with the distribution of moisture along the slope playing a key role in evolution of CAPE profiles at the ARM sites. Nocturnal enhancements to CAPE were observed at the ARM sites, with CAPE increasing by $\sim$1000-1500 J kg^{-1} in layers aloft. This evolution of CAPE exhibited a southwest to northeast trend overnight, consistent with findings by previous work that areas favorable for the tendency of convection to shift east, away from the High Plains overnight (Carbone et al. 2002). This trend was partly explained by intensification of westerly flow above the southerly NLLJ. This intensification of westerly flow impacted the distribution of CAPE along the slope by advecting moisture east and creating regions of convergence leading to ascent. Similar convergence and ascent have been documented in past studies (Trier et al. 2017; Gebauer et al. 2018; Smith et al. 2019) and has been identified as a source of CI contributing to the nocturnal maximum in precipitation over the region (Trier et al. 2017; Gebauer et al. 2018). This westerly enhancement was qualitatively similar to that produced by the Shapiro et al. (2016) analytical model. It was found that heterogeneous characteristics of the u_{max} were consistent with westerly

acceleration from variations in the zonal PGF that were linked southerly NLLJ. One other possible explanation for this evolution occurred when upslope flow intensified shortly after boundary layer mixing ceased, which may have produced a negative pressure perturbation. Consistent with dryline simulations by Sun and Wu (1992) which found easterly upslope flow developed when mixing down of westerly momentum ceased while frictional decoupling in the shallow PBL to the east produced an initial easterly acceleration. This finding provides a possible link between mid-level flow and evolution of surface conditions, with surface heating driving upslope flow to the east and deeper PBLs to the west. Future investigations are needed to confirm this association to evolution of low-level flow over the SGP. In addition, examination for similar diurnal variations in the PGF in the vicinity of heterogeneous PBLs may help determine how well these results can be generalized.

Bibliography

Anthes, R. A., Y.-H. Kuo, S. G. Benjamin, and Y.-F. Li, 1982: The evolution of the mesoscale environment of severe local storms: Preliminary modeling results. *Monthly Weather Review*, **110 (9)**, 1187–1213.

Arritt, R. W., T. D. Rink, M. Segal, D. P. Todey, C. a. Clark, M. J. Mitchell, and K. M. Labas, 1997: The Great Plains Low-Level Jet during the Warm Season of 1993. *Monthly Weather Review*, **125 (9)**, 2176–2192, doi:10.1175/1520-0493(1997)125⟨2176:TGPLLJ⟩2.0.CO;2.

Atkins, N. T., R. M. Wakimoto, and C. L. Ziegler, 1998: Observations of the finescale structure of a dryline during vortex 95. *Monthly weather review*, **126 (3)**, 525–550.

Banacos, P. C., and D. M. Schultz, 2005: The use of moisture flux convergence in forecasting convective initiation: Historical and operational perspectives. *Weather and Forecasting*, **20 (3)**, 351–366.

Barandiaran, D., S.-Y. Wang, and K. Hilburn, 2013: Observed trends in the great plains low-level jet and associated precipitation changes in relation to recent droughts. *Geophysical Research Letters*, **40 (23)**, 6247–6251.

Bechtold, P., N. Semane, P. Lopez, J.-P. Chaboureau, A. Beljaars, and N. Bormann, 2014: Representing equilibrium and nonequilibrium convection in large-scale models. *Journal of Atmospheric Sciences*, **71 (2)**, 734–753.

Benjamin, S. G., 1986: Some effects of surface heating and topography on the regional severe storm environment. part ii: Two-dimensional idealized experiments. *Monthly weather review*, **114 (2)**, 330–343.

Berg, L. K., L. D. Riihimaki, Y. Qian, H. Yan, and M. Huang, 2015: The low-level jet over the southern great plains determined from observations and reanalyses and its impact on moisture transport. *Journal of Climate*, **28 (17)**, 6682–6706.

Blackadar, A. K., 1957: Boundary Layer Wind Maxima and Their Significance for the Growth of Nocturnal Inversions. 283–290 pp.

Bluestein, H. B., 1992: Synoptic-dynamic meteorology in midlatitudes: Volume 1, principles of kinematics and dynamics.

Bluestein, H. B., and T. M. Crawford, 1997: Mesoscale dynamics of the near-dryline environment: Analysis of data from cops-91. *Monthly weather review*, **125 (9)**, 2161–2175.

Blumberg, W. G., K. T. Halbert, T. A. Supinie, P. T. Marsh, R. L. Thompson, and J. A. Hart, 2017: Sharppy: An open-source sounding analysis toolkit for the atmospheric sciences. *Bulletin of the American Meteorological Society*, **98 (8)**, 1625–1636.

Bonner, W. D., 1968: Climatology of the Low Level Jet. *Monthly Weather Review*, **96 (12)**, 833–850, doi:10.1175/1520-0493(1968)096⟨0833:COTLLJ⟩2.0.CO;2.

Bonner, W. D., and J. Paegle, 1970: Diurnal variations in boundary layer winds over the south-central united states in summer. *Monthly Weather Review*, **98 (10)**, 735–744.

Browning, K., and C. Pardoe, 1973: Structure of low-level jet streams ahead of mid-latitude cold fronts. *Quarterly Journal of the Royal Meteorological Society*, **99 (422)**, 619–638.

Buban, M. S., C. L. Ziegler, E. N. Rasmussen, and Y. P. Richardson, 2007: The dryline on 22 may 2002 during ihop: Ground-radar and in situ data analyses of the dryline and boundary layer evolution. *Monthly weather review*, **135 (7)**, 2473–2505.

Burrows, D. A., C. R. Ferguson, and L. F. Bosart, 2020: The role of upper-level coupling on great plains low-level jet structure and variability. *Journal of the Atmospheric Sciences*, **77 (12)**, 4317–4335.

Carbone, R. E., J. D. Tuttle, D. A. Ahijevych, and S. B. Trier, 2002: Inferences of Predictability Associated with Warm Season Precipitation Episodes. *Journal of the Atmospheric Sciences*, **59 (13)**, 2033–2056, doi:10.1175/1520-0469(2002)059⟨2033:IOPAWW⟩2.0.CO;2, URL http://journals.ametsoc.org/doi/abs/10.1175/1520-0469%282002%29059%3C2033%3AIOPAWW%3E2.0.CO%3B2.

Carlson, T., and F. Ludlam, 1968: Conditions for the occurrence of severe local storms. *Tellus*, **20 (2)**, 203–226.

Clark, A. J., W. A. Gallus Jr, and T.-C. Chen, 2007: Comparison of the diurnal precipitation cycle in convection-resolving and non-convection-resolving mesoscale models. *Monthly Weather Review*, **135 (10)**, 3456–3473.

Cook, B. I., R. L. Miller, and R. Seager, 2009: Amplification of the north american "dust bowl" drought through human-induced land degradation. *Proceedings of the National Academy of Sciences*, **106 (13)**, 4997–5001.

Cook, K. H., E. K. Vizy, Z. S. Launer, and C. M. Patricola, 2008: Springtime intensification of the great plains low-level jet and midwest precipitation in gcm simulations of the twenty-first century. *Journal of Climate*, **21 (23)**, 6321–6340.

Crawford, T. M., and H. B. Bluestein, 1997: Characteristics of dryline passage during cops-91. *Monthly weather review*, **125 (4)**, 463–477.

Curtis, R., and H. Panofsky, 1958: The relation between large-scale vertical motion and weather in summer. *Bulletin of the American Meteorological Society*, **39 (10)**, 521–531.

Danco, J. F., and E. R. Martin, 2018: Understanding the influence of enso on the great plains low-level jet in cmip5 models. *Climate Dynamics*, **51 (4)**, 1537–1558.

Demoz, B., and Coauthors, 2006: The dryline on 22 may 2002 during ihop_2002: Convective-scale measurements at the profiling site. *Monthly weather review*, **134 (1)**, 294–310.

Doswell III, C. A., H. E. Brooks, and R. A. Maddox, 1996: Flash flood forecasting: An ingredients-based methodology. *Weather and Forecasting*, **11 (4)**, 560–581.

Du, Y., and R. Rotunno, 2014: A simple analytical model of the nocturnal low-level jet over the great plains of the united states. *Journal of the Atmospheric Sciences*, **71 (10)**, 3674–3683.

Fedorovich, E., J. A. Gibbs, and A. Shapiro, 2017: Numerical study of nocturnal low-level jets over gently sloping terrain. *Journal of the Atmospheric Sciences*, **74 (9)**, 2813–2834.

Fritsch, J., R. Kane, and C. Chelius, 1986: The contribution of mesoscale convective weather systems to the warm-season precipitation in the united states. *Journal of climate and applied meteorology*, **25 (10)**, 1333–1345.

Gallus Jr, W. A., N. A. Snook, and E. V. Johnson, 2008: Spring and summer severe weather reports over the midwest as a function of convective mode: A preliminary study. *Weather and Forecasting*, **23 (1)**, 101–113.

Gebauer, J. G., and A. Shapiro, 2019: Clarifying the baroclinic contribution to the great plains low-level jet frequency maximum. *Monthly Weather Review*, **147 (9)**, 3481–3493.

Gebauer, J. G., A. Shapiro, E. Fedorovich, and P. Klein, 2018: Convection initiation caused by heterogeneous low-level jets over the great plains. *Monthly Weather Review*, **146 (8)**, 2615–2637.

Geerts, B., 2008: Dryline characteristics near lubbock, texas, based on radar and west texas mesonet data for may 2005 and may 2006. *Weather and forecasting*, **23 (3)**, 392–406.

Geerts, B., and Coauthors, 2017: The 2015 plains elevated convection at night field project. *Bulletin of the American Meteorological Society*, **98 (4)**, 767–786.

Gutowski Jr, W. J., Y. Chen, and Z. Ötles, 1997: Atmospheric water vapor transport in ncep–ncar reanalyses: Comparison with river discharge in the central united states. *Bulletin of the American Meteorological Society*, **78 (9)**, 1957–1970.

Haghi, K. R., and D. R. Durran, 2021: On the dynamics of atmospheric bores. *Journal of the Atmospheric Sciences*, **78 (1)**, 313–327.

Helfand, H. M., and S. D. Schubert, 1995: Climatology of the simulated great plains low-level jet and its contribution to the continental moisture budget of the united states. *Journal of Climate*, **8 (4)**, 784–806.

Hersbach, H., and Coauthors, 2020: The era5 global reanalysis. *Quarterly Journal of the Royal Meteorological Society*, **146 (730)**, 1999–2049.

Higgins, R., Y. Yao, E. Yarosh, J. E. Janowiak, and K. Mo, 1997: Influence of the great plains low-level jet on summertime precipitation and moisture transport over the central united states. *Journal of Climate*, **10 (3)**, 481–507.

Holton, J. R., 1967: The diurnal boundary layer wind oscillation above sloping terrain. *Tellus*, **19 (2)**, 199–205, doi:10.1111/j.2153-3490.1967.tb01473.x, URL http://tellusa.net/index.php/tellusa/article/view/9766.

Holton, J. R., 1973: An introduction to dynamic meteorology. *American Journal of Physics*, **41 (5)**, 752–754.

Hsie, E.-Y., R. A. Anthes, and D. Keyser, 1984: Numerical simulation of frontogenesis in a moist atmosphere. *Journal of the Atmospheric Sciences*, **41 (17)**, 2581–2594.

Hu, Q., J. A. Torres-Alavez, and M. S. Van Den Broeke, 2018: Land-cover change and the "dust bowl" drought in the us great plains. *Journal of Climate*, **31 (12)**, 4657–4667.

Igau, R. C., and J. W. Nielsen-Gammon, 1998: Low-level jet development during a numerically simulated return flow event. *Monthly weather review*, **126 (11)**, 2972–2990.

Jiang, X., N.-C. Lau, I. M. Held, and J. J. Ploshay, 2007: Mechanisms of the great plains low-level jet as simulated in an agcm. *Journal of the atmospheric sciences*, **64 (2)**, 532–547.

Kain, J. S., and Coauthors, 2013: A feasibility study for probabilistic convection initiation forecasts based on explicit numerical guidance. *Bulletin of the American Meteorological Society*, **94 (8)**, 1213–1225.

Kaplan, M. L., J. W. Zack, V. C. Wong, and G. D. Coats, 1984: The interactive role of subsynoptic scale jet streak and planetary boundary layer processes in organizing an isolated convective complex. *Monthly weather review*, **112 (11)**, 2212–2238.

Kincer, J. B., 1916: Daytime and nighttime precipitation and their economic significance. *Monthly Weather Review*, **44 (11)**, 628–633, doi:10.1175/1520-0493(1916)44⟨628:DANPAT⟩2.0.CO;2, URL http://journals.ametsoc.org/doi/abs/10.1175/1520-0493(1916)44%3C628:DANPAT%3E2.0.CO;2.

Lackmann, G. M., 2002: Cold-frontal potential vorticity maxima, the low-level jet, and moisture transport in extratropical cyclones. *Monthly Weather Review*, **130 (1)**, 59–74.

Lillo, S. P., and D. B. Parsons, 2017: Investigating the dynamics of error growth in ecmwf medium-range forecast busts. *Quarterly Journal of the Royal Meteorological Society*, **143 (704)**, 1211–1226.

Liu, C., and M. W. Moncrieff, 2000: Simulated density currents in idealized stratified environments. *Monthly Weather Review*, **128 (5)**, 1420–1437.

Loveless, D. M., T. J. Wagner, D. D. Turner, S. A. Ackerman, and W. F. Feltz, 2019: A composite perspective on bore passages during the pecan campaign. *Monthly Weather Review*, **147 (4)**, 1395–1413.

Maddox, R. A., 1983: Large-scale meteorological conditions associated with midlatitude, mesoscale convective complexes. *Monthly Weather Review*, **111 (7)**, 1475–1493.

Maddox, R. A., C. F. Chappell, and L. R. Hoxit, 1979: Synoptic and meso-α scale aspects of flash flood events. *Bulletin of the American Meteorological Society*, **60 (2)**, 115–123.

Mather, J. H., and J. W. Voyles, 2013: The arm climate research facility: A review of structure and capabilities. *Bulletin of the American Meteorological Society*, **94 (3)**, 377–392.

May, R. M., S. C. Arms, P. Marsh, E. Bruning, J. R. Leeman, K. Goebbert, J. E. Thielen, and Z. S. Bruick, 2008 - 2020: Metpy: A Python package for meteorological data. Boulder, Colorado, URL https://github.com/Unidata/MetPy, doi:10.5065/D6WW7G29.

Means, L. L., 1952: On thunderstorm forecasting in the central united states. *Mon. Wea. Rev*, **80 (10)**, 165–189.

Mitchell, M. J., R. W. Arritt, and K. Labas, 1995: A Climatology of the Warm Season Great Plains Low-Level Jet Using Wind Profiler Observations. URL http://journals.ametsoc.org/doi/abs/10.1175/1520-0434(1995)010%3C0576:ACOTWS%3E2.0.CO;2, 576–591 pp., doi:10.1175/1520-0434(1995)010⟨0576:ACOTWS⟩2.0.CO;2.

Mitchell, T., and D. M. Schultz, 2020: A synoptic climatology of spring dryline convection in the southern great plains. *Weather and Forecasting*, **35 (4)**, 1561–1582.

Nigam, S., and A. Ruiz-Barradas, 2006: Seasonal hydroclimate variability over north america in global and regional reanalyses and amip simulations: Varied representation. *Journal of Climate*, **19 (5)**, 815–837.

Ogura, Y., and Y.-L. Chen, 1977: A life history of an intense mesoscale convective storm in oklahoma. *Journal of Atmospheric Sciences*, **34 (9)**, 1458–1476.

Paegle, J., and G. E. Rasch, 1973: Three-dimensional characteristics of diurnally varying boundary-layer flows. *Monthly Weather Review*, **101 (10)**, 746–756.

Parish, T. R., 2016: A Comparative Study of the 3 June 2015 Great Plains Low-Level Jet. *Monthly Weather Review*, **144 (8)**, 2963–2979, doi:10.1175/MWR-D-16-0071.1, URL http://journals.ametsoc.org/doi/10.1175/MWR-D-16-0071.1.

Parish, T. R., 2017: On the forcing of the summertime great plains low-level jet. *Journal of the Atmospheric Sciences*, **74 (12)**, 3937–3953.

Parish, T. R., and R. D. Clark, 2017: On the initiation of the 20 June 2015 Great Plains low-level jet. *Journal of Applied Meteorology and Climatology*, **56 (7)**, 1883–1895, doi:10.1175/JAMC-D-16-0187.1.

Parish, T. R., R. D. Clark, and T. D. Sikora, 2020: Nocturnal destabilization associated with the summertime great plains low-level jet. *Monthly Weather Review*, **148 (11)**, 4641–4656.

Parish, T. R., and L. D. Oolman, 2010: On the role of sloping terrain in the forcing of the great plains low-level jet. *Journal of the atmospheric sciences*, **67 (8)**, 2690–2699.

Parish, T. R., A. R. Rodi, and R. D. Clark, 1988: A case study of the summertime great plains low level jet. *Monthly weather review*, **116 (1)**, 94–105.

Parsons, D. B., K. R. Haghi, K. T. Halbert, B. Elmer, and J. Wang, 2019a: The potential role of atmospheric bores and gravity waves in the initiation and maintenance of nocturnal convection over the southern great plains. *Journal of the Atmospheric Sciences*, **76 (1)**, 43–68.

Parsons, D. B., S. P. Lillo, C. P. Rattray, P. Bechtold, M. J. Rodwell, and C. M. Bruce, 2019b: The role of continental mesoscale convective systems in forecast busts within global weather prediction systems. *Atmosphere*, **10 (11)**, 681.

Parsons, D. B., M. A. Shapiro, R. M. Hardesty, R. J. Zamora, and J. M. Intrieri, 1991: The finescale structure of a west texas dryline. *Monthly weather review*, **119 (5)**, 1242–1258.

Parsons, D. B., M. A. Shapiro, and E. Miller, 2000: The Mesoscale Structure of a Nocturnal Dryline and of a Frontal–Dryline Merger. *Monthly Weather Review*, **128 (11)**, 3824–3838, doi:10.1175/1520-0493(2001)129⟨3824:TMSOAN⟩2.0.CO;2, URL http://journals.ametsoc.org/doi/abs/10.1175/1520-0493%282001%29129%3C3824%3ATMSOAN%3E2.0.CO%3B2.

Peckham, S. E., and L. J. Wicker, 2000: The influence of topography and lower-tropospheric winds on dryline morphology. *Monthly weather review*, **128 (7)**, 2165–2189.

Pinto, J. O., J. A. Grim, and M. Steiner, 2015: Assessment of the high-resolution rapid refresh model's ability to predict mesoscale convective systems using object-based evaluation. *Weather and Forecasting*, **30 (4)**, 892–913.

Pitchford, K. L., and J. London, 1962: The low-level jet as related to nocturnal thunderstorms over midwest united states. *Journal of Applied Meteorology*, **1 (1)**, 43–47.

Pu, B., and R. E. Dickinson, 2014: Diurnal Spatial Variability of Great Plains Summer Precipitation Related to the Dynamics of the Low-Level Jet. *Journal of the Atmospheric Sciences*, **71 (5)**, 1807–1817, doi:10.1175/JAS-D-13-0243.1, URL http://journals.ametsoc.org/doi/abs/10.1175/JAS-D-13-0243.1.

Rattray, C., D. B. Parsons, and A. Shapiro, 2018: Low-level jet making the atmosphere unstable again. *17th Annual Student Conf., Austin, TX, Amer. Meteor. Soc. S*, Vol. 168.

Reif, D. W., and H. B. Bluestein, 2017: A 20-year climatology of nocturnal convection initiation over the central and southern great plains during the warm season. *Monthly Weather Review*, **145 (5)**, 1615–1639.

Reif, D. W., and H. B. Bluestein, 2018: Initiation mechanisms of nocturnal convection without nearby surface boundaries over the central and southern great plains during the warm season. *Monthly Weather Review*, **146 (9)**, 3053–3078.

Roads, J. O., S.-C. Chen, A. K. Guetter, and K. P. Georgakakos, 1994: Large-scale aspects of the united states hydrologic cycle. *Bulletin of the American Meteorological Society*, **75 (9)**, 1589–1610.

Rodwell, M. J., D. S. Richardson, D. B. Parsons, and H. Wernli, 2018: Flow-dependent reliability: A path to more skillful ensemble forecasts. *Bulletin of the American Meteorological Society*, **99 (5)**, 1015–1026.

Rodwell, M. J., and Coauthors, 2013: Characteristics of occasional poor medium-range weather forecasts for europe. *Bulletin of the American Meteorological Society*, **94 (9)**, 1393–1405.

Ropelewski, C. F., and E. S. Yarosh, 1998: The observed mean annual cycle of moisture budgets over the central united states (1973–92). *Journal of climate*, **11 (9)**, 2180–2190.

Rotunno, R., J. B. Klemp, and M. L. Weisman, 1988: A theory for strong, long-lived squall lines. *Journal of the Atmospheric Sciences*, **45 (3)**, 463–485.

Schaefer, J. T., 1974a: The life cycle of the dryline. *Journal of Applied Meteorology and Climatology*, **13 (4)**, 444–449.

Schaefer, J. T., 1974b: The life cycle of the dryline. 444–449 pp., doi:10.1175/1520-0450(1974)013⟨0444:TLCOTD⟩2.0.CO;2.

Shapiro, A., E. Fedorovich, and J. G. Gebauer, 2018: Mesoscale ascent in nocturnal low-level jets. *Journal of the Atmospheric Sciences*, **75 (5)**, 1403–1427.

Shapiro, A., E. Fedorovich, and S. Rahimi, 2016: A Unified Theory for the Great Plains Nocturnal Low-Level Jet. *Journal of the Atmospheric Sciences*, **73 (8)**, 3037–3057, doi:10.1175/JAS-D-15-0307.1, URL http://journals.ametsoc.org/doi/10.1175/JAS-D-15-0307.1.

Smith, E. N., J. G. Gebauer, P. M. Klein, E. Fedorovich, and J. A. Gibbs, 2019: The great plains low-level jet during pecan: Observed and simulated characteristics. *Monthly Weather Review*, **147 (6)**, 1845–1869.

Song, J., K. Liao, R. L. Coulter, and B. M. Lesht, 2005: Climatology of the Low-Level Jet at the Southern Great Plains Atmospheric Boundary Layer Experiments Site. *Journal of Applied Meteorology*, **44 (1968)**, 1593–1606, doi:10.1175/JAM2294.1.

Squitieri, B. J., and W. A. Gallus Jr, 2016a: Wrf forecasts of great plains nocturnal low-level jet-driven mcss. part i: Correlation between low-level jet forecast accuracy and mcs precipitation forecast skill. *Weather and Forecasting*, **31 (4)**, 1301–1323.

Squitieri, B. J., and W. A. Gallus Jr, 2016b: Wrf forecasts of great plains nocturnal low-level jet-driven mcss. part ii: Differences between strongly and weakly forced low-level jet environments. *Weather and Forecasting*, **31 (5)**, 1491–1510.

Stokes, G. M., and S. E. Schwartz, 1994: The atmospheric radiation measurement (arm) program: Programmatic background and design of the cloud and radiation test bed. *Bulletin of the American Meteorological Society*, **75 (7)**, 1201–1222.

Sun, W., and Y. Ogura, 1979: Boundary-layer forcing as a possible trigger to a squall-line formation. *Journal of the Atmospheric Sciences*, **36 (2)**, 235–254.

Sun, W.-Y., and C.-C. Wu, 1992: Formation and diurnal variation of the dryline. *Journal of the atmospheric sciences*, **49 (17)**, 1606–1619.

Surcel, M., M. Berenguer, and I. Zawadzki, 2010: The diurnal cycle of precipitation from continental radar mosaics and numerical weather prediction models. part i: Methodology and seasonal comparison. *Monthly Weather Review*, **138 (8)**, 3084–3106.

Tollerud, E. I., and Coauthors, 2008: Mesoscale moisture transport by the low-level jet during the ihop field experiment. *Monthly weather review*, **136 (10)**, 3781–3795.

Trier, S. B., and D. B. Parsons, 1993: Evolution of environmental conditions preceding the development of a nocturnal mesoscale convective complex. *Monthly weather review*, **121 (4)**, 1078–1098.

Trier, S. B., J. W. Wilson, D. A. Ahijevych, and R. A. Sobash, 2017: Mesoscale vertical motions near nocturnal convection initiation in pecan. *Monthly Weather Review*, **145 (8)**, 2919–2941.

Tuttle, J. D., and C. A. Davis, 2006: Corridors of warm season precipitation in the central united states. *Monthly weather review*, **134 (9)**, 2297–2317.

Uccellini, L. W., 1980: On the role of upper tropospheric jet streaks and leeside cyclogenesis in the development of low-level jets in the great plains. *Monthly Weather Review*, **108 (10)**, 1689–1696.

Uccellini, L. W., and D. R. Johnson, 1979: The coupling of upper and lower tropospheric jet streaks and implications for the development of severe convective storms. URL http://journals.ametsoc.org/doi/abs/10.1175/1520-0493(1979)107%3C0682:TCOUAL%3E2.0.CO;2, 682–703 pp., doi:10.1175/1520-0493(1979)107⟨0682:TCOUAL⟩2.0.CO;2.

Walters, C. K., 2001: Airflow configurations of warm season southerly low-level wind maxima in the great plains. part ii: The synoptic and subsynoptic-scale environment. *Weather and forecasting*, **16 (5)**, 531–551.

Walters, C. K., and J. A. Winkler, 2001: Airflow configurations of warm season southerly low-level wind maxima in the great plains. part i: Spatial and temporal characteristics and relationship to convection. *Weather and forecasting*, **16 (5)**, 513–530.

Walters, C. K., J. A. Winkler, R. P. Shadbolt, J. van Ravensway, and G. D. Bierly, 2008: A long-term climatology of southerly and northerly low-level jets for the central United States. *Annals of the Association of American Geographers*, **98 (3)**, 521–552, doi:10.1080/00045600802046387.

Wang, S.-Y., and T.-C. Chen, 2009: The late-spring maximum of rainfall over the us central plains and the role of the low-level jet. *Journal of Climate*, **22 (17)**, 4696–4709.

Weckwerth, T. M., J. Hanesiak, J. W. Wilson, S. B. Trier, S. K. Degelia, W. A. Gallus Jr, R. D. Roberts, and X. Wang, 2019: Nocturnal convection initiation during pecan 2015. *Bulletin of the American Meteorological Society*, **100 (11)**, 2223–2239.

Weckwerth, T. M., and Coauthors, 2004: An overview of the international h2o project (ihop_2002) and some preliminary highlights. *Bulletin of the American Meteorological Society*, **85 (2)**, 253–278.

Whiteman, C. D., X. Bian, and S. Zhong, 1997: Low-Level Jet Climatology from Enhanced Rawinsonde Observations at a Site in the Southern Great Plains. *Journal of Applied Meteorology*, **36 (10)**, 1363–1376, doi:10.1175/1520-0450(1997)036⟨1363:LLJCFE⟩2.0.CO;2, URL http://journals.ametsoc.org/doi/abs/10.1175/1520-0450(1997)036%3C1363:LLJCFE%3E2.0.CO;2.

Wilson, J., S. Trier, D. Reif, R. Roberts, and T. Weckwerth, 2018: Nocturnal elevated convection initiation of the pecan 4 july hailstorm. *Monthly Weather Review*, **146 (1)**, 243–262.

Wilson, J. W., and R. D. Roberts, 2006: Summary of convective storm initiation and evolution during ihop: Observational and modeling perspective. *Monthly weather review*, **134 (1)**, 23–47.

Ziegler, C. L., and C. E. Hane, 1993: An observational study of the dryline. *Monthly weather review*, **121 (4)**, 1134–1151.